Design and evaluation of a powered prosthetic foot with monoarticular and biarticular actuation

Entwurf und Evaluation eines angetriebenen Prothesenfußes mit eingelenkiger und zweigelenkiger Aktuierung

Zur Erlangung des akademischen Grades Doktor-Ingenieur (Dr.-Ing.)
Genehmigte Dissertation von Julian Zeiß aus Gießen
Tag der Einreichung: 28.3.2023, Tag der Prüfung: 30.6.2023

1. Gutachten: Prof. Dr.-Ing. Ulrich Konigorski
2. Gutachten: Prof. Dr. André Seyfarth
3. Gutachten: Dr. rer. nat. Martin Grimmer
Darmstadt, Technische Universität Darmstadt, 2023

TECHNISCHE UNIVERSITÄT DARMSTADT

Electrical Engineering and Information Technology Department

Institute of Automatic Control and Mechatronics

Control Systems and Mechatronics Laboratory

Design and evaluation of a powered prosthetic foot with monoarticular and biarticular actuation
Entwurf und Evaluation eines angetriebenen Prothesenfußes mit eingelenkiger und zweigelenkiger Aktuierung

Accepted doctoral thesis by Julian Zeiß

1. Review: Prof. Dr.-Ing. Ulrich Konigorski
2. Review: Prof. Dr. André Seyfarth
3. Review: Dr. rer. nat. Martin Grimmer

Date of submission: 28.3.2023
Date of thesis defense: 30.6.2023

Darmstadt, Technische Universität Darmstadt, 2023

Bitte zitieren Sie dieses Dokument als:
URN: urn:nbn:de:tuda-tuprints-243305
URL: http://tuprints.ulb.tu-darmstadt.de/24330

Dieses Dokument wird bereitgestellt von tuprints,
E-Publishing-Service der TU Darmstadt
http://tuprints.ulb.tu-darmstadt.de
tuprints@ulb.tu-darmstadt.de

Vorwort

Die vorliegende Arbeit entstand während meiner Tätigkeit als wissenschaftlicher Mitarbeiter am Fachgebiet Regelungstechnik und Mechatronik der TU Darmstadt. An erster Stelle möchte ich Prof. Dr.-Ing. Ulrich Konigorski danken, der mir die Möglichkeit gab, am Fachgebiet Regelungstechnik und Mechatronik zu promovieren. Sein stetiger Rückhalt und das entgegengebrachte Vertrauen haben mich maßgeblich unterstützt. Mein größter Dank gilt Florian – ich hätte mir in den vergangenen Jahren keinen besseren Büronachbarn, Sparringspartner und Freund vorstellen können. Daneben danke ich meinem Mitstreiter Martin: Du hast mir dieses spannende Promotionsprojekt quasi ermöglicht und die Zusammenarbeit hat mir viel Freude bereitet.

Mein herzlicher Dank geht auch an die wissenschaftlichen Mitarbeiterinnen und Mitarbeiter des Fachgebiets Regelungstechnik und Mechatronik: Jonathan, Volker, Bernhard, Viktor, Alex, Marcel, Jonas, Patrick, Philipp Eric und allen anderen Wegbegleitern. Ihr habt meine Zeit am Fachgebiet bereichert und ich habe neben der Arbeit und Lehre vor allem die Pausen, den Kaffee und den Spaß mit euch allen sehr genossen! Bei Guoping vom Lauflabor möchte ich mich ebenfalls bedanken: Danke für dein Feedback zu meiner Dissertation und ich hätte mich gefreut, wenn wir häufiger hätten zusammenarbeiten können. Den administrativen und technischen Mitarbeitenden Corina, Ilse, Brigitte und Alfred danke ich für ihre herzliche Aufnahme, ihre Hilfsbereitschaft und die Fürsorge am Fachgebiet. Mein Dank gilt auch Alexander Stark und den Auszubildenden der Institutswerkstatt, die maßgeblich an der Gestaltung und Herstellung der Versuchsaufbauten beteiligt waren, die im Rahmen meiner Tätigkeit am Fachgebiet entstanden sind.

Ich möchte mich bei allen Studienteilnehmenden bedanken (Ihr wisst, wer gemeint ist), die an meiner Arbeit mitgewirkt haben. Jede Session, von der Schaftfertigung bis zum Gangexperiment, war inspirierend und bewundernswert. Ein besonderer Dank gilt Martin Brehm und dem Team vom Sanitätshaus Klein für ihr Interesse, ihre Anregungen und ihre herausragende handwerkliche Expertise.

Zu guter Letzt möchte ich meiner Familie – Karo, Lotte und Fritz – von ganzem Herzen danken. Ihr seid stets mein sicherer Rückhalt und mein Kompass und ermöglicht es mir, den aufregenden Dingen gelassen entgegenzusehen.

Darmstadt, Juli 2023

Julian Zeiß

Abstract

To overcome the limitations of passive prosthetic feet, powered prostheses have been developed, that can provide the range of motion and power of their human counterparts. These devices can equalize spatio-temporal gait parameters and improve the metabolic effort compared to passive prostheses, but asymmetries and compensatory motions between the healthy and impaired leg remain. Unlike their human counter part, existing powered prosthetic feet are fully monoarticular actuating only the prosthetic ankle joint, whereas in the biological counter part, ankle and knee joint are additionally coupled by the biarticular gastrocnemius muscle.

The goal of this work is to investigate the benefits of a powered biarticular transtibial prosthesis comprising mono- and biarticular actuators similar to the human example.

The contributions of the present work are as follows: A biarticular prosthesis prototype is methodically designed to match the capabilities of the monoarticular muscles at the human ankle joint as well as the biarticular gastrocnemius muscle during level walking. The prototype consists of an existing powered monoarticular prosthetic foot, which is extended with a knee orthoses and a stationary biarticular Bowden cable actuator. Both actuators are modeled as serial elastic actuators (SEA) and the identification of the model parameters is conducted. A model based torque control utilizing the measurements commonly available in SEAs, an impedance control law based on human ankle reference trajectories, and a high level control to enable steady walking in the lab are introduced. The proposed hardware setup and control structure can provide sagittal plane angles and torques similar to the mono- and biarticular muscles at the human ankle, with proper torque tracking performance and a freely adjustable allocation of torque between the monoarticular and biarticular actuator.

The biarticular prosthesis is evaluated in the gait lab with three subjects with unilateral transtibial amputation utilizing a continuous sweep experimental protocol to investigate the metabolic effort and spatio-temporal gait parameters. All subjects show a tendency to reduced metabolic effort for medium activity of the artificial gastrocnemius, although noise level and time variation are large. In addition to the reduction in metabolic effort, the artificial gastrocnemius is able to influence spatio temporal gait parameters between the impaired and the intact side, but partially opposing effects are observed among the individual subjects.

In conclusion, this thesis describes the implementation of an artificial gastrocnemius following the human example and the systematic investigation of metabolic effort and spatio-temporal gait parameters. It is shown that the addition of the artificial gastrocnemius to a monoarticular prosthesis can positively affect the investigated parameters. The meaningfulness of the results should be improved by increased clinical effort in future work.

Kurzfassung

Um die Einschränkungen passiver Prothesenfüße zu überwinden, wurden in den vergangenen Jahren angetriebene Prothesen entwickelt, die Bewegungsumfang und Leistung vergleichbar zum menschlichen Sprunggelenk ermöglichen. Diese aktiven Prothesen können spatiotemporale Gangparameter angleichen und die Anstrengung im Vergleich zu passiven Prothesen verbessern, wobei Asymmetrien und Kompensationsbewegungen zwischen gesundem und beeinträchtigtem Bein bestehen bleiben. Im Gegensatz zu ihrem menschlichen Vorbild sind existierende aktive Prothesenfüße vollständig monoartikulär, aktuieren also nur das Prothesensprunggelenk, wohingegen im menschlichen Bein Knöchel- und Kniegelenk zusätzlich durch den biartikulären Gastrocnemius-Muskel gekoppelt sind.

Das Ziel dieser Arbeit ist, die Vorteile eines angetriebenen Prothesenfußes mit mono- und biartikulären Antrieben gemäß vergleichbar zum menschlichen Vorbild zu untersuchen. Hierfür wird ein biartikulärer Prothesenprototyp methodisch entworfen, um das Verhalten sowohl der monoartikulären, als auch der biartikulären Muskeln am menschlichen Sprunggelenk bei ebenem Gehen nachzubilden. Der Prototyp besteht aus einem existierenden monoartikulären Prothesenprototyp, der mithilfe einer angepassten Knieorthese und einem externen, biartikulären Bowdenzugaktor erweitert wird. Beide Antriebe werden als seriell-elastische Antriebe (SEA) modelliert und die Identifikation der Modellparameter wird dargelegt. Es wird eine Reglerstruktur eingeführt, die kontinuierliches Gehen im Labor ermöglicht. Diese besteht aus einer modellbasierten Drehmomentregelung auf Basis der in SEAs gewöhnlich verfügbaren Messgrößen, einem Impedanzregelgesetz auf Basis menschlicher Referenztrajektorien, und einem übergeordneten Gangregler. Der vorgestellte Hardwareaufbau und die eingeführte Reglerstruktur können Winkel und Drehmomente in der Sagittalebene bereitstellen, die den mono- und biartikulären Muskeln am menschlichen Knöchel ähnlich sind, mit geeigneter Regelgüte und einer frei wählbaren Aufteilung des Drehmoments zwischen dem monoartikulären und dem biartikulären Aktor.

Die biartikuläre Prothese wird im Ganglabor mit drei Versuchspersonen mit einseitiger transtibialer Amputation mit einem rampenförmigen Protokoll evaluiert, um den Einfluss auf Anstrengung und spatiotemporale Gangparameter zu untersuchen. Alle Probanden zeigen eine Tendenz zu reduziertem metabolischem Aufwand bei mittlerer Aktivität des künstlichen Gastrocnemius, wobei Rauscheinflüsse und zeitliche Variation groß sind. Neben der Reduktion der Anstrengung ist der künstliche Gastrocnemius in der Lage, spatiotemporale Gangparameter zwischen beeinträchtigtem und unbeeinträchtigtem Bein zu beeinflussen, wobei teilweise gegensätzliche Effekte unter den einzelnen Versuchspersonen beobachtet werden.

Zusammenfassend beschreibt diese Arbeit die Implementierung eines künstlichen Gastrocnemius und die systematische Untersuchung von dessen Einfluss auf die Anstrengung und spatiotemporale Gangparameter. Es wird gezeigt, dass die Hinzunahme des künstlichen Gastrocnemius die untersuchten Parameter positiv beeinflussen kann. Die Aussagekraft der Ergebnisse sollte in zukünftigen Arbeiten durch erhöhten klinischen Aufwand verbessert werden.

Contents

Symbols and abbreviations

Latin symbols

a_*	Polynomial coefficient of nonlinear spring
$\boldsymbol{A}_*$	System matrix
$\boldsymbol{B}_*$	Input Matrix
c_M	Motor torque constant
c_n	Motor speed constant
$\boldsymbol{c}_*$	Output matrix
d	Viscous damping
D	Damping facotr (2nd order system)
f	Frequency
f	Stationary prefilter
F_*	Force
h_*	Lever arm
i_*	Gear ratio
I_*	Current
j	Imaginary unit of imaginary number
J_*	Mass moment of inertia
k_*	Spring stiffness
$\boldsymbol{k}_*$	State feedback controller gain
K_*	Controller gain
l_*	Length
m	Mass
M_*	Torque
n_*	Angular velocity in rpm
N	Filter length
P	Power
q	Gear parameter of SEA
r_*	Lever arm or radius
R	Electrical resistance
$R_{\mathrm{th},}$	Thermal resistance
s	Laplace variable
t	Time
$t_{\mathrm{g},*}$	Gait phase
T	Temperature
u_*	Control input (state space model)
U_*	Electrical voltage or control input (Laplace transform)
v	Walking velocity
x_*	Translational position

Greek symbols

α_*	Joint angle
α_{Cu}	Resistance coefficient of copper
β	Prosthesis rear angle
γ	Prosthesis spring angle
η	Efficiency
φ	Angle
κ	AG torque allocation factor
ω_{b}	Bandwidth
μ	Membership function
θ	Parameter vector
τ	Time constant

Abbreviations

AG	Artificial gastrocnemius
AW	Anti-windup
BS	Ball screw
CD	Controlled dorsiflexion
COP	Center of pressure
DOF	Degree of freedom
DS	Double support phase
ESR	Energy storage and return
FF	Feed-forward
GRF	Ground reaction force
HLC	High-level control
HS	Heel strike
IMU	Inertial measurement unit
LLC	Low-level control
LQR	Linear quadratic regulator
LS	Least Squares
MLC	Mid-level control
RMS	Root mean square
ROA	Ruggedized Odysseus Ankle
ROM	Range of motion
SEA	Series elastic actuator
SS	Single support
ST	Stance phase
SW	Swing phase
TD	Touch down
TF	Transfer function
TO	Toe-off
TTA	Transtibial amputation
WRA	Walk Run Ankle

1. Introduction

Human locomotion is a fascinating interaction between the human musculoskeletal and nervous systems. Neuromuscular functions and biomechanical components of the musculoskeletal system are likely the result of millions of years of evolutionary optimization and enable efficient, versatile and robust movements. This enables humans to seamlessly adjust their gait between standing, walking or running, efficiently adapt to terrain and environments, jump, climb or perform other complex movements. The loss of a lower limb diminishes these abilities and can have a significant impact on quality of life. Everyday tasks such as walking, running or climbing stairs become challenging. The amount of affected persons is considerable even in times of medical and health progress. In 2015, 55 595 lower extremity amputations were recorded in Germany, with about 30 % of the amputations being major amputations above the ankle joint [1]. In over 90 % of cases the causes for lower limb amputations are vascular diseases, trauma, and tumors [2]. In 2014, diabetes mellitus was diagnosed in about 64 % of all major amputations [3].

In the case of a transtibial amputation (TTA), i.e. an amputation between the ankle and the knee, medical care nowadays usually consists of a passive prosthesis. These attempt to approximate the function of the human ankle joint with the help of carbon springs. Since they are passive, positive work can be generated only by releasing potential energy previously stored in the elastic elements of the prosthesis on a stride by stride basis. The prosthetic foot shows a limited range of motion and reduced peak power when compared to the human counterpart [4]. As a result, they cannot provide the net positive work required in various everyday tasks. Compared to unimpaired individuals, people with unilateral TTA chose slower free walking velocities and show 20 % higher metabolic energy expenditure at the same controlled walking speed [5]. Furthermore, since they cannot actively move the foot, passive prosthetic feet require that the individual with TTA employs alternative strategies for example during stair ambulation or sit to stand movements. The compromised functionality of the impaired leg leads to asymmetrical gait patterns with increased loads on the remaining joints and especially increased loading of the intact limb [6]. This results in an increased risk of degenerative changes in the intact side, such as osteoarthritis of thee knee and hip joint [6], [7].

To overcome the limitations of passive feet, active prostheses such as the BiOM powered prosthetic foot [8] have been developed. These are capable of providing the range of motion and power of their human counterparts and can equalize gait parameters such as the preferred walking speed or metabolic cost [9]. Despite these improvements over passive prosthetic feet, asymmetries between the healthy and impaired leg remain even with powered prostheses. During the push-off, increased torques at the hip (referred to as hip-strategy) and reduced knee flexion torques are observed when compared to unimpaired individuals [10]. One possible reason for these observations is the point that, while mimicking human ankle behavior in the sense of joint angle and joint torque, powered prosthetic feet act solely monoarticular, i.e. they actuate the ankle joint exclusively. In contrast, next to the monoarticular soleus and tibialis anterior muscles, the human ankle joint also comprises the biarticular gastrocnemius muscle: it is attached to the heel of the foot via the Achilles tendon an the condyles of the femur, i.e. the thigh segment and therefore spans both, the knee and the ankle joint. Thus, the biarticular gastrocnemius can stretch the ankle and flex the knee simultaneously – a function that is missing in state of the art powered prosthetic feet. The authors in [10] state that the restoration of normal kinematics and kinetics in individuals with TTA is not possible with monoarticular powered transtibial prostheses and suggest that further studies regarding biarticular actuation should be

pursued.

The contribution of individual muscles to human locomotion is subject to research. Traditional inverse dynamics gait analysis allows to estimate the net joint torque, whereas the contribution of the various muscles in the over actuated human leg is unknown. Simulation based approaches employing optimal control techniques such as [11] are employed to determine the allocation of muscle forces, but the actual human goodness function is yet to be determined. Surface EMG measures give insight to the timing of individual muscles, but cannot be correlated with actual force amplitudes. Biarticular muscles allow the coupling and coordination of neighboring joints and are thought to improve the energy efficiency of human locomotion, and to transfer energy from proximal to distal joints and vice versa [12].

The study of biarticular assist systems in the literature is not new. Biarticular structures are widely represented in soft exoskeletons for the lower extremity and experimental studies show potential improvements in human effort [12]. Explicit replication of the biarticular gastrocnemius muscle in powered prostheses is the subject of only a few research studies. Endo et al. [13] and Willson et al. [14] use clutched springs to mimic the gastrocnemius function. Ziemnicki et al. [15] use a tethered prosthetic emulator to replicate the monoarticular and biarticular muscles at the ankle joint, but yet do not provide further results on the performance of the system and biomechanical effects observed with it. Eilenberg [16] emulated the function of the mono- and biarticular muscles at the ankle joint using a powered knee orthosis and the Biom foot. The system was evaluated with seven subjects, making it the most comprehensive study along with the work of Willson et al. [14]. The parameters defining the artificial gastrocnemius (AG) support in Eilenbergs study are fixed for each subject, and the authors suggest to systematically explore potential benefits of the AG device more broadly in the future. So far, there is no work in the literature that implements a powered artificial gastrocnemius with physical coupling similar to the human counterpart and systematically evaluates the potential effects on gait pattern and effort of individuals with TTA compared to monoarticular support only.

As such, the goal of the present work is to investigate whether prosthetic feet with biarticular actuation following the human example can positively affect gait parameters of individuals with TTA, as assessed by gait symmetry and effort, compared with monoarticular actuation only. To address this question, a novel prosthetic prototype is designed in this work with mono- and biarticular actuation of the prosthetic ankle and intact knee according to the human example. The novel biarticular prototype is tested with individuals with TTA on the treadmill.

Therefore, the contributions of the present work are as follows: Chapter 2 comprises the foundations of this work, covering the biomechanical basics of the lower limb, an overview of prosthetic feet and biarticular actuation in the literature, and an introduction into the control of powered prostheses. Chapter 3 targets the methodical design of the biarticular prosthesis prototype to match the capabilities of the mono- and biarticular muscles at the human ankle joint. Therefore, an existing powered monoarticular prosthetic foot is extended with a knee orthoses and a stationary Bowden cable actuator, which is capable to emulate the missing gastrocnemius and is therefore referred to as artificial gastrocnemius (AG), as it is done in [16]. In the subsequent three chapters, the control functionalities for using the novel prosthesis in the gait laboratory are designed. Chapter 4 describes the modeling of the actuators included in the prototype and the identification procedures required to determine the model parameters. Both actuators represent series elastic actuators, and the specifics of each setup are discussed. A cascaded approach is chosen for the control of the prosthesis with low level torque controllers and a high level control to enable walking on the treadmill in the gait lab. The torque controllers are the subject of Chapter 5, and the walking controller is designed in Chapter 6. In the final Chapter 7 the biarticular prosthesis is evaluated in the gait lab with three subjects with TTA.

2. Foundations

In this section, the foundations for the following chapters are presented. After an introduction to the biomechanics of level walking and the lower limb muscles involved in walking, a review of powered prosthetic feet and lower limb actuation systems from the literature is given. Special attention is given to Bowden cable actuation systems for treadmill applications in the lab. Subsequently, an overview of control approaches for lower limb prostheses is given. Since powered lower-limb orthoses and exoskeletons share many similarities with powered prostheses in terms of hardware design and control, those systems will also be taken into account in the overview.

2.1. Biomechanical foundations

Biomechanical analyses are usually carried out in a human body fixed reference frame. Here, three body planes are defined as shown in Figure 2.1a. The sagittal plane is the plane that divides the human in to right and left halves [17]. During level walking, the majority of work in the lower limb is done in the sagittal plane, in particular for the ankle joint with 93 % of the work [18]. Thus, in locomotion, e.g. symmetric walking or running, the analysis is often reduced to the sagittal plane, resulting in sufficient accuracy and reduced complexity. The lower extremity is then simplified to a model consisting of rigid links and revolute joints. A model consisting of the four segments foot, shank, thigh, and HAT (head, arms and torso) as illustrated in Figure 2.1b allows the analysis of the ankle, knee, and hip joint, which are the main joints involved in level walking.

2.1.1. Sign convention and nomenclature

All analyses in this work are restricted to the sagittal plane. Figure 2.1b shows the sign convention used in this work. Joint angles are defined as the inner joint angles between two links. Joint torques are defined such that positive torques tend to extend the leg. Joint power is defined positive, if involved muscles at the joint transfer power to the links, and negative if they absorb power from the links.

An increase in the joint angles is referred to as *extension*, and a decrease as *flexion*. For the ankle joint, moving the tip towards the ground is referred to as *plantar flexion*, and moving the tip towards the shank is referred to as *dorsiflexion*. Elements further away from the torso are referred to as *distal*, elements closer to the torso as *proximal*. [17]

In order to compare the data of different subjects, the joint torques and powers are usually normalized to body mass. For the joint angles, mean angles or angles at certain events such as touch down may be subtracted.

2.1.2. Sagittal plane leg musculature

The human leg is over-actuated, as is the entire human body, so that different muscles are capable of causing the same movement. It comprises monoarticular muscles spanning a single joint and biarticular muscles spanning two neighboring joints. Figure 2.2 shows the main muscle groups typically included in the analysis

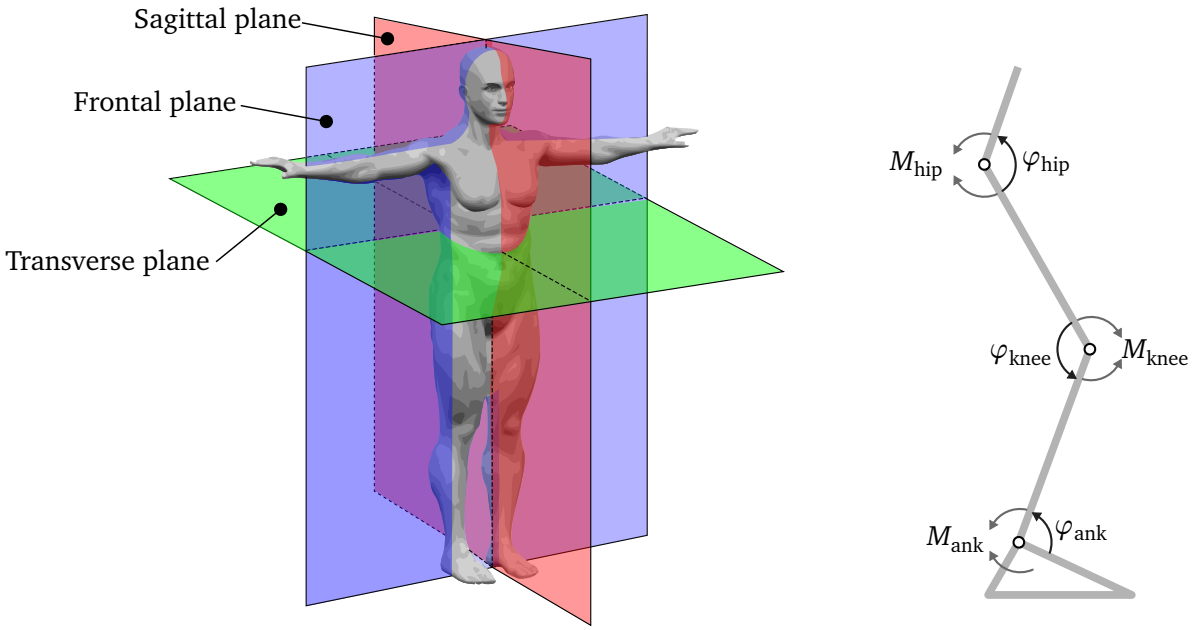

(a) Human body planes

(b) Planar model

Figure 2.1.: The main anatomical planes of the human body (a, original graphic [19]), and planar model with sign conventions for lower limb sagittal plane joint angles and torques (b)

of locomotion in the sagittal plane (e.g. [20], [21]). With rectus femoris, hamstrings and gastrocnemius, there are three biarticular muscles in the lower limb, contributing to the motion of hip, knee and ankle. Additionally, two major monoarticular muscles acting antagonistically are found at each joint. Of particular interest in this work are the monoarticular soleus and tibialis anterior muscles at the ankle joint as well as the biarticular gastrocnemius muscle, which act on the ankle and knee joint simultaneously.

Mono- and biarticular muscles do not exhibit physiological differences, but are thought to contribute to different locomotor subfunctions. The lever arm ratios of biarticular muscles are likely evolutionarily optimized for the coordination of adjacent joints and are believed to contribute to the efficiency and robustness of locomotion. The role of biarticular muscles in locomotion has long been the subject of research but is not yet fully understood. [22]
They allow the coupling and coordination of neighboring joints and are thought to improve the energy efficiency of human locomotion, transfer energy from proximal to distal joints and vice versa. [12]

The forces of individual muscles cannot be measured in vivo. With the help of methods such as inverse dynamics, only the superposed joint moments can be estimated without knowing the exact contribution of individual muscles. EMG signals do provide insight into the temporal activity of muscles, but cannot be directly equated with applied forces. While distal muscles show less cross-subject variability than proximal muscles, biarticular muscles show more cross-subject variability than monoarticular muscles [23]. In principle, the monoarticular soleus and the biarticular gastrocnemius show similar EMG signals with a peak at 50 % of the gait cycle, with the gastrocnemius showing slightly more variability in early stance and some activity in swing phase, in which the soleus shows no EMG activity [23].

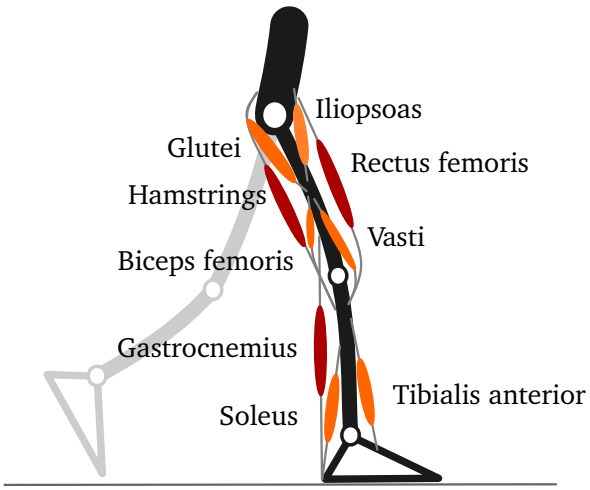

Figure 2.2.: Major mono- (orange) and biarticular (red) lower limb muscle groups included in musculoskeletal models for sagittal plane walking simulations.

Table 2.1.: Average lever arms for two cadaver measurements (averaging values for gastrocnemius medialis and lateralis for two cadavers from [24]), where the knee angle in maximum extension is defined as 180°

Joint	Posture	Lever arm
Knee	extended (170°)	28,5 mm
	flexed (110°)	16,25 mm
Ankle	neutral (90°)	52 mm
	plantar flexed (120°)	36,5 mm

Gastrocnemius lever arms at knee and ankle

The top end of the gastrocnemius originates from the lateral condyles of the femur, i.e. the knuckles above the knee joint. The lower end joins with the soleus into the Achilles tendon [17], connecting both muscles to the heel bone. Ankle and knee joint are, as human joints in general, not perfect rotary joints as found in machines. The pivot points and thus the lever arms of muscles change with the joint angles. Therefore, the lever arms of human muscles are investigated by observing length changes in prepared cadaver specimens (e.g. in [24]) and validated using simulation models of the human musculoskeletal system (e.g. [25], [26]).

In cadaver measurements in [24], the lever arm of the gastrocnemius at the knee joint decreases by an average of 43 % when the knee is flexed. The lever arm of the Achilles tendon at the ankle joint is maximal at a joint angle of 90°, i.e. when foot and shank are perpendicular. It reduces by about 30 % during maximum plantar flexion. For exemplary actual length values of the lever arms see Table 2.1.

Ankle and knee lever arm ratios of the gastrocnemius in simulation models in the literature range from $\frac{r_{\text{ank}}}{r_{\text{kne}}} = \frac{5.3}{2.5} = 2.12$ [25] to $\frac{r_{\text{ank}}}{r_{\text{kne}}} = \frac{3.45}{1.35} = 2.56$ [26].

2.1.3. Human locomotion

Being cyclic in nature, steady human walking is usually analyzed in a periodic manner. A gait cycle or stride is defined as the time interval between two consecutive repetitive events, typically from heel contact to

preceding heel contact of the same limb [17].

To compare strides with varying durations, stride time is typically normalized with the duration of the gait cycle. The normalized time is then given in % of stride or % gait cycle (% GC). The gait cycle can be divided into two distinct phases: the stance or stance phase is the phase when the foot has contact to the ground. It starts with heel strike, ends with toe-off, and lasts about 62 % of the gait cycle depending on the walking velocity [27]. The following phase without ground contact is referred to as swing or swing phase. Periods where both legs have ground contact are referred to as double support (DS, about 12 % GC [27]), and otherwise as single support (SS). Stance and swing may be divided into multiple subphases, depending on the joint being examined. From an ankle perspective, the stance is divided into early, mid and late stance, that are marked by the type of support, the type of foot contact, or other conditions. They are also be referred to as controlled plantar flexion, controlled dorsiflexion and powered plantarflexion [18]. A gait cycle of level walking with the presented events and phases is illustrated in top of Figure 2.3.

Running differs from walking in the way that there is no double support phase, but a flight phase in which neither leg is in contact with the ground. The focus of this work is on walking, and running is not considered any further within this work.

2.1.4. Level walking knee and ankle behavior

The torque and angle trajectories for a level walking stride at 1.05 m/s are shown in Figure 2.3. After the heel strike, the ankle performs a short phase of controlled plantarflexion until the tip of the foot reaches the ground at around 10 % GC. At higher walking speeds, or for some subjects even at lower speeds, dorsiflexor (i.e. negative) torques can be observed during the controlled plantarflexion. During the mid stance the ankle performs a slow dorsiflexion movement, during which the calf muscles (i.e. soleus and gastrocnemius) stretch and the ankle torque is steadily increased to reach a peak at about 50 % GC. This is followed by the pushoff, during which the ankle rapidly plantarflexes, the torque decreases and the leg is unloaded to swing into the swing phase. During the swing phase, foot clearance is provided by increasing the dorsiflexion and the torque is approximately zero.

The knee is mostly straight during the stance phase. It slightly flexes after the heel strike to absorb the impact. While load is transferred to the limb, the knee extensors provide an extension torque [20]. At about 30 % GC the knee torque turns to a flexion torque as a result of the increasing gastrocnemius forces contributing to the rising ankle torque [20]. The knee slightly extends before it flexes to initiate the swing phase. A short phase of extension torque is applied before the toe-off to limit the amount of knee flexion [20] in the following swing phase. A short period of flexion torque at the end of the swing decelerates the shank before the next heel strike.

The knee power (not shown) shows two distinctive negative buckles in early and late stance, whereas the ankle power has a distinctive positive peak during the unloading. The analysis of the mechanical work at both joints in [28] suggests that energy is transferred from the knee to the ankle joint during the early and mid stance and from the ankle to the knee joint during the unloading of the limb, both which can be provided by the gastrocnemius muscle. Further, in [10] subjects with unilateral amputation with a passive prosthesis or a powered monoarticular prosthesis showed reduced knee flexion torques during the mid stance when compared to their intact limb and a control group, which may be a result of the missing gastrocnemius function.

2.2. Lower limb actuation

This section gives an overview of the current state of the art foot prostheses and lower limb actuation systems. For the latter, actuators and human machine coupling, which are of relevance for the hardware

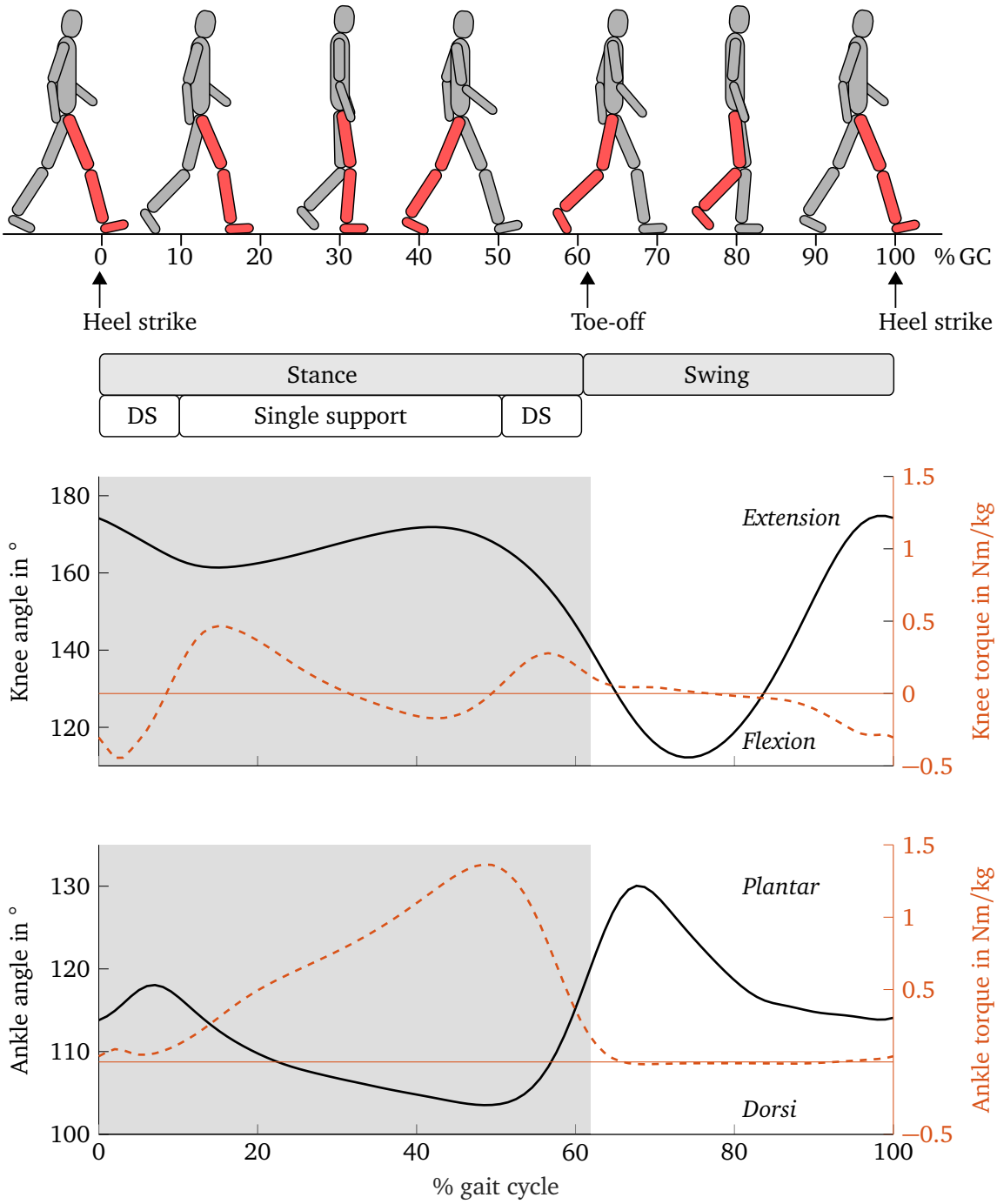

Figure 2.3.: Top: Level walking gait cycle with relevant phases (DS: double support) and events. Bottom: Knee and ankle angle and torque for level walking at $1.05\,\mathrm{m/s}$. Average trajectories of 21 subjects. Data from [28]

(a) passive (b) semi-active (c) active (d) active

Figure 2.4.: State of the art prosthetic feet: (a) passive Ottobock C-Walk [40], (b) semi-active Össur PROPRIO FOOT [41], (c) powered Ottobock Empower [42], and (d) powered Walk-Run-Ankle [35]

design in Chapter 3, is discussed. Lastly, an overview of experimental setups from the literature, that mimic the gastrocnemius in powered prostheses is provided.

2.2.1. Prosthetic feet

Most commercial prostheses are built from carbon fiber springs and damping elements and therefore are totally passive (e.g. Figure 2.4a). They are only able to return energy to the user that was previously stored in elastic elements the device. In level walking, energy is stored during the mid stance and released during pushoff. Hence they are referred to as energy storage and return (ESAR) prosthetic feet As a consequence, they cannot provide net-positive joint energy and mimic ROM and torques observed in human walking and activities of daily living. The result is an in increase in metabolic cost [5] compared to unimpaired people. In addition, the passive feet cannot actively move during the swing, as is for example necessary during stair descent, and thus cause unnatural gait adaptations.
Semi-active devices like Ottobock Trition or Össur PROPRIO FOOT (Figure 2.4b) contain actuators to change certain parameters of the prosthesis, such as resting angles. As a result, they are able to stretch the foot during sitting, adapt to ramps or increase the foot clearance during the swing phase. This is to increase comfort, flexibility or safety. Like passive prostheses, they do not provide net-positive joint work and therefore suffer same deficits.

To overcome the limits of passive and semi-active prosthetic feet, powered feet have been developed in the past 15 years. So far, Ottobock Empower (Figure 2.4c), a foot that has been developed from the BIOM [29] ankle, is the only commercially available system, but further feet such as the Walk Run Ankle [30] shown in Figure 2.4d can be found in the literature, for instance [31]–[34]. Common in these systems is, that they use an actuator to reproduce sagittal plane ankle kinematics for level walking and potentially other locomotion modes. In most cases, the actuator includes a serial spring, resulting in a series elastic actuator (SEA). In the Walk-Run-Ankle, a steel spring is used [35]. In the early BIOM prototype in [8], a serial leaf spring is paired with a unidirectional parallel spring, while in the Empower a series carbon spring and a carbon foot blade is used [36]. In all three feet, the series spring is paired with an electric motor, a ball screw and possibly other gear stages [8], [35], [36]. Similar to the passive feet, the series elastic element is used to store energy in the mid stance and release it during the pushoff. It can be optimized to reduce peak power and energy consumption of the motor [37], [38]. This way, for instance the Empower can match the intact limb in size and weight [39] and can provide power and torque similar to the human counterpart.

2.2.2. Lower limb actuation systems in the literature

Numerous experimental setups for lower limb actuation can be found in the literature, from which a selection is shown in Figure 2.5. The different solutions range from stationary tethered systems for treadmill use to mobile systems. While the design of mobile devices has to consider the lightweight implementation of actuators, power electronics and power supply, stationary prototypes often place those components off-board to reduce the weight carried by the user. A common method is to use Bowden cables to transfer forces from powerful off-board placed actuators to the joints of the user, for example Figures 2.5a, 2.5b and 2.5g. This enables the design of powerful testing platforms, whereby the component weight can be neglected. Typically, off-board actuators in laboratory setups are over-designed to cover a wider range of experiments [43]. Applications contain orthotic joints [44], [45], lower limb exoskeletons [46]–[48] or prosthetic device emulators [49].

Next to the power generation in the assistive device, the force transfer to the human body as well as the alignment of the assistive device with the human body segments and joints play a central role in the design. Since human joints are different in nature than machine joints, fitting the assistive device is generally accomplished through a combination of the following three elements: firm components such as links and mechanical joints, soft components such as cuffs and pads, and selectively added mechanical degrees of freedom.

2.2.3. Bowden cable actuators

In the literature, there are two solutions for Bowden cable actuators: Either the inner cable is wound on a pulley (e.g. [44], [49], [54], [55]), or it is translationally pulled through linear actuators (e.g.[56]). While pulley systems have to take into account the permissible bending radii of the rope or cable, translational systems are restricted by the limited travel distance. Actuators can be unidirectional [49], [56], i.e. allow slack rope in one direction, or bidirectional [44] using two opposed cables.

For the inner cables, synthetic rope [48] (e.g. Vectran or Dyneema) is widely used in tethered exoskeletons. The authors in [49] mention the flexibility resulting from the small bending radius (three times the rope diameter) and the durability as the major advantages compared to steel cables.

Besides, steel cables are typically used in Bowden cable systems, such as bicycle brakes. Steel cables consist of individual strands. Strands, in turn, consist of several wires laid in a spiral around a core. A 7x7 cable, for example, consists of seven strands of seven wires each [57]. Generally speaking, the more individual wires a rope contains, the more flexible it is, but the easier it is for individual wires to break. As an example, for a 7x7 cable, permissible bending radii have to be larger than 42 times the cable radius [57].

2.2.4. Physical human-robot coupling

Since humans are individually and oddly shaped, the connection between humans and machines poses a number of challenges. In [45] a good overview of the problem of coupling human and exoskeleton/orthosis is given for the design of an active knee orthosis. Here, a distinction is made between constrained kinematics and self-adjusting kinematics. The former define the course of the rotational axis as a function of the knee angle, resulting in a constrained guidance of shank and thigh. The synthesis of these kinematics is complex, the adaptation to users is individual and an exact alignment is practically impossible [45]. Self-adjusting kinematics release degrees of freedom and thus enable relative movement between human and exoskeleton. The following design guidelines result:

- Forces are to be applied perpendicular to the longitudinal axis of the body segment on which they engage.

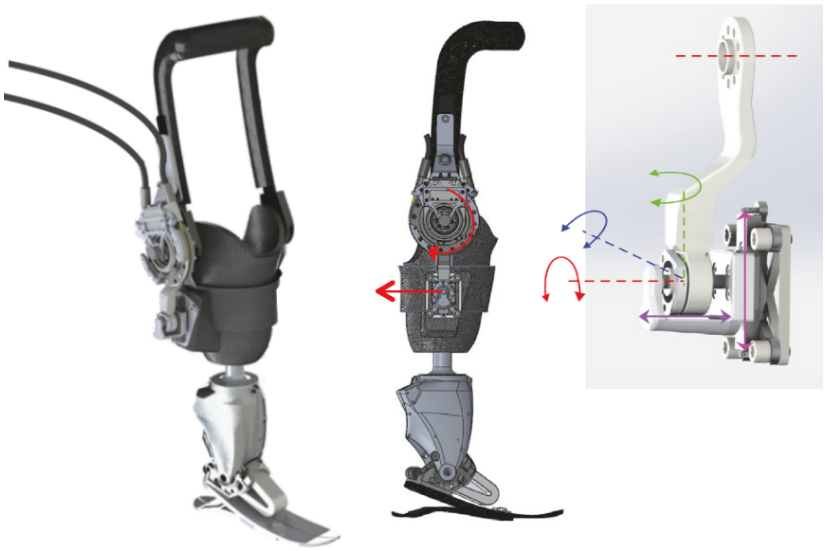

(a) Artificial gastrocnemius emulated with powered knee orthosis [44]

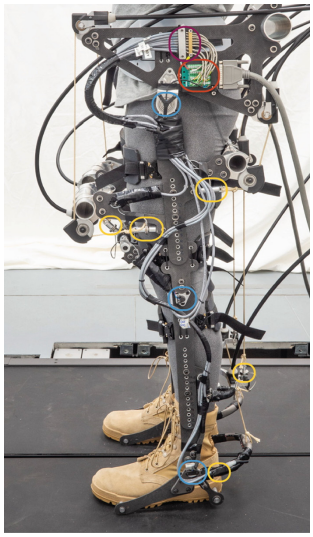

(b) Tethered lower limb exoskeleton [46]

(c) Clutched passive artificial gastrocnemius [50]

(d) Portable knee-ankle exoskeleton [51]

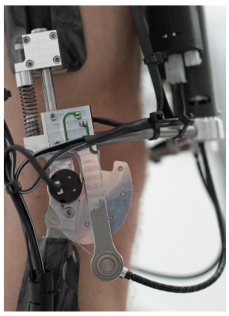

(e) Powered knee orthosis [45]

(f) Tethered biarticular prosthesis [15]

(g) Tethered ankle exoskeleton [47]

(h) Polycentric knee orthosis Genu Arexa [52]

(i) Mono- and polycentric knee joints [53]

Figure 2.5.: Selection of experimental setups for lower limb actuation including powered prostheses, orthoses and exoskeletons as well as commercial solutions for knee orthotics

- Cuffs should be as large as possible and torques on cuffs should be avoided.
- Coupling points between human and exoskeleton are to be realized with additional, passive degrees of freedom

Next to additional DOF, Witte et al. [43] suggest the use of selective compliance in the DOF that are not explicitly implemented in an exoskeleton. Further, forces to the body should be applied at large levers to reduce the pressure in the human tissue.

Commercial passive knee orthoses typically use soft sleeves, simple offset revolute joints to match the compromise pivot point of the knee, or polycentric knee joints (see Figure 2.5h and Figure 2.5i). Powered lower limb orthoses in the literature mostly use rigid planar mechanisms with 1-DOF revolute joints parallel to the limb, which are coupled to the human with large cuffs [51], [58] to enable relative motion. When single joints are actuated, usually simple rotatory joints are used in the device. For a gastrocnemius like implementation, Willson et al. [50] mount a knee orthosis with a thigh cuff and polycentric knee joint on a prosthetic shaft (Figure 2.5c). The kinematics are constrained, but mounting at a large distance from the knee joint allows relative motion between the human knee and the orthotic knee due to the elasticity inherent in the setup.

Instead of using soft cuffs, Eilenberg [44] and Müller [45] allow relative movement between user and device through additional mechanical degrees of freedom in the device. In [44], a knee orthosis mounted on a prosthetic socket (Figure 2.5a) is implemented by a revolute joint, whereby relative motion between the prosthetic socket and orthosis is enabled in five of six DOF. Hence, only force application perpendicular to tibia in sagittal plane is possible, decoupling rotational and longitudinal motion in the knee joint as proposed in [59]. In [45], the thigh cuff is guided in parallel using a spring-loaded linear guide (Figure 2.5e) with a stroke of 30 mm successfully reducing shear forces between the thigh and the orthosis.

2.2.5. Artificial gastrocnemius prototypes

Four relevant research papers exist in the literature on the replication of the biarticular gastrocnemius muscle in a prosthesis. Endo et al. [13] used a clutched spring that only spanned the knee joint in combination with a powered prosthetic foot. Tests with a single subject with TTA showed a metabolic cost decrease of 6.3 % compared to a passive prosthesis. The biarticular prototype is not tested against a powered prosthetic foot. Eilenberg et al. [16], [44] emulate the gastrocnemius muscle using a powered knee orthosis and powered BiOM prosthetic foot (see Figure 2.5a). The knee orthosis is actuated by an offboard placed Bowden cable actuator. The prosthesis is evaluated with six subjects with TTA. When compared to a monoarticular powered prosthesis, they observed a reduced hip positive work in late stance and metabolic benefits in some of the six subjects with TTA tested.

Both of the above mentioned designs emulate the function of the biarticular gastrocnemius muscle through the addition of a monoarticular actuator at the knee. In contrast Willson et al. [50] first presented a design physically connecting the thigh and the heel through a quasi-passive clutched spring with attachment points similar to the gastrocnemius muscle. The clutched actuator engages and disengages during the gait cycle to mimic the gastrocnemius muscle. It is combined with a passive prosthetic foot, hence lacks the function of a powered soleus and tibialis anterior muscle. The system was evaluated with seven subjects [14] and showed that the clutched actuator could provide forces with a similar timing as the gastrocnemius muscle. They showed that the biarticular actuator can modify the users gait, but did not significantly improve kinematic symmetry. Ziemnicki [15] presented a Bowden cable driven emulator that mimics soleus and gastrocnemius muscle (Figure 2.5f). The prototype extends the ankle prosthesis emulator presented in [49] with second actuator mimicking the gastrocnemius muscle. With four subjects with TTA they report that the hardware and heuristic controller can track a wide range of different actuation patterns for the artificial soleus and gastrocnemius, but did not carry out any clinical studies so far.

Next to the present work, [50] and [15] represent the only setups so far that implement a powered actuation physically linking knee and ankle joint comparable to the gastrocnemius muscle. Further, next to the present work [15] is the only prototype that implements a simultaneous physical powered actuation of the knee and ankle joint comparable to the human gastrocnemius muscle. Eilenberg [16] and Willson [14], [50] represent the only setups featuring an artificial gastrocnemius, that have been evaluated with subjects with TTA to a larger extent. So far there is no powered prosthesis physically implementing an active actuation, that simultaneously actuates the knee and the ankle joint comparable to the human soleus, gastrocnemius and tibialis anterior muscles.

2.3. Control strategies for powered lower limb prostheses and orthoses

The number of powered orthotic and prosthetic prototypes for the lower extremity has grown very rapidly since the early 2000s, and with it the number of different control strategies. An overview for the control of powered prostheses and orthoses is given in [60] and for powered knees in [61]. A more recent review of lower-limb exoskeleton control, which shares many aspects with the control of lower-limb prostheses, can be found in [62].

What follows is an overview of control approaches for powered prosthetic feet. With the application and hardware of this work in mind, the focus is on relevant concepts for powered prosthetic feet and laboratory applications on the treadmill. The goal here is to discuss relevant considerations, concepts, structures, and implementation aspects in order to understand and contextualize the controllers designed in Chapter 6.

Powered prostheses controllers usually employ hierarchical control structures consisting of a high-, mid-, and low-level controller [60], even though many research papers do not make this explicit distinction. In the high-level controller (HLC), the user's state and intent are estimated. The mid-level controller (MLC) translates the estimated intent into appropriate reference signals for the powered prosthesis. These typically are mechanical variables that are tracked at the lowest level by the low-level controller (LLC).

Before we look at specific solutions presented in the literature, some thoughts should be made on what behavior is desired for prostheses and therefore which variables actually need to be controlled in powered prostheses and orthoses. Being a mechanical joint, torque and angle are obvious candidates for the variables to be controlled in the device. In prosthetic joints, controlling the torque with no regard to the current position may lead to uncontrolled movements, stumbling or bumping into ROM limits [60]. In contrast, in case of powered orthoses and exoskeletons, torque is a suitable variable to be controlled (e.g. in [63] for a knee orthoses and [48] for an ankle exoskeleton), especially when the assisted human joints provide the majority of the total joint torque. On the other hand, stiff position control dictating the joint trajectories with no regard to the interaction forces and environment causes the user to react to the device rather than interact with it [64].

These considerations illustrate that the joint torque or joint position must be controlled taking into account each other. One approach to this is to control the joint impedance, i.e. the relation between the joint angle (or angular velocity) and the resulting torque [60]. The aim is to enable the user to perform movements similar to unimpaired locomotion, and to respond appropriately to user-specific patterns.

One more aspect when selecting the physical quantity to be controlled is the device-specific hardware. Position controlling a device is possible if the control law and the output impedance of the device lead to suitable interaction with the user, as demonstrated for instance in [65] for a knee ankle prosthesis or in [30] for an ankle prosthesis. Combined with the control law, the device output impedance and the user interaction, a position controlled system may show similar behavior to an impedance controlled system during certain locomotion.

2.3.1. High level control for treadmill applications

HLC locomotion intent estimation from different sensors based on mechanical sensors and electromyography (EMG) is the subject of much research [60]. One central point is the estimation of the gait mode, e.g. standing, level walking or stair climbing. Next to the direct volitional control by the user, solutions comprise heuristic rule based (HRB) classifiers based on finite state machines or decision trees, and machine learning based classifiers [60]. Heuristic rule based approaches are the solution found in commercial semi-active knee prostheses with the other approaches being restricted to powered research prototypes [61]. Regarding sensor inputs utilized in the HLC, the presented commercial semi-active and active prosthetic feet rely on kinematic sensors such as inertial measurement units (IMUs), which are also found in most laboratory prototypes. For the latter, however, there is a trend toward environment sensing with the aid of distance and depth-based sensors [66].

When testing hardware of new prototypes in the lab, gait mode is often assumed to be known. Initiation of gait is then often reduced to the distinction between standing and walking, and transitions between two gait modes are predictable from the experimental protocol. The HLC for such laboratory experiments can be achieved by simple HRB or by direct volitional control of experimental supervisors.

2.3.2. Mid level control

Given the locomotion intent from the HLC, the MLC generates suitable reference signals for the prosthetic device. Measured variables of the device, the user, and temporal information as well as joint trajectories from unimpaired subjects can be used for this purpose.

The joint behavior of unimpaired individuals usually serves as a template for the MLC. In particular MLC control laws may rely on continuous stride reference trajectories derived from unimpaired subjects. In such case, one important quantity found (in different forms) in many MLC laws is the continuous gait phase, which can be defined as the relative progression between the start and the end of a stride [67]. Start and end of the stride are defined by a reoccurring event such as the heel strike and the continuous gait phase takes values between 0 and 1, or 0 % and 100 %, respectively.

As will be seen in the following paragraphs, several strategies to tackle the problem exist: the gait phase is either estimated through extrapolation, or continuously derived from the user states, or continuous trajectories only play a role in the design, but not in the application of the MLC. Related examples are illustrated below.

Event and time based approaches

Event and time based MLC can probably be considered as the simplest approach to cyclic locomotion. Based on the regularity of the gait, time-based approaches repeatedly produce preprogrammed actions starting from a specific gait event such as the heel strike or the toe-off [60]. These preprogrammed actions can be reference trajectories adapted to the stride duration. The preprogrammed trajectories are adapted to the stride duration based on the duration of preceding strides. Averaging across multiple strides is common and the results can be improved by applying robust averaging methods as in [68]. In [35] the zero crossing of the shank angular velocity at the end of the stride is used to extrapolate the gait phase and to generate a reference signal for a powered prosthetic foot based on unimpaired ankle trajectories. The approach can be as good as the accuracy of the event detection as well as the regularity of the gait. As the reference generation is a simple feedforward control, limitations may also arise from gait asymmetries such as unusual duty cycles, leading to ill-timed support within the stride.

Switching finite state controllers

Going one step further, switching finite state controllers (FSC) divide the gait cycle into a sequence of finite states with clearly identifiable events for the transitions. For each state a reference, typically a reference impedance [69]–[72], is commanded to the prosthetic device. Typically, higher order springs as well as damping terms are employed as reference impedances. Energy is induces by varying the set points of the virtual springs in between the states. Shultz et al [70] separate the gait cycle into four states to control a powered prosthetic foot. Linear and fifth order springs as well as linear damping are used to approximate the ankle behavior. Sup et al. [71] use a sequence of five states, in each of which the reference torque is generated by a virtual linear spring and damper, to control a transfemoral prosthesis. Common to these approaches is the quickly increasing number of controller parameters. According to [60], FSC represent the most common MLC approach. In [8] the reference torque for a prosthetic foot is generated based on a neuromuscular model, which can be seen as a special case of FSC employing the neuromuscular model as virtual impedance of the ankle [73]. The model generates the reference plantarflexor torque based on the current joint angle, which is fed into a triggered nonlinear neuromuscular model.

Phase variable based approaches

In contrast to time based and FSC approaches, phase variable approaches are based on the idea that the temporal progress within a cycle can be bijectively assigned to an unactuated degree of freedom. Mostly, it is exploited that individual segment angles are piecewise monotonous while walking. In combination with a time derivative, the relative progression within the stride, the continuous gait phase can thus be determined. Holgate et al. [74] use the shank angle to control a powered prosthetic foot during level walking. Quintero et al. [65] control a knee-ankle-prosthesis based on the thigh angular velocity, which is a suitable phase variable even during non-steady, e.g. perturbed walking [75]. The phase variable may also be used to parametrize other gait parameters such as speed or inclination. In early applications, a single measurement, e.g. an angular velocity was used to manually derive the phase variable. In recent years, machine learning techniques were used to handle multiple measured variables to estimate the gait phase for different gait modes and transitions in between [67]. Compared to time based approaches, the phase variable approach has a potential to give adequate timed support with zero lag, and is therefore probably most suitable for the use outside the lab. Thatte et al. [76] use a phase variable and its time derivative, the gait phase velocity, to control a powered knee-ankle-prosthesis. Reference torques for the device are generated based on unimpaired human reference angle and angular velocity trajectories and a superposed feedforward toque. All trajectories in the control law are based on unimpaired human ankle and knee trajectories respectively.

To summarize, several approaches to replicate unimpaired human joint behavior with powered prosthetic devices during walking are found in the literature. Two clear trends exist: Either, progression within the stride is detected discretely based on specific events, or in a continuous manner based on extrapolation or a phase variable. Depending on this, references for the device are then defined by either varying set points of virtual impedances, or in a continuous form based on unaffected joint reference trajectories.

2.3.3. Low level control for SEAs

The actuator in prosthetic and orthotic applications most often comprises an electric motor, certain gear stages and a series elasticity, resulting in a series elastic actuator. In powered prostheses, the series elastic element is used to store energy and to reduce power and energy requirements of the motor. In powered orthoses and exoskeletons, the series elasticity is used to improve the perturbation rejection performance

[62], [77] and thus allow to improve back-driveability and impedance control. The serial elasticity can be either provided by an explicit machine element or is caused by soft elastic materials and the compliance of the interfering human tissue.

As discussed earlier, in most cases force respectively torque is the physical variable to be controlled in the prosthetic or orthotic application. Control approaches for force control of series elastic actuators can be divided into two groups. The first transfers the force control problem into a position control problem (e.g. [77], [78]) by controlling the spring deflection and estimating the resulting force from the spring stiffness. This approach is suitable if the hardware setup contains a dedicated spring with known spring stiffness. For this method it is necessary to measure both, the load and the motor position.

Kong et al. [78] proposed a PD-position control combined with a feed forward control and a disturbance observer to control the spring deflection of the SEA, where the disturbance observer was applied to the motor position and in later work to the load deflection [79]. As shown in [63], the approach can be transformed into an internal model control. Grün et al. [77] use a state space controller and a state and disturbance observer to control the force of the SEA in a powered knee orthoses. Feedback of the load side acceleration is used to compensate the motor inertia.

The second group feedbacks forces measured from force transducers, not explicitly relying on a specified elastic element and load position measurement. Subsets of PID control or cascaded controllers with inner velocity and outer force loop [80] are used. Pratt et al. [81] used a PID force controller and feedback of the load acceleration. Vallery et al. [80] investigated several cascaded controllers with respect to passivity. The recommended controller consists of two cascaded PI controllers, where the inner one controls the motor velocity and the outer one controls the output torque of the SEA. Whilst the passivity based approach by Vallery et al. guarantees stability in all conditions, guaranteeing passivity may restrict the performance of the torque control. Eilenberg [16] used an output PID torque controller combined with a P-type iterative learning control to compensate nonlinear friction and to track desired forces in a tethered knee orthosis.

Next to the above mentioned model based force control methods for SEAs, several partly heuristic approaches tailored to cyclic treadmill walking exist. Often the actual force-trajectory tracking problem is replaced by a simpler position control problem combined with an iterative control. As an example, Quinlivan et al. [54] adapt the force in an exoskeleton by iteratively manipulating a prototypical reference trajectory for the motor position on a stride by stride basis. Similar approaches are widely used in treadmill experiments in the literature. In general, they are tailored to a specific hardware and experiment and can yield suitable results, but may lack adaptability and robustness.

Last, a heuristic solution for providing high back-driveability in Bowden cable actuated exsosuits shall be mentioned. Instead of controlling forces close to zero, several groups (e.g. [47], [55], [82]) switch from force control to position control and actively provide slack cable, i.e. push out the cable, during zero force periods. Strategies to provide bumpless transfer when re-tensioning the cable often are not explicitly discussed.

3. Biarticular prosthesis prototype

This chapter describes the mechanical design of the biarticular prosthesis prototype. The basis for this is the monoarticular Ruggedized Odysseus Ankle (ROA, [83]) prosthesis from the company Spring Active, a powered prosthetic ankle comprising a series elastic actuator that can mimic human ankle torque and angle trajectories for level walking.

The goal is to design an experimental prototype that can be used to replicate the function of the biarticular gastrocnemius muscle for level walking on the treadmill. It should be able to meet the following requirements:

- The system should be able to generate up to 50 % of the human ankle torque using the artificial gastrocnemius for level walking with a walking speed of 1.55 m/s and a body weight of 80 kg (reference data from [28]).
  For said conditions, the maximum ankle torque to be provided is approximately 60 N m.
- It should be adaptable to different individuals with unilateral transtibial amputation for clinical studies.
- It should be usable by subjects without physical impairment for pre-testing purposes.
- The implementation of the biarticular actuator should follow the human model, respecting lever arm ratios and force application points.
- Forces of the artificial gastrocnemius have to be measured to estimate the applied knee and ankle torque.
- The hardware should be designed lightweight, as distal masses increase the metabolic costs and affect the biomechanics of walking [84].
- Since, with the ROA there is a potential monoarticular prototype available, the artificial gastrocnemius should be compatible with the existing ROA prosthesis.

Throughout this chapter, the hardware initially given in the project is presented. Experimental setups with similarities from the literature are presented and conceptual points of hardware design are discussed. Solutions to subproblems are discussed and the overall solution is presented. Lastly, a special focus is placed on the dimensioning of the drive unit of the biarticular actuator to emulate the ankle joint behavior.

3.1. ROA powered prosthetic foot and control unit

The powered prosthetic foot (Figure 3.1a) in use is a lab version of the Ruggedized Odysseuys Ankle (ROA, [83]) prosthesis (SpringActive, US), an updated version of the Walk Run Ankle (WRA) prosthetic foot. It comprises a 200 W brushless DC (BLDC) motor (maxon *EC*-4pole 30), a 2.44 : 1 belt drive, a 1 mm pitch ball screw and a lever mechanism to actuate a serial steel spring. The components of the resulting series elastic actuator (SEA) are designed to reproduce the biomechanics of the human ankle joint. In particular, the

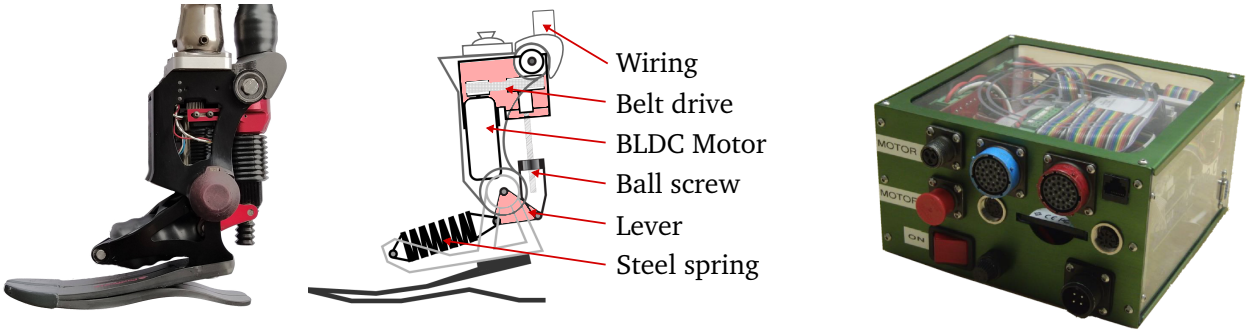

(a) ROA prosthetic foot (b) Control unit

Figure 3.1.: Hardware existing in the project: powered prosthetic foot ROA (Ruggedized Odysseus Ankle), schematic representation of the ROA, and control unit comprising target computer and power electronics.

series elasticity is optimized to reduce the motor peak power and energy consumption during level walking. Encoders measure motor position and ankle joint angle, by which the deflection of the serial spring and the resulting ankle torque can be estimated. A 6-axis inertial measurement unit (IMU) is placed in the shank of the prosthesis. Motor and sensors are connected to an offboard placed control unit by cable. A Pacifica LP carbon foot (stiffness category 9) a foot cosmetic and a sports shoe are used. The stiffness of the carbon foot is chosen as high as possible for two reasons: firstly, because it is connected in series to the optimized steel spring of the SEA and therefore alters the impedance of the drive train. Secondly, the deformation of the carbon spring is not measured and should therefore be as small as possible. The maximum user weight of the carbon foot is 166 kg, and it is therefore assumed to be rigid compared to the series elasticity of the ROA. The total weight of the ROA including the carbon spring and the cosmetic is 2.6 kg.

The control unit (Figure 3.1b) comprises a real-time target computer (PCM-3353, Advantech), analog and digital IO boards (model 526, Sensoray) and two motion controllers (AZBE40A8, Advanced Motion Controls). The motion controllers feature analog current control loops and can drive brushed or brushless DC motors with 40 A peak and 20 A continuous current. Power is supplied either by a lithium ion battery with eight cells or by a fixed voltage laboratory power supply. The control unit and the battery can be carried in a backpack for field testing or placed next to the user when used stationary, e.g. on a treadmill. Controllers are designed in Simulink using the MATLAB real time software environment xPC Target and are executed with a sampling frequency of 1 kHz.

3.2. Hardware design

Based on the observations and experience from the literature (see Section 2.2.2), the following principal design is chosen for the biarticular prosthesis prototype: The artificial gastrocnemius (AG) is designed as a Bowden cable actuator to keep the weight carried by the user as low as possible. A knee orthosis is used to transfer the AG forces to the human thigh. Force application points for the AG and the lever arms at knee and ankle are selected similar to the human example.

The resulting prototype can be seen in Figure 3.2. The development of the components is described in the following sections and background information on certain design aspects and decisions are discussed.

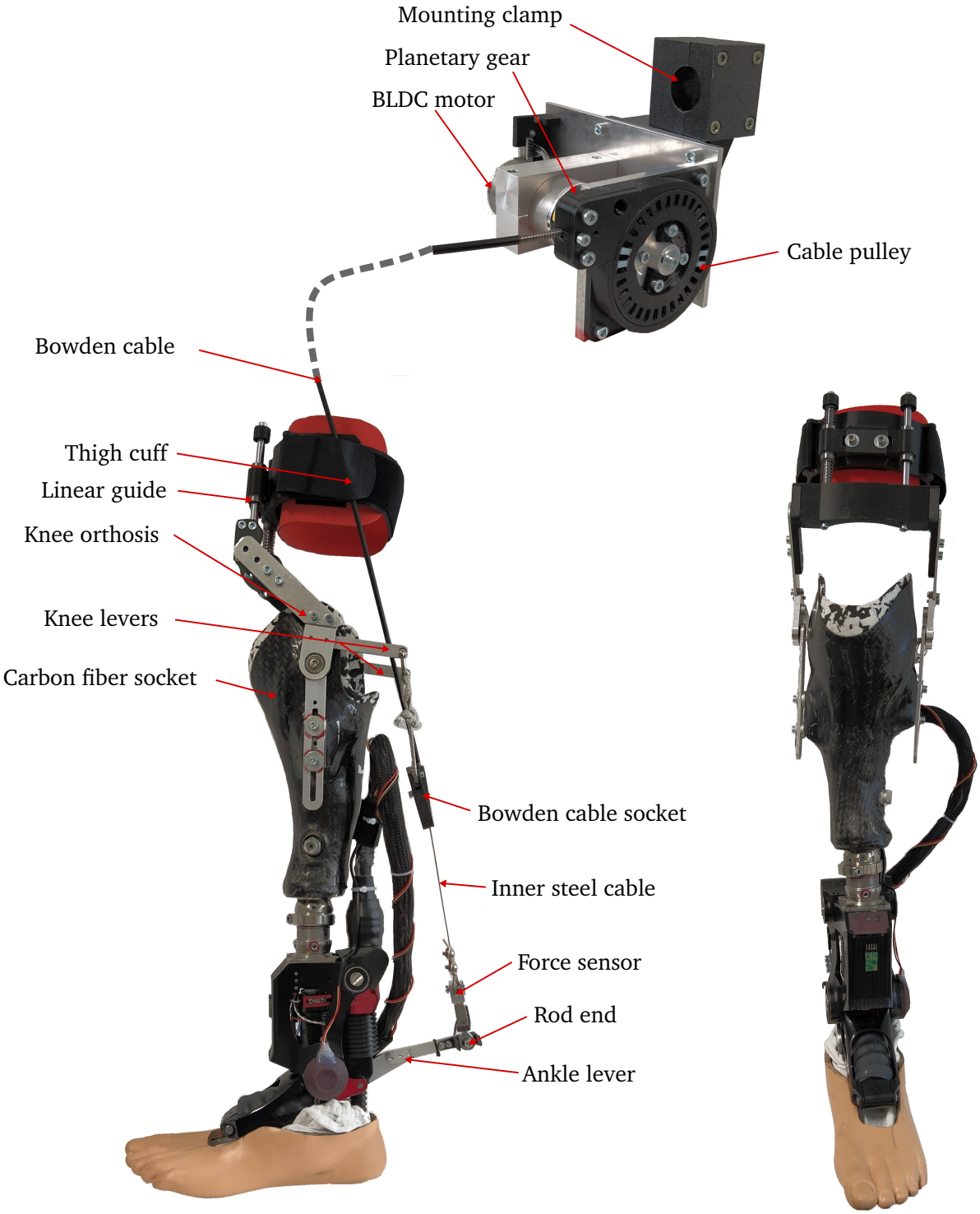

Figure 3.2.: Biarticular prosthesis prototype consisting of worn prosthesis and offboard placed Bowden cable actuator. The major components are labeled.

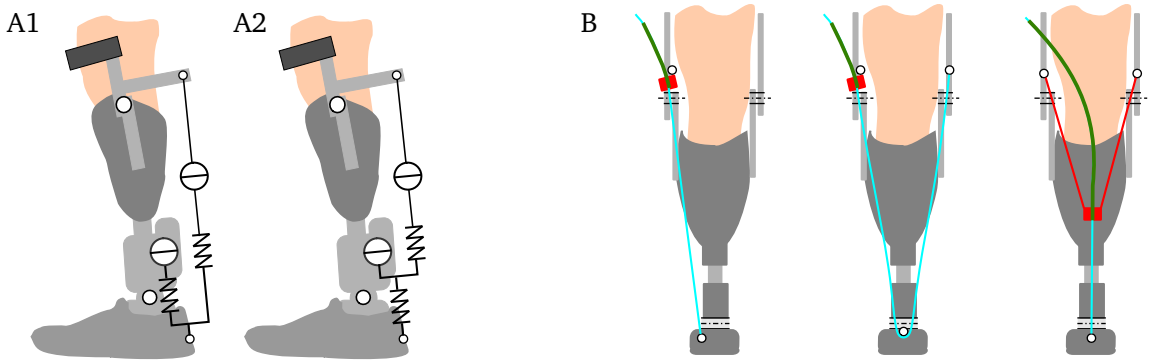

Figure 3.3.: A) Possible mechanical topologies comprising the mono- and the biarticular Actuator. B) Bowden cable routing options from left to right: I-, V-, and Y-shaped

3.2.1. Mechanical topology

The force of the AG is applied above the knee joint and below the prosthetic ankle joint, e.g. at the foot part of the prosthesis. Due to the compliance of the interacting human tissue, the AG can be assumed to be an SEA. At the lower end, the force application is possible at two points, either between the motor and the spring of the monoarticular SEA (Figure 3.3, A2), or at the foot part (see Figure 3.3, A1).

Choosing the latter of these options holds several advantages: First, the installation space is more open. Moving parts of the monoarticular SEA stay untouched and the ROA can still be used unmodified in other experiments. Secondly, both actuators share the same topology, so they can be considered in a similar way but independently from each other during the modeling, identification and controller design. The disadvantage is that in this case the monoarticular actuator no longer emulates the behavior of the ankle joint alone, for which the series elasticity was optimized.

Hence, in a final design one would either chose option A2 or re-optimize both elasticities in A1. In the case of the intended prototypical implementation, the advantages of A1, in particular the simple usability of the ROA without AG, outweigh those of A2. Therefore, option A1 is chosen for the prototype.

3.2.2. Bowden cable routing

When installing the Bowden cable, it is necessary to take into account that the device is worn both by subjects without an amputation with the help of an orthotic bypass and by subjects with an amputation with the help of an adapted prosthetic socket. Figure 3.3 shows the considered attachment options, which are discussed in the following.

The I-shaped variant results in easy cable routing and low lateral forces in the knee orthosis due to the long vertical dimensions. The single-sided asymmetric force application increases torsional forces in the knee orthosis and thigh bracket and therefore implies a more solid design, potentially increasing the system weight.

The V-shaped variant mitigates this asymmetry using a pulley at the lower end on the cost of complexity. The intrinsic $2:1$ gear ratio is advantageous, as it reduces the load on the drive gear and the need for small winding pulleys (see restrictions for Bowden cables in Section 2.2.3). With this variant, challenges arise due to the rope guidance (especially at low rope forces) and the permissible bending radii of the rope.

The Y-shaped option involves an upper pulley holding the Bowden cable housing. This pulley can be adapted to individual leg length and the asymmetric configuration with the orthotic bypass. Rope material

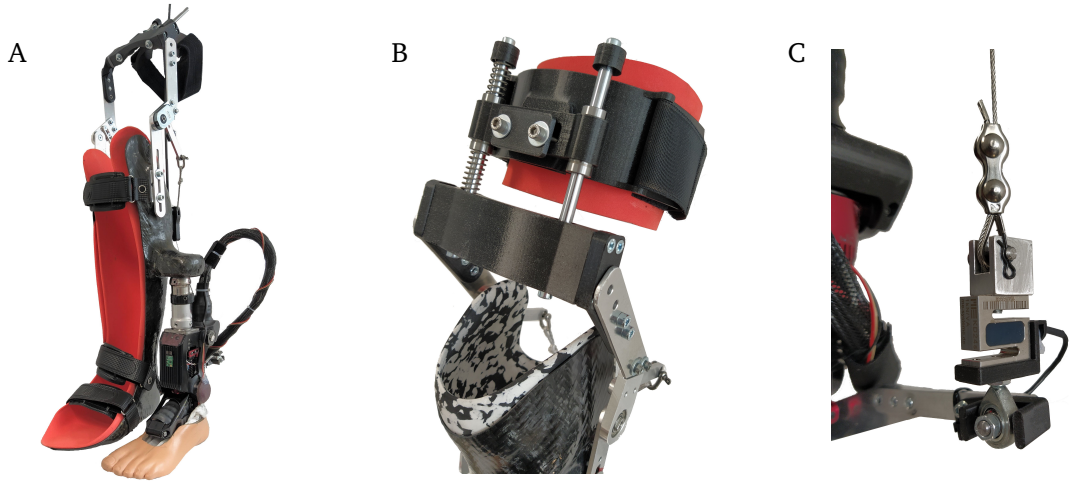

Figure 3.4.: From left to right: Bypass for prototyping with unimpaired subjects (A), Detail view on knee orthosis and guided thigh cuff (B), and rod end mounted force sensor at the ankle end effector (C).

for this pulley can be selected independently from the Bowden cable. Lateral stress in the thigh bracket is expected to be larger than in the other variants, whilst the force application is symmetric. The cable socket (red part) is expected to be less complicated than the pulley in the V-shaped variant. Compared to the I-shaped variant, the stress in the orthotic knee joint and thigh bracket is expected to be lower. Therefore, the Y-shaped option is chosen to be implemented in the prototype.

3.2.3. Prosthetic socket and orthotic bypass

The orthotic bypass (see Figure 3.4 A) and prosthetic sockets (as displayed in Figure 3.2) are built with the assistance of a local orthotist. The bypass is built as a carbon reinforced frame structure and fitted to a research assistant involved in the project. During plaster casting, the foot is slightly dorsiflexed. This is to avoid collisions of the bypass with the ground when walking and to keep the build-up height low. The prosthetic foot is placed next to the bypass so that the prosthetic ankle joint lies vertically below the human ankle joint. The lateral displacement is approximately 130 mm . The distance is chosen as small as possible to minimize frontal plane torques in the shaft but preventing crashes between prosthetic foot and bypass. Two adapter plates are laminated into the upper part of the bypass to accommodate the knee orthosis. The weight of the bypass is 1.98 kg. When wearing the bypass, the ipsolateral foot is raised accordingly by an additional sole by 55 mm to match the leg length. The total weight of the bypass setup including the ROA prosthetic foot and the knee orthotic parts designed in the following sections is 5.5 kg. This weight is in addition to the own limb constrained in the bypass.

For each subject with TTA, an individual prosthetic socket containing the mechanical interfaces for the AG is fabricated (shown in Figure 3.2). The prosthetic foot is aligned to the subject by the orthotist. The weight of the individual sockets is between 780 g and 1040 g, resulting in a total weight of the prototype between 4.26 kg and 4.52 kg.

For both the orthotic bypass and the prosthetic socket, the adapter plates are placed to enable an alignment of the knee axis following the compromise axis method by Nietert [85].

3.2.4. Knee orthosis and thigh cuff

Based on the human-robot interaction design guidelines discussed in 2.2.2, the knee orthosis is designed as a rotational joint with a linear guided thigh cuff (see Figure 3.4 B) similar to [45].

Care is taken to ensure that the knee orthosis can be adapted to the bypass and the individual prosthetic sockets. A modular design and the use of additive manufacturing technology (FDM 3D-printing) for subject individual parts such as the thigh bracket allows adaptation to the length, thickness and shape of the leg. The height of the knee axis is adjusted using slotted holes, allowing alignment by the orthotist. The thigh cuff can be laterally offset and tilted in the frontal plane by ±10°. Spacers allow the adjustment to the width of the thigh. Flexible bands are used to fix the cuff to the thigh.

Preliminary tests with the bypass revealed a relative motion of up to 30 mm between the human thigh and a rigid thigh cuff for 90° knee motion. To prevent relative motion between the cuff and the human tissue and to reduce sheer forces, the thigh cuff is mounted on a spring-loaded linear guide with two pretensioned compression springs with a travel of 40 mm. The resulting spring stiffness is 0.513 N/mm, leading to expected shear forces smaller than ±8 N, which was not found to be disturbing in preliminary tests. Double linear bearings are used on each rail to absorb tilting moments and to prevent jamming. An elastic strap is used to fix the cuff to the thigh.

3.2.5. Lever arms

As seen in the literature, the gastrocnemius lever arm ratio at ankle and knee is between 2 : 1 and 2.5 : 1. To enhance possible effects due to the AG, a more knee-heavy ratio of 2 : 1 is chosen to be implemented. Given the installation space, the ankle and knee levers were specified at 160 mm and 80 mm, respectively. The knee lever is vertically offset to the knee axis by 23 mm.

At the ankle, the force sensor (KD24s 1kN, ME-Meßsysteme) is mounted on a rod pin in order to align it with the Bowden cable. Because the level walking ankle ROM of ±15° is small, the lever arm at the ankle does not change significantly during level walking.

In contrast, the knee ROM is almost twice as large, so the knee lever significantly changes with the knee angle. An almost constant lever arm during the stance phase is desired, as this is the part of the gait cycle during which the AG can apply force. Figure 3.5 left shows the assembly of the knee lever and Figure 3.5 right shows the resulting lever arm for level walking at 1.05 m/s (based on average joint angles from [28]). In addition, the corresponding ankle torque is displayed, which can be supplied in part by the gastrocnemius. As can be seen, the lever arm is approximately constant during the stance phase, in which high ankle torques are expected, and only significantly decreases during swing phase, in which the ankle torque is close to zero.

3.2.6. Bowden cable actuator

The Bowden cable actuator (see Figure 3.6) comprises a BLDC motor, a planetary gearbox and an aluminum disk to wind the cable. A 3D-printed housing with small clearance prevents the cable from slipping of the disk. Since slack rope can occur during rapid movements with low forces, a clearance is provided around the circumference of the disk (see Figure 3.6 right). This prevents the need to push the slack cable through the outer conduit and possibly kinking it. A similar feature is found in the translational Bowden cable actuator in [56], but none of the rotatory actuators investigated in the literature.

In [86] pre-tests with an early Bowden cable actuator prototype with several different rope materials and rope forces between 20 and 120 N were conducted. As a result, lubricated stainless steel cables showed less friction than polyester ropes and nylon-coated steel cables. For the combination of a two staged planetary gear and a 1.5 m of Bowden cable, an efficiency of $\eta = 60\,\%$ with straight and $\eta = 48\,\%$ with bent Bowden cable (90°) is determined. Given that the efficiency of the planetary gear alone is up to $\eta_{\text{Gear}} = 83\,\%$

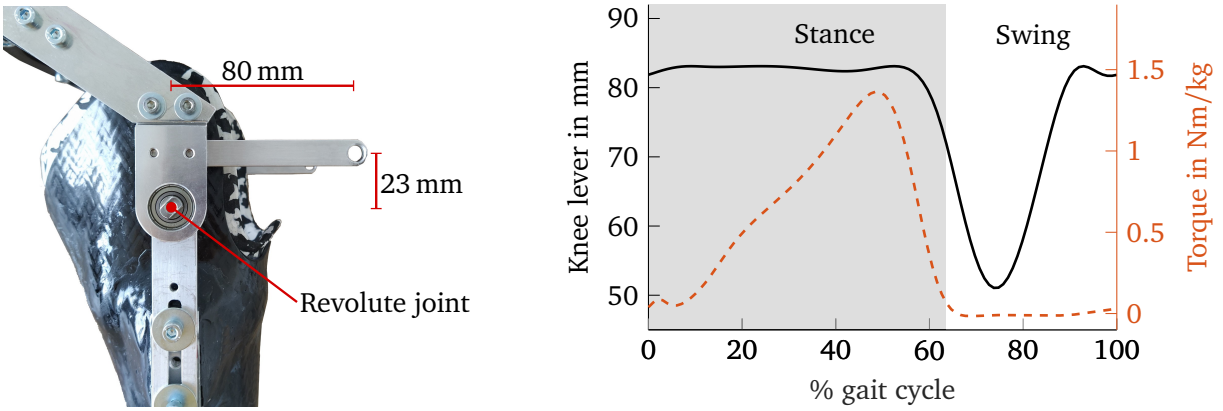

(a) Knee joint and lever

(b) AG lever arm during gait cycle

Figure 3.5.: Knee lever assembly and expected AG lever arm for a stride of level walking at 1.05 m/s

according to manufacturers data sheet, the efficiency of the lubricated steel Bowden cable in the given setup can be expected to be in a in a region of

$$\eta_{\text{Bow}} = \frac{\eta}{\eta_{\text{Gear}}} \approx 55\,\% \text{ to } 72\,\% \,,$$

depending on the cable forces and shape. It was further observed, that the efficiency improves with rising cable forces.

Given the ankle lever of 160 mm and the maximum ankle torque of 60 N m to be provided, the resulting peak cable forces are in a region of 375 N ($\eta_{\text{Bow}} = 1$) to 680 N ($\eta_{\text{Bow}} = 0.55$). Thus, a 1.5 mm stainless steel cable (1.4401, construction 7x7) is chosen and the actuator disc radius is specified at

$$r_{\text{disc}} = 30\,\text{mm} \,.$$

According to the manufacturer, the breaking force of the cable is 1265 N and the recommended minimum bending radius is 31.5 mm. The stainless steel rope is combined with an outer tube consisting of a steel helix with POM-liner (Polyoxymethylene). While the breaking force is two times higher than the maximum expected cable forces, the actual bending radius is slightly lower than recommended. Nevertheless, no significant wear of the cable was observed during 4.5 h of walking experiments, which was the longest period conducted with a single cable.

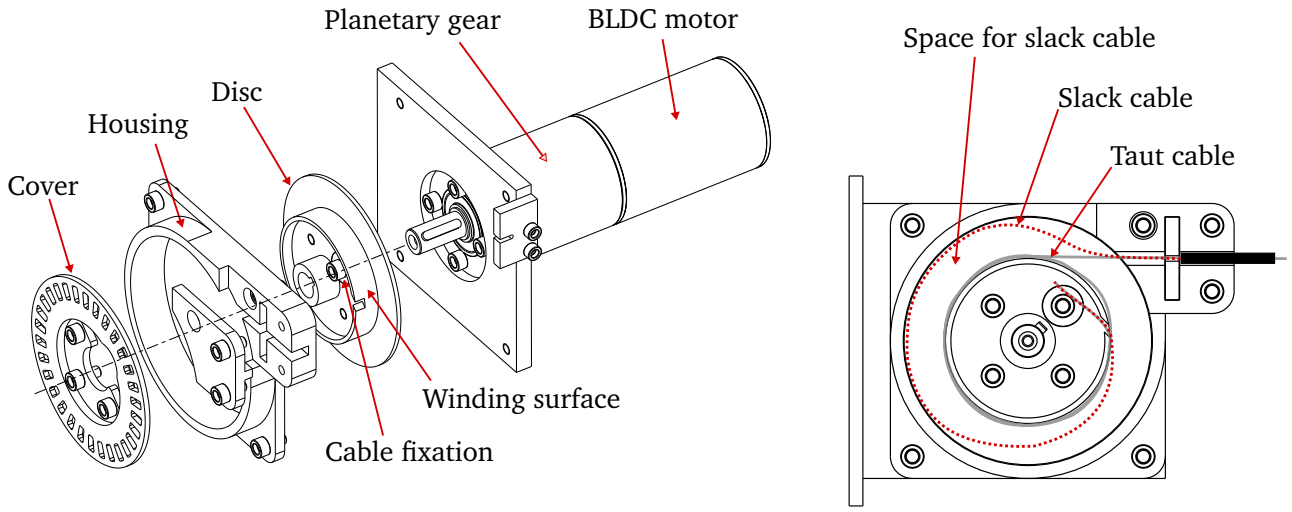

Figure 3.6.: Bowden cable actuator explosion with labeled components, and side view of the pulley: a situation with slack and a situation with taut inner cable is illustrated.

3.3. Actuator synthesis

After defining the basic setup of the AG and specifying individual parameters such as lever arms and disc radius, the next step is to find a suitable actuator for generating the desired torque and angle trajectories.

In a simple application such as steady operation, a motor and gearbox combination can be found by defining a single or few operating points, e.g. desired torque and speed. In dynamic applications, the resulting motor torque is determined by the desired output trajectories as well as the actuator parameters, e.g. the moment of inertia of the actuator. Therefore, an actuator design taking into account the desired output trajectories is necessary.

The following considerations are carried out for the AG, but can easily be transferred to the actuation of other body joints.

3.3.1. Modeling

In the following, the relationship between actuator variables and the desired load trajectories, i.e. the joint kinetics to be represented, is derived. A suitable reference axis for the synthesis of the actuator, i.e. the selection of the motor and the gearbox is either the motor shaft (i.e. the input of the gear) or the gear shaft (i.e. the output of the gear). With the knee and ankle lever arms and the disc radius specified, the torque and angle trajectories at the gear output axis are more or less defined. Furthermore, torque limitations of the gearbox are typically specified for the output shaft. Therefore, the gear output shaft is selected as a reference axis for the further modeling and design.

Given the ankle and knee angular velocities $\dot{\varphi}_{\mathrm{Ank}}$ and $\dot{\varphi}_{\mathrm{Knee}}$ as defined in Figure 2.1, the constant lever arms at ankle and knee r_{Ank} and r_{Knee}, and the radius of the Bowden cable actuator disc r_{Disc}, the disc angular velocity is

$$\dot{\varphi}_{\mathrm{Disc}} = \frac{r_{\mathrm{Ank}}\dot{\varphi}_{\mathrm{Ank}} - r_{\mathrm{Knee}}\dot{\varphi}_{\mathrm{Knee}}}{r_{\mathrm{Disc}}} \,. \tag{3.1}$$

This implies, that the Bowden cable is rigid, hence disc and end effector are rigidly coupled.

With $\kappa \in [0,1]$ indicating the relative portion of ankle torque M_{Ank} to be provided by the AG, and η_{Bow} being the Bowden cable efficiency, the load torque at the disc is

$$M_{\text{Disc}} = \frac{r_{\text{Disc}}}{r_{\text{Ank}}} \frac{\kappa M_{\text{Ank}}}{\eta_{\text{Bow}}} \,. \tag{3.2}$$

Let c_{M} be the motor torque constant, I be the motor current,

$$i_{\text{G}} = \frac{\varphi_{\text{M}}}{\varphi_{\text{Disc}}} > 1$$

be the gear ratio, and $J_{\text{M,tot}}$ be the total mass moment of inertia at the motor axis. With the motor torque

$$M_{\text{M}} = c_{\text{M}} I$$

the equation of motion at the motor axis is

$$J_{\text{M,tot}} \ddot{\varphi}_{\text{M}} = c_{\text{M}} I - \frac{M_{\text{Disc}}}{i_{\text{G}} \eta_{\text{Gear}}} \,, \tag{3.3}$$

which can be written as

$$i_{\text{G}} \underbrace{c_{\text{M}} I}_{=M_{\text{M}}} = \frac{M_{\text{Disc}}}{\eta_{\text{Gear}}} + \underbrace{J_{\text{M,tot}} i_{\text{G}}^2}_{=J_{\text{Disc,tot}}} \ddot{\varphi}_{\text{Disc}} \,. \tag{3.4}$$

In equation (3.4), the left side represents the motor torque M_{M} transformed to the disc axis. The right side consists of two terms, the load torque and the inertial torque. The total mass moment of inertia of the actuator reduced to the gear axis is

$$J_{\text{Disc,tot}} = i_{\text{G}}^2 \left(J_{\text{M}} + J_{\text{Gear}}\right) + J_{\text{Disc}} \,. \tag{3.5}$$

The inertia of motor and gear box J_{M} and J_{Gear} are typically provided by the manufacturer. The inertia of the disc J_{Disc} depends on the specific realization and is unknown during the synthesis of the actuator. As will be seen in the later realization, J_{Disc} is very small compared to the scaled motor torque $i_{\text{G}}^2 J_{\text{M}}$ and can therefore be neglected in the initial design. The validity of this assumption should be checked afterwards for the actual realization.

Equations (3.1) and (3.2) allow these terms to be fully expressed as a function of the desired joint kinetics. To specify the actuator parameters, one has to chose the gear ratio i_{G} and the torque constant of the motor c_{M}. Hence, with equations (3.1), (3.2) and (3.4) the load cycle can be represented in the speed-torque-diagram of the disc axis. The motor and gear output torque can be considered separately, taking into account the specific hardware limitations. Relevant dependencies and restrictions are discussed in the following.

3.3.2. Constraints and dependencies

Torque and speed are limited by component specific constant constraints and the speed-torque line of the motor. The various constraints and how they can be influenced are discussed next.

Component specific limitations

The following limitations must be taken into account when designing the actuator: First, the motion controller current is limited and therefore restricts the motor current. In the specific case, the motion controller continuous and peak currents are 20 A and 40 A, limiting the RMS and peak torque of the motor.

Second, the maximum output torque M_{Disc} and speed $\dot{\varphi}_{\mathrm{Disc}}$ of the gearbox are limited according to the manufacturer specifications. For both, torque and speed, typically maximum continuous torque and maximum intermittent torque at the gear are specified. Last, similar to the gear speed, the motor speed is limited by the manufacturer specifications as well as the supply voltage of the motion controller.

Torque and speed dependencies and limitations

To increase the actuator torque, the gear ratio can be increased, which comes at the cost of increased inertial torques. In general, in the given application the total actuator inertia $J_{\mathrm{Disc,tot}}$ is mainly determined by the motor inertia for higher gear ratios i_{G}.

Next to the gear ratio, the motor torque constant c_{M} can be increased. This is done by increasing the number of windings of the motor coil at the expense of thinner wires, which does two things: first, the winding resistance increases limiting the permissible current, and second, the speed constant c_{n} of the motor decreases. For DC and BLDC motors, the relation

$$c_{\mathrm{M}} c_{\mathrm{n}} = 1 \ .$$

holds [87]. By increasing c_{M} the induced voltage

$$U_{\mathrm{ind}} = c_{\mathrm{n}}^{-1} \dot{\varphi}_{\mathrm{M}} = c_{\mathrm{M}} \dot{\varphi}_{\mathrm{M}}$$

increases quicker with rising motor velocity $\dot{\varphi}_{\mathrm{M}}$. From the detailed power balance of the motor [88] or the electrical equivalent circuit equation [87], [89] the speed-torque line of the motor

$$U_{\mathrm{Mot}} = c_{\mathrm{M}} \dot{\varphi}_{\mathrm{M}} + \frac{R}{c_{\mathrm{M}}} M_{\mathrm{M}} \tag{3.6}$$

can be derived. Since the motor voltage is limited by the supply voltage $U_{\mathrm{Mot}} < U_{\mathrm{Sup}}$, speed and torque are limited by the straight line in the speed-torque diagram connecting the no load speed n_0 and the stall torque M_{Stall}. Both, n_0 and M_{Stall} are typically provided by the manufacturer. With the gear ratio, the speed-torque line can be transformed to the disc axis according to

$$U_{\mathrm{Mot}} = c_{\mathrm{M}} i_{\mathrm{G}} \dot{\varphi}_{\mathrm{Disc}} + \frac{R}{c_{\mathrm{M}}} \frac{M_{\mathrm{Disc}}}{i_{\mathrm{G}}} \leq U_{\mathrm{Sup}} \ . \tag{3.7}$$

Hence, next to the component specific limitations, the disc speed and torque is limited by the speed-torque line of the motor. The line can be vertically offset by increasing the supply voltage U_{Sup} and tilted by changing the gear ratio i_{G} and the motor torque constant c_{M}. All operation points of the load cycle must lie below the speed-torque line [87].

Figure 3.7 illustrates the relevant constraints for the actuator synthesis, originating from the component specific limitations as well as the motor parameters, and the dependencies between them in the speed-torque-diagram.

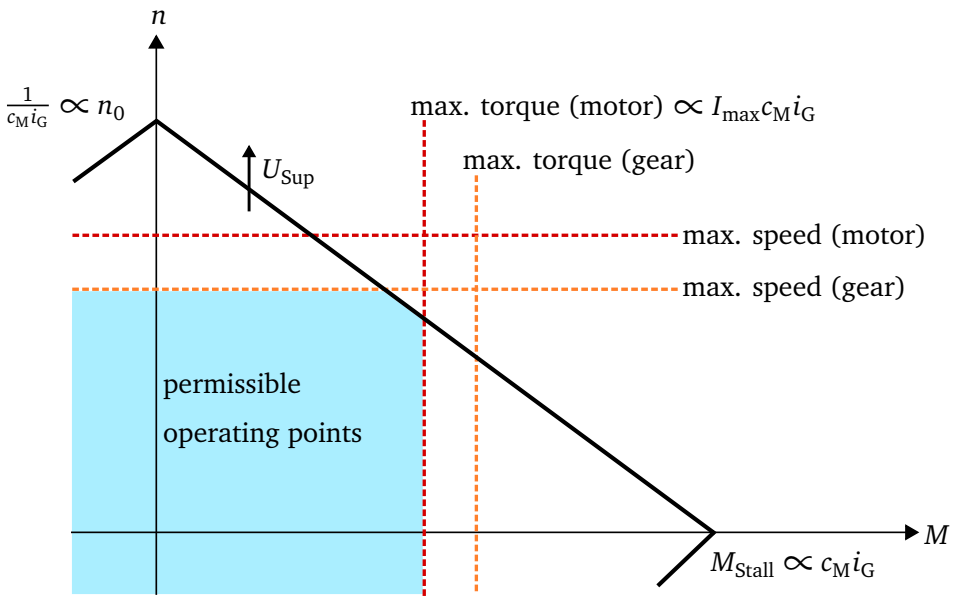

Figure 3.7.: Constraints and dependencies for actuator synthesis: The speed-torque line of a motor and gearbox (black), limitations of the motor (red), and limitations of the gearbox (orange)

Thermal limitations

The heating of the motor depends on the electrical resistance of the winding R, the RMS current I_{RMS}, and the thermal resistances between winding and housing $R_{th,1}$ as well as between housing and ambient $R_{th,2}$. The temperature difference between the winding and the ambient can then be calculated as

$$\Delta T_{Winding} = \frac{\left(R_{th,1} + R_{th,2}\right) R I_{RMS}^2}{1 - \alpha_{Cu}\left(R_{th,1} + R_{th,2}\right) R I_{RMS}^2} \tag{3.8}$$

where α_{Cu} is the resistance coefficient of copper [87]. The RMS current can be influenced by the actuator design, e.g. gear ratio and torque constant. The other parameters follow from the motor selection. While $R_{th,1}$ is determined by the design of the motor, the housing-ambient thermal resistance $R_{th,2}$ can be influenced by constructive modifications. Manufacturer guidelines in [88] state that mounting the motor to a good heat-conducting material can reduce $R_{th,2}$ by up to 80 %, whereby the actual reduction depends on the mounting conditions and must be determined on an application-specific basis.

Motor and gearbox are mounted to an aluminum plate. To further dissipate the heat from the motor, a heat sink is attached to the motor housing. In all following calculations, $R_{th,2}$ is therefore assumed to be reduced to 30 % of the value given in the manufacturers data sheet, which is a rather conservative guess compared to the manufacturer's instructions. The actual reduction of $R_{th,2}$ was not investigated, but during the pretests and experiments conducted within this thesis, no relevant heating of the actuator was noticed.

3.3.3. Actuator selection

The actuator was selected from BLDC motors from the manufacturers *maxon* (Alpnach Dorf, Switzerland) and *Faulhaber* (Schönaich, Germany). All BLDC motors with a rated power greater than 150 W available in

Table 3.1.: Assumptions and boundary conditions of the actuator synthesis

Parameter	Symbol	Value
Subject weight	m_{User}	80 kg
Walking speed		1.55 m s^{-1}
AG provided ankle torque	κ	50 %
Gear efficiency (component specific)	η_{Gear}	0.83
Assumed Bowden cable efficiency	η_{Bow}	0.5
Supply voltage	U_{Sup}	48 V
Ankle lever arm	r_{Ank}	80 mm
Knee lever arm	r_{Knee}	160 mm
Disc radius	r_{Disc}	>30 mm

12/2019 were considered in conjunction with the manufacturers matching gearboxes. The maximum rated power among the motors was 400 W.

During the selection process, it became clear that smaller diameter planetary gears cannot carry the expected load torques and are therefore not suitable. They might be relevant in a setup with synthetic cables and a smaller disc radius (resulting in smaller drive torques) or other additional gear stages. Furthermore, large gear ratios or motor diameters showed to significantly increase the inertial torques and therefore are unsuitable.

In the end, 30 motors from 8 model series were examined in detail. For each motor, a matching gearbox was selected such that the load cycle from equations (3.1), (3.2) and (3.4) best fits into the component specific constraints and the speed-torque line (3.7) as indicated in Figure 3.7. Furthermore, slight adaption of the disc radius r_{Disc} was allowed if necessary.

Table 3.1 lists all assumptions and constraints that were used for the actuator synthesis.

The motor and gear box combination which meets the requirements the best is a 180 W BLDC motor with a two staged planetary gearhead from *maxon*. The detailed components are listed below:

- Maxon BLDC motor EC-i 52 (nominal voltage 36 V, 180 W part number 578169)
- Maxon planetary gearhead GP 52 C (2 stages, gear ratio 12 : 1, part number 223083)

Although the gearbox is declared as 12 : 1, the actual gear ratio is $i_{\text{G}} = 49/4$. The resulting load cycle is displayed in Figure 3.8. The speed-torque trajectories are almost entirely within the area of permissible operating points and component-specific maximum torques and speeds are only marginally exceeded. Furthermore, the selected actuator has some reserve in speed, which is necessary in case of deviating kinematics or compliance occurring in the real system. The expected temperature increase of the winding is

$$\Delta T_{\text{Winding}} = 72\,^{\circ}\text{C}\,,$$

so that the maximum permissible winding temperature of 155 °C will not be exceeded.

3.4. Summary

To summarize, the given ROA prosthetic foot has been extended with an additional actuator with force application points similar to the biarticular gastrocnemius muscle. The force sensor measures the cable force and allows to estimate the applied knee and ankle torque.

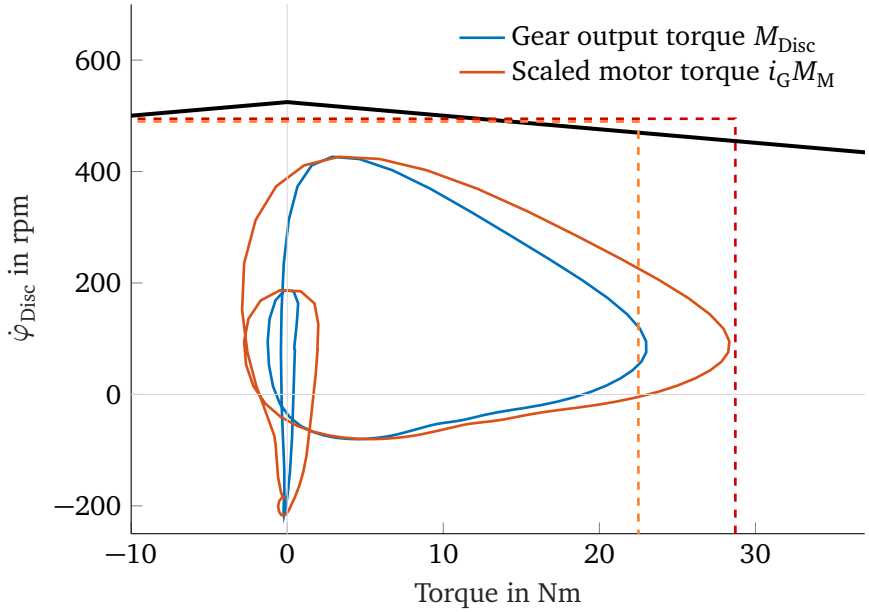

Figure 3.8.: Load cycle for the Motor EC-i 52-36V and 12 : 1 planetary gearhead GP 52. Dashed lines indicate the speed and torque limits of the gear (orange) and motor (red). The thick black line shows the speed-torque line of the motor

The actuator unit can represent 50 % of the ankle torque of an 80 kg subject walking at 1.55 m/s. While the subject weight is average, the speed is considered high for walking experiments with subjects with TTA. In actual (longer lasting) experiments the walking speed is expected to be lower. Therefore, the designed actuator can be considered capable to produce all relevant support patterns. Interestingly, of the evaluated motors, a medium-powered motor was the most suitable.

Table 3.2 lists the weight of all worn components. For subjects with TTA, the setup weighs between 4.26 kg and 4.52 kg, dependent on the weight of the individual prosthetic socket. This is up to two times heavier than the subjects individual passive prosthetic feet and about 1 kg heavier than the mass of the missing limb. For comparison, adding 1 kg of mass to the foot can increase the net metabolic cost of walking by up to 6 % [84].

When worn by unimpaired subjects with the help of the bypass, the additional weight is 5.5 kg. This weight is totally added to the constrained foot and shank. Due to this and the lateral and vertical displacement, the bypass is only considered suitable for technical testing purposes, but relevant biomechanical observations are unlikely to be observed.

Table 3.2.: Component weights of the hardware setups for subjects with transtibial amputation (TTA) and unimpaired subjects (bypass)

Component	Weight (TTA)	Weight (bypass)
Prosthetic socket (subject individual)	780 g to 1040 g	-
Orthotic bypass	-	1980 g
Knee orthosis, and thigh bracket	620 g	660 g
ROA prosthetic foot incl. pyramid adapter	2080 g	
Pacifica LP 9 carbon foot	300 g	
Foot cosmetic (size 28)	220 g	
Ankle lever incl. force sensor	150 g	
Bowden cable socket incl. 0.5 m outer cable	110 g	
Total setup weight	4260 g to 4520 g	5500 g

4. Modeling and identification

In the following, the dynamic equations describing both the ROA prosthesis and the Bowden cable actuator designed in Chapter 3 are derived and the model parameters are estimated by appropriate experiments. Both actuators can be modeled as serial elastic actuators. For the ROA prosthesis, special attention is paid to the nonlinear prosthesis kinematics in order to accurately determine the ankle torque from the installed angular encoders. For the purposes of controller design, the nonlinear ROA kinematic equations are linearized. In the case of the AG, the nonlinear stiffness resulting from the coupling to the user is examined in more detail and is then linearized for the purposes of the controller design. The investigations form the basis for the model-based torque controller design in Chapter 5.

For both actuators, the motor drives are operated in current control mode. The current control loop time constants are small enough and therefore current dynamics are neglected in the modeling and identification process. For the sake of readability sometimes, identical variable names are used for physical quantities of the individual actuators, e.g. φ_M for a motor angle. The associated physical meanings should be clear from the context. If confusion is possible, the indexes ROA and AG are used explicitly for the ROA prosthetic foot and the artificial gastrocnemius, respectively.

4.1. ROA prosthesis modeling

The prosthetic foot used in this work is Ruggedized Odysseus Ankle (ROA) from Springactive. It is a prototype from the predevelopment stage. The assembly and kinematics of the prosthesis are shown schematically in the Figure 4.1. It comprises a BLDC motor (maxon EC-4pole 30, part no. 305013), that is connected to a threaded shaft of a ballscrew via a pulley. The pitch of the ballscrew is 1 mm per revolution and the reduction ratio of the pulley is 2.44 : 1. The lever mechanism indicated in red in Figure 4.1 connects the nut of the ballscrew to a linear steel spring with a stiffness of $k_\mathrm{S} = 386\,000\,\mathrm{N/m}$. The spring is attached to the foot part of the prosthesis. The kinematic parameters l_F, l_x, l_y, r_1 and r_2 are fix and summarized in Table 4.1. Component parameters such as the spring stiffness k_S and the kinematic parameters are provided by the manufacturer [90].

In the following, all mechanical components of the ROA except for the steel spring are assumed to be rigid. Regarding the directions of counting, the following is assumed: Positive motor currents I tend to increase the motor angle φ_M. Increasing motor angles correspond to decreasing spindle lengths x_BS, which corresponds to an elongation of the spring, causing positive (plantar-flexing) ankle torque M_Ank. For better understanding, the translational motor position x_M is introduced such that

$$\dot{\varphi}_\mathrm{M} \propto \dot{x}_\mathrm{M} = -\dot{x}_\mathrm{BS}$$

Table 4.1.: Kinematic parameters of the ROA prosthesis

Parameter	l_x	l_y	l_F	r_1	r_2
Value	32 mm	95 mm	109.8 mm	40 mm	30 mm

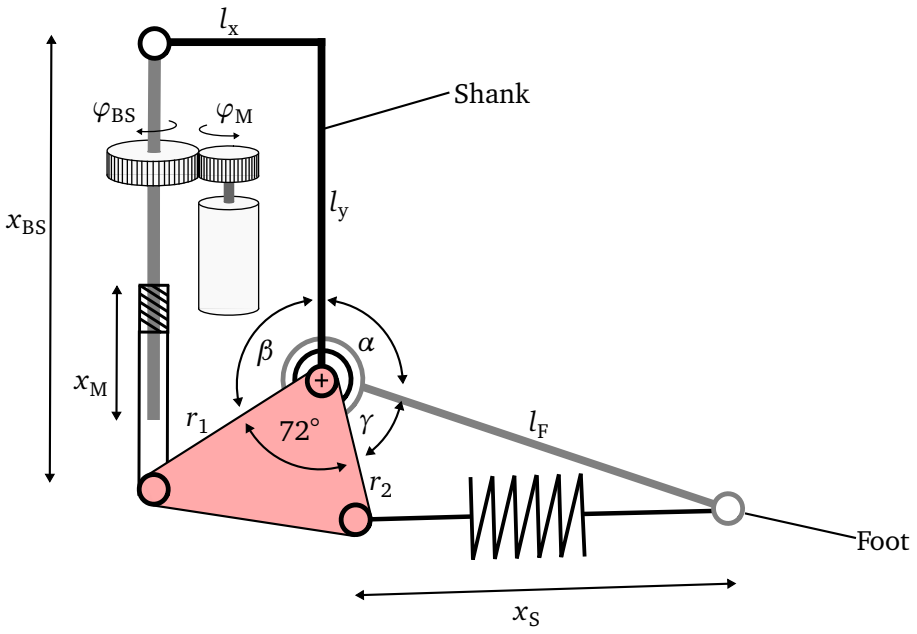

Figure 4.1.: Schematic structure of the ROA prosthetic foot with kinematic parameters and variables.

holds. The gear ratio of the pulley and ballscrew then is

$$i_{BS} = \frac{\dot{x}_M}{\dot{\varphi}_M} \,. \tag{4.1}$$

In the ROA prostheses, the position of the motor φ_M is measured with an incremental angular encoder (2048 cts/rev) and the ankle angle α is measured with a magnetic absolute angular encoder. The movement of the ballscrew nut is limited by upper and lower stops, and therefore the length of the spindle x_{BS} is limited between 84.5 mm and 124.5 mm [90]. After an initial run, the length of the spindle x_{BS} can thus be determined from the motor position φ_M. By measuring the motor position φ_M and the ankle angle α, it is possible to calculate β and γ shown in Figure 4.1, where γ can be used to calculate the length of the spring x_S. The deflection of the spring Δx_S and its effective lever arm then allow to estimate the prosthesis ankle torque. Therefore, the nonlinear kinematic of the prosthesis lever mechanism is investigated next.

4.1.1. Kinematics

The angles α, β, γ and the angle $\beta_L = 72°$ of the lever mechanism sum up to a complete circle

$$\alpha + \beta + \gamma + \beta_L = 360° \,. \tag{4.2}$$

To determine the angle β the rear quadrilateral is divided into two triangles as shown in Figure 4.2. Applying the law of cosines to the left triangle yields

$$x_{BS}^2 = l_x^2 + l_y^2 + r_1^2 - 2r_1\sqrt{l_x^2 + l_y^2}\cos\beta' \,, \tag{4.3}$$

from which the β can be determined as

$$\beta = \beta' + \arctan\frac{l_x}{l_y} = \arccos\left(\frac{l_x^2 + l_y^2 + r_1^2 - x_{BS}^2}{2r_1\sqrt{l_x^2 + l_y^2}}\right) + \arctan\frac{l_x}{l_y} \,. \tag{4.4}$$

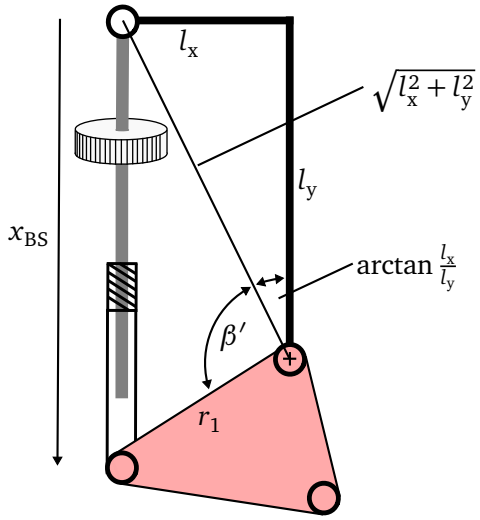

Figure 4.2.: Rear kinematic of the ROA prosthetic foot

Depending only on kinematic parameters and the length of the ball screw x_{BS}, β can be determined from the measured motor position φ_M. With α and β measured, γ can be determined from (4.2). Next, the spring length x_S is determined by applying the law of cosines to the foot segment triangle in Figure 4.1 and taking the square root

$$x_S = \sqrt{r_2^2 + l_F^2 - 2 r_2 l_F \cos\gamma} \, . \tag{4.5}$$

4.1.2. Kinetics

The equation of motion of the electric motor is

$$J\ddot{\varphi}_M = c_M I - M_{Fric} - i_{BS} F_M \, , \tag{4.6}$$

where J is the reflected mass moment of inertia on the motor axis, c_M is the torque constant of the Motor, I is the motor current, M_{Fric} is the friction torque at the motor axis, and F_M is the translational force in the ball screw. Since the drive train is assumed to be rigid, all friction torques and all mass moments of inertia can be reduced to the motor axis. The friction is assumed to be composed of viscous and Coulomb friction

$$M_{Fric} = d\varphi_M + M_C \mathrm{sign}\left(\dot{\varphi}_M\right) \, , \tag{4.7}$$

where d is the viscous friction and M_C is the Coulomb friction. Next, the force F_M in the ball screw will be expressed as a function of the ankle angle α and the motor angle φ_M. The force F_M appears in the equilibrium of moments at the lever mechanism

$$F_M h_M = F_S h_S = M_{Ank} \, , \tag{4.8}$$

where F_S is the force in the steel spring, M_{Ank} is the ankle torque, and h_S as well as h_M are the lever arms of the steel spring and the ballscrew with respect to the ankle joint. The lever arm h_S of the steel spring is calculated as the height of the lower triangle (see Figure 4.1)

$$h_S = \sqrt{r_2^2 - \left(\frac{l_F^2 - r_2^2 + x_S^2}{2x_S}\right)^2} \tag{4.9}$$

Table 4.2.: Variables in neutral position (sole ⊥ shank, spring relaxed)

Variable name	Variable	Value	Unit
Ankle angle	α_0	131.4	°
Ankle torque	$M_{\mathrm{Ank},0}$	0	N m
Spindle length	$x_{\mathrm{BS},0}$	103.5	mm
Spring length	$x_{\mathrm{S},0}$	95.65	mm
Angle (spindle)	β_0	101.9	°
Angle (spring)	γ_0	54.7	°
Motor lever	$h_{\mathrm{M},0}$	38.5	mm
Spring lever	$h_{\mathrm{S},0}$	28.1	mm
Motor current	I_0	0	A
Motor angle	$\varphi_{\mathrm{M},0}$	0	rad

and is a function of the spring length. Similar, the lever of the motor (or the ball screw, respectively) h_{M} is derived as

$$h_{\mathrm{M}} = \sqrt{r_1^2 - \left(\frac{x_{\mathrm{BS}}^2 + r_1^2 - l_{\mathrm{x}}^2 - l_{\mathrm{y}}^2}{2x_{\mathrm{BS}}}\right)^2} \,. \tag{4.10}$$

For a detailed derivation, see Section A.1 in the appendix. The resting length of the steel spring is $x_{\mathrm{S},0}$ and the spring characteristic is assumed to be linear with the spring rate k_{S}. Hence, the spring force

$$F_{\mathrm{S}} = k_{\mathrm{S}}\left(x_{\mathrm{S}} - x_{\mathrm{S},0}\right)$$

and the ankle torque is

$$M_{\mathrm{Ank}} = F_{\mathrm{S}} h_{\mathrm{S}} = k_{\mathrm{S}}(x_{\mathrm{S}} - x_{\mathrm{S},0}) \sqrt{r_2^2 - \left(\frac{l_{\mathrm{F}}^2 - r_2^2 + x_{\mathrm{S}}^2}{2x_{\mathrm{S}}}\right)^2} \,. \tag{4.11}$$

Here, M_{Ank} only depends on x_{S}, which can be calculated from the measured position φ_{M} and the measured ankle angle α as shown in the kinematic section Section 4.1.1. Therefore, the nonlinear kinematic and kinetic equations can be used to estimate the actual ankle torque of the ROA prosthesis, which is done so in all experiments carried out in this work. For the model based controller design they will be linearized in the next section.

4.1.3. Linearization

To derive a model for the controller design, the kinematic and kinetic equations derived in the previous section are linearized for the values in Table 4.2, which correspond to a neutral position of the prosthesis. In the neutral position, the prosthesis shank is approximately rectangular to the sole of the shoe, and the spring is relaxed, such that $F_{\mathrm{M}} = F_{\mathrm{S}} = 0\,\mathrm{N}$, $x_{\mathrm{S}} = x_{\mathrm{S},0}$ and $M_{\mathrm{Ank}} = 0\,\mathrm{N\,m}$. The motor current is $I = 0\,\mathrm{A}$ and the motor zero angle is defined as $\varphi_{\mathrm{M},0} = 0\,\mathrm{rad}$ in the neutral position.
The friction model (equation (4.7)) is linearized as $\Delta M_{\mathrm{Fric}} = d\,\Delta\dot{\varphi}_{\mathrm{M}}$, where the non-steady Coulomb term is neglected for the purposes of the linearization. Hence, the linearization of the motor equation of motion (4.6) results as

$$J\,\Delta\ddot{\varphi}_{\mathrm{M}} = c_{\mathrm{M}}\Delta I - d\,\Delta\dot{\varphi}_{\mathrm{M}} - i_{\mathrm{BS}}\Delta F_{\mathrm{M}} \,. \tag{4.12}$$

Linearizing the torque equilibrium equation (4.8) and solving for ΔF_M gives

$$\Delta F_\mathrm{M} = \frac{\Delta M_\mathrm{Ank}}{h_\mathrm{M,0}} = \frac{h_\mathrm{S,0} k_\mathrm{S}}{h_\mathrm{M,0}} \Delta x_\mathrm{S} \,. \tag{4.13}$$

Linearizing the spindle length (4.3) yields

$$\Delta x_\mathrm{BS} = \frac{r_1 \sqrt{l_\mathrm{x}^2 + l_\mathrm{y}^2} \sin \beta_0'}{x_\mathrm{BS,0}} \Delta \beta' = h_\mathrm{M,0} \Delta \beta \,, \tag{4.14}$$

where $\Delta \beta' = \Delta \beta$ and $\beta_0' = \beta_0 - \arctan \frac{l_\mathrm{x}}{l_\mathrm{y}}$. $h_\mathrm{M,0}$ is the linearized motor lever arm, which, even it is not obvious, can similarly be calculated from (4.10) with the help of (4.3). With the ballscrew gear reduction (4.1), equation (4.14) can be written as

$$\Delta \varphi_\mathrm{M} = \frac{h_\mathrm{M,0}}{-i_\mathrm{BS}} \Delta \beta \,. \tag{4.15}$$

Similar, linearization of the spring length (4.5) yields

$$\Delta x_\mathrm{S} = \frac{r_2 l_\mathrm{F} \sin \gamma_0}{x_\mathrm{S,0}} \Delta \gamma = h_\mathrm{S,0} \Delta \gamma \,,$$

which with the linearization of (4.2) $\Delta \gamma = -\Delta \alpha - \Delta \beta$ and (4.15) becomes

$$\Delta x_\mathrm{S} = h_\mathrm{S,0} \left(\frac{i_\mathrm{BS}}{h_\mathrm{M,0}} \Delta \varphi_\mathrm{M} - \Delta \alpha \right) . \tag{4.16}$$

Substituting equations (4.13) and (4.16) into (4.12) results in the linearized equation of motion of the ROA prosthesis

$$J \Delta \ddot{\varphi}_\mathrm{M} = c_\mathrm{M} \Delta I - d \Delta \dot{\varphi}_\mathrm{M} - \frac{i_\mathrm{BS}}{h_\mathrm{M,0}} h_\mathrm{S,0}^2 k_\mathrm{S} \left(\frac{i_\mathrm{BS}}{h_\mathrm{M,0}} \Delta \varphi_\mathrm{M} - \Delta \alpha \right) , \tag{4.17}$$

which is the ODE of a series elastic actuator. The belonging block diagram is shown in Figure 4.3 and the state space representation is

$$\begin{bmatrix} \Delta \dot{\varphi}_\mathrm{M} \\ \Delta \ddot{\varphi}_\mathrm{M} \end{bmatrix} = \begin{bmatrix} 0 & 1 \\ -\frac{i_\mathrm{BS}^2 h_\mathrm{S,0}^2 k_\mathrm{S}}{J h_\mathrm{M,0}^2} & -\frac{d}{J} \end{bmatrix} \begin{bmatrix} \Delta \varphi_\mathrm{M} \\ \Delta \dot{\varphi}_\mathrm{M} \end{bmatrix} + \begin{bmatrix} 0 \\ \frac{c_\mathrm{M}}{J} \end{bmatrix} \Delta I + \begin{bmatrix} 0 \\ -\frac{i_\mathrm{BS} h_\mathrm{S,0}^2 k_\mathrm{S}}{J h_\mathrm{M,0}} \end{bmatrix} \Delta \alpha \tag{4.18}$$

$$\Delta M_\mathrm{Ank} = \begin{bmatrix} \frac{i_\mathrm{BS} h_\mathrm{S,0}^2 k_\mathrm{S}}{h_\mathrm{M,0}} & 0 \end{bmatrix} \begin{bmatrix} \Delta \varphi_\mathrm{M} \\ \Delta \dot{\varphi}_\mathrm{M} \end{bmatrix} - h_\mathrm{S,0}^2 k_\mathrm{S} \Delta \alpha \,. \tag{4.19}$$

With $\Delta \varphi_\mathrm{M} = \frac{h_\mathrm{M,0}}{i_\mathrm{BS}} (-\Delta \beta)$ the ODE (4.17) can be transformed to the joint axis as

$$\underbrace{\frac{h_\mathrm{M,0}^2 J}{i_\mathrm{BS}^2}}_{=J_\beta} (-\Delta \ddot{\beta}) = \underbrace{\frac{h_\mathrm{M,0} c_\mathrm{M}}{i_\mathrm{BS}}}_{=c_{\mathrm{M},\beta}} \Delta I - \underbrace{\frac{h_\mathrm{M,0}^2}{i_\mathrm{BS}^2 d}}_{=d_\beta} (-\Delta \dot{\beta}) - \underbrace{h_\mathrm{S,0}^2 k_\mathrm{S}}_{=k_\beta} (-\Delta \beta - \Delta \alpha) \tag{4.20}$$

from which the torsional stiffness k_β, inertia J_β, damping d_β and the scaled motor constant $c_{\mathrm{M},\beta}$ of the ankle SEA can be read. Of particular interest is the torsional stiffness k_β for three reasons: first, k_β is a result of

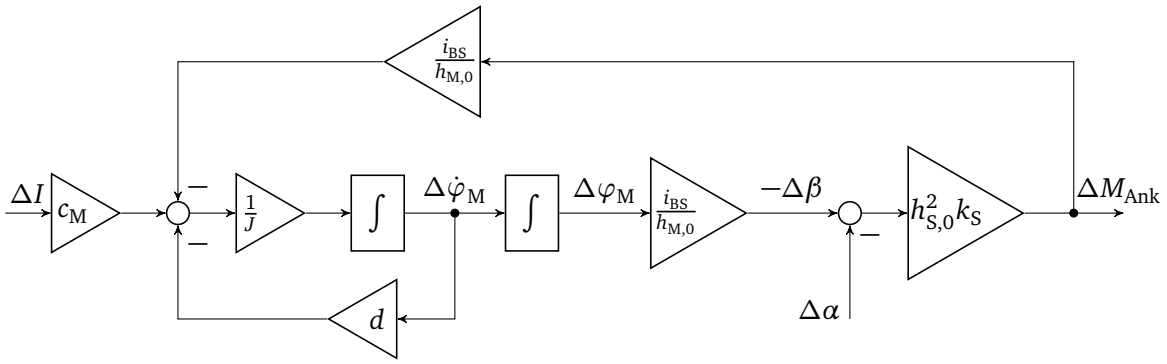

Figure 4.3.: Block diagram of the linearized ROA prosthesis

the prosthesis design process and is chosen to reduce motor power and energy requirements during walking. Second, the ankle stiffness plays a role in the kinematic analysis of human ankle biomechanics. Lastly, in case of powered prostheses the SEA is often used to render a desired impedance, where the performance is influenced by the impedance parameters of the SEA. In the neutral position, the torsional stiffness of the prosthesis at hand is

$$k_\beta = 305 \, \frac{\mathrm{N\,m}}{\mathrm{rad}} \, . \tag{4.21}$$

Normalized to the weight of an exemplary 80 kg user, this corresponds to a normalized ankle stiffness of approximately 3.8 N m/(rad kg).

4.2. Artificial gastrocnemius actuator modeling

The modeling of the AG Bowden cable actuator is described in Chapter 3 focusing on the dimensioning of the actuators capabilities to provide desired joint torques. The actuator unit applies torques to the knee and ankle joint simultaneously, which are related to the cable force F via the corresponding joint lever arms. Hence, with the translational force F being more generous, the AG is modeled as a translational system for the purposes of controller design. Additionally, it is assumed that the coupling to the user has elastic properties, resulting in a translational SEA. Besides many similarities, the modeling of the AG has some differences compared to that of the ROA. While the ROA prosthesis has a specified elasticity in form of a linear steel spring, the Bowden cable actuator's stiffness is composed of the stiffness of the cable and the interfering human tissue, which is assumed to be nonlinear. Further, the force in the AG is directly measured instead of being derived from the spring deflection. Modeling of the nonlinear kinematics as in the case of the prosthesis is not necessary.

Since the Bowden cable actuator can only generate pulling forces, but no pushing forces, it is technically a system with hybrid dynamics. This is ignored in the modeling similar to Chapter 3, and the inner cable is always assumed to be under tension, i.e. the cable force is greater than zero. Figure 4.4 shows a schematic representation of the AG Bowden cable actuator with the relevant kinematic and kinetic parameters.

With the translational cable position x and the motor angle φ_M, the total gear ratio of the actuator

$$\frac{\dot{x}}{\dot{\varphi}_M} = \frac{r_{Disc}}{i_G} \tag{4.22}$$

is composed of the disc radius r_{Disc} and the planetary gear reduction i_G. The equation of motion of the motor axis is

$$J\ddot{\varphi}_M = c_M I - M_{Fric} - \frac{r_{Disc}}{i_G} F \, , \tag{4.23}$$

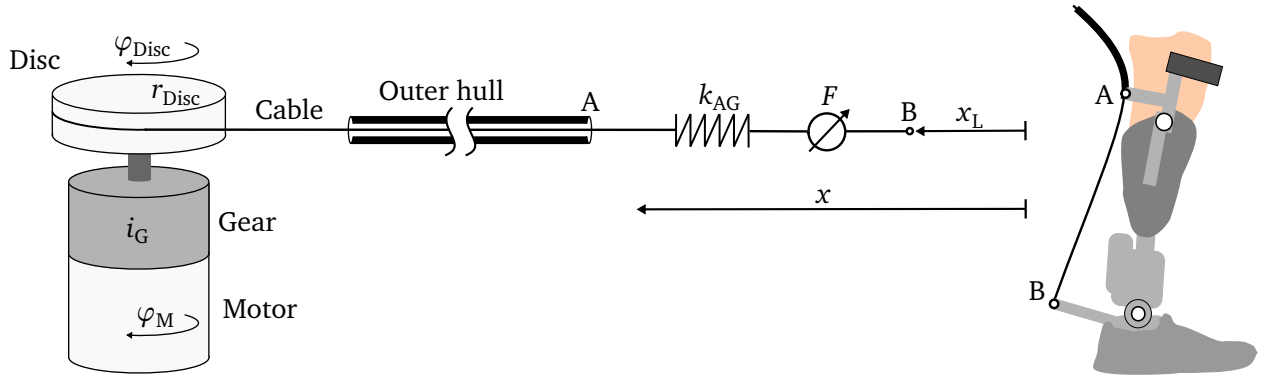

Figure 4.4.: Schematic representation of the artificial gastrocnemius with kinematic parameters and variables. The attachment points of the inner cable and outer hull are indicated with A and B.

where c_{M} is the torque constant of the motor, I is the motor current and J is the total inertia of motor, gear and disc reflected to the motor axis (see equation (3.3)). The friction is modeled as viscous friction d and Coulomb friction M_{C} similar to the ROA prosthetic foot.

The load force is assumed to be a function of the difference between translational cable position and the load deflection caused by knee and ankle movement $F = f(x - x_{\text{L}})$ and is linearized as

$$\Delta F = k_{\text{AG}}(\Delta x - \Delta x_{\text{L}}) = k_{\text{AG}}\left(\frac{r_{\text{Disc}}}{i_{\text{G}}}\Delta\varphi_{\text{M}} - \Delta x_{\text{L}}\right). \tag{4.24}$$

where k_{AG} is the linearized spring rate of the AG. What follows is the linearized ODE of the AG hesen

$$J\Delta\ddot{\varphi}_{\text{M}} = c_{\text{M}}\Delta I - d\Delta\dot{\varphi}_{\text{M}} - k_{\text{AG}}\frac{r_{\text{Disc}}}{i_{\text{G}}}\left(\frac{r_{\text{Disc}}}{i_{\text{G}}}\Delta\varphi_{\text{M}} - \Delta x_{\text{L}}\right) \tag{4.25}$$

with the corresponding block diagram in Figure 4.5 and the state space representation

$$\begin{bmatrix}\Delta\dot{\varphi}_{\text{M}}\\ \Delta\ddot{\varphi}_{\text{M}}\end{bmatrix} = \begin{bmatrix}0 & 1\\ -\frac{k_{\text{AG}}r_{\text{Disc}}^2}{Ji_{\text{G}}^2} & -\frac{d}{J}\end{bmatrix}\begin{bmatrix}\Delta\varphi_{\text{M}}\\ \Delta\dot{\varphi}_{\text{M}}\end{bmatrix} + \begin{bmatrix}0\\ \frac{c_{\text{M}}}{J}\end{bmatrix}\Delta I + \begin{bmatrix}0\\ -\frac{k_{\text{AG}}r_{\text{Disc}}}{Ji_{\text{G}}}\end{bmatrix}\Delta x_{\text{L}} \tag{4.26}$$

$$\Delta M_{\text{Ank}} = \begin{bmatrix}\frac{k_{\text{AG}}r_{\text{Disc}}}{i_{\text{G}}} & 0\end{bmatrix}\begin{bmatrix}\Delta\varphi_{\text{M}}\\ \Delta\dot{\varphi}_{\text{M}}\end{bmatrix} - k_{\text{AG}}\Delta x_{\text{L}}\,. \tag{4.27}$$

To conclude, the nonlinear and linearized equations of motions of the ROA prosthesis and the AG have been derived, resulting in fairly similar systems. In the stationary operating point, the cable force is $F_0 \geq 0\,\text{N}$ and the current I_0 results from the nonlinear output stiffness, which is to be identified. The load position $x_{\text{L},0}$ is assumed to be 0 m and the stationary positions x_0 and $\varphi_{\text{M},0}$ are chosen to match the spring characteristic. Except for F_0, the variable values in the stationary operating point play no role in the controller design carried out in later chapters. Based on this, the model parameters of both actuators will be identified next.

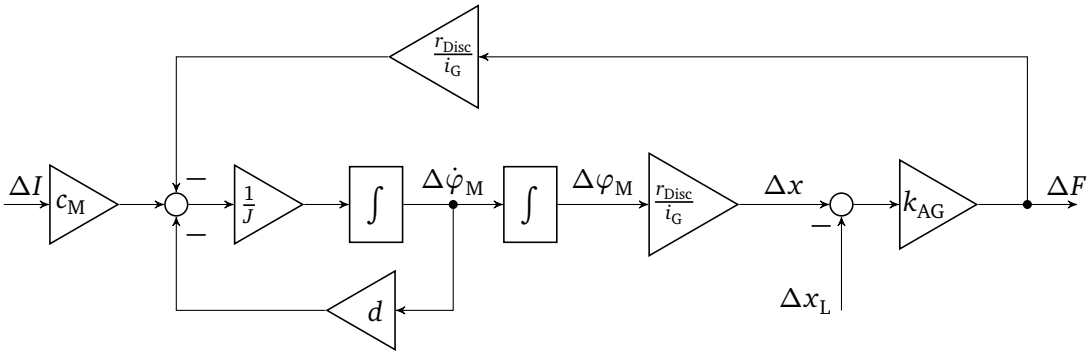

Figure 4.5.: Block diagram of the linearized artificial gastrocnemius

4.3. Identification

In this section, the identification of the model parameters for the ROA and the AG are described. For both actuators, the torque constants of the motors are available from the data sheets, and the effective gear ratios are known from the modeling process.

In case of the ROA, the stiffness of the steel spring is provided by the manufacturer. This leaves the friction parameters and the total inertia of the drive train open to be identified. For the AG, the friction parameters and the total inertia of the AG drive train are determined. Lastly, the stiffness of the user interface is investigated.

Suitable experiments are introduced to determine individual parameters in isolation. In the case of the ROA, the ROM is limited by the restricted travel of the ballscrew, whereas the design of the AG allows the Bowden cable to be detached and the drive unit to be examined independently of the user interface. Some of the experiments require the motor velocity, the motor position, or the AG output force to be controlled. A procedure to derive the required controllers fulfilling the requirements of the identification procedure without particular knowledge of the model parameters is provided in the appendix Section A.2.

4.3.1. ROA friction

To determine the friction parameters of the ROA, it is examined under no-load conditions ($M_{\mathrm{Ank}} = 0$), such that the nonlinear equation of motion (4.6) results in

$$J\ddot{\varphi}_{\mathrm{M}} = c_{\mathrm{M}} I - M_{\mathrm{Fric}} \,. \tag{4.28}$$

It can be assumed that the friction torque depends solely on the motor velocity. At constant velocity, the left side of the equation is zero and the friction torque equals motor torque . Two options to operate the actuator at constant speed are available:

- Constant currents are applied and the motor speed is measured.
- The motor speed is controlled and the resulting input current is measured.

In the constant current setting, constant speeds cannot be achieved in the low speed range due to small position dependent variations of the friction torque. Further, high currents easily result in motor speeds above the component limitations. In the speed-controlled mode, it is easier to set the relevant speeds and lower speeds can be applied.

To determine the friction parameters of the ROA, the actuator is moved at constant speeds between the stops of the ballscrew. In order to prevent crashes for higher speeds, it is more practical to follow ramped

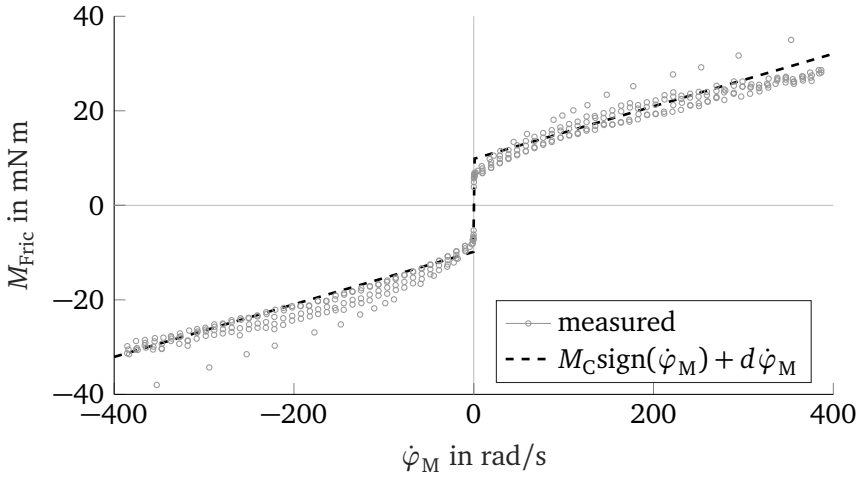

Figure 4.6.: Measured (grey dots) friction at the ROA motor axis and least squares fit (black dashed)

reference position trajectories using position control. Current and motor velocity are then averaged during periods of constant speed. For very low speeds ($|\dot{\varphi}_{\mathrm{M}}| \leq 1\,\mathrm{rad/s}$), the angular velocity of the motor is PI controlled.

Figure 4.6 shows the result of multiple repetitions in the relevant velocity range. The friction exhibits viscous behavior and a prominent Coulomb part. Towards higher velocities, the increase in friction slightly decreases. Contrary to expectations, there is no increase in friction torque for $\dot{\varphi}_{\mathrm{M}} \to 0$, as it is known from the Stribeck friction model. This observation is comparable to observations in the literature [91], [92] and is due to dominant rolling losses in the bearings of the motor and the ball screw. Least squares fitting of the model of viscous and coulomb friction $M_{\mathrm{Fric}} = M_{\mathrm{C}}\mathrm{sign}(\dot{\varphi}_{\mathrm{M}}) + d\dot{\varphi}_{\mathrm{M}}$ to the data points yields the friction parameters

$$\begin{aligned} M_{\mathrm{C}} &= 9.8 \cdot 10^{-3}\,\mathrm{N\,m} \\ d &= 0.056 \cdot 10^{-3}\,\frac{\mathrm{N\,m\,s}}{\mathrm{rad}}\,. \end{aligned}$$

The few outliers in the data stem from an initial separate run, whereas the majority of the data points were measured in a single run with the ball screw and bearings warmed up. While the Coulomb friction does not change noticeably, the outliers indicate that the viscous friction coefficient may vary by a factor of 2. An increase of the Coulomb friction can be expected under loaded conditions, since static friction is known to be proportional to the normal forces [91, p. 59], which increase under load.

4.3.2. ROA inertia

In the equation of motion, the inertia J occurs as the coefficient of the angular acceleration $\ddot{\varphi}_{\mathrm{M}}$ and therefore influences transient motions of the actuator. Hence, the inertia J is estimated from current step responses with the prosthesis being able to move freely, i.e. $M_{\mathrm{Ank}} = 0$. Since the sign of the motor velocity $\dot{\varphi}_{\mathrm{M}}$ does not change during the step response, the friction is simplified to $M_{\mathrm{Fric}}(\dot{\varphi}_{\mathrm{M}}) = M_{\mathrm{C}} + d\dot{\varphi}_{\mathrm{M}}$, and the step response of motor velocity $\dot{\varphi}_{\mathrm{M}}(t)$ from (4.6) for $I(t) = I\sigma(t)$ becomes

$$\dot{\varphi}_{\mathrm{M}}(t) = \dot{\varphi}_{\mathrm{M},0}\,\mathrm{e}^{\frac{-d}{J}t} + \frac{c_{\mathrm{M}}I - M_{\mathrm{C}}}{d}\left(1 - \mathrm{e}^{\frac{-d}{J}t}\right), \quad t \geq 0\,.$$

The friction parameters M_C and d influence the steady state, whereas $\frac{d}{J}$ defines transient behavior. With the measured motor velocities $\dot{\varphi}_{M,meas}$ and estimated $\dot{\varphi}_{M,est}$, the model parameters can be estimated from output error minimization. It turns out that optimizing only J to match a measured step response while assuming M_C and d from the friction estimation results in bad fits with J varying dependent on the step height indicating nonlinearity. This observation probably originates from the velocity dependence of the friction parameters, which is also observed during the friction identification Figure 4.6. Nonetheless, a linear model is assumed to be accurate enough. Therefore, all three of the parameters $\theta = [J, d, M_C]$ are estimated simultaneously from output error minimization. To do so, the integrated squared output error is minimized over multiple ($n > 2$) step responses with different step heights I_k

$$\theta = \arg\min_{\theta} \sum_{k=1}^{n} \int_0^{t_{end,k}} \left(\dot{\varphi}_{M,k,meas}(t) - \dot{\varphi}_{M,k,est}(t, I_k, \theta)\right)^2 . \tag{4.29}$$

For the identification, three positive and three negative step responses with different height are recorded. The step heights of ±2 A, ±2.5 A, and ±3 A were chosen to allow the actuator to reach steady state velocity within the available travel distance of the ballscrew. To determine θ, problem (4.29) is solved 100 times picking three random measurements. This is done to gain insight into the uncertainty of the model parameters θ. The resulting mean parameters and standard deviations are

$$\begin{aligned} J &= (6.38 \pm 0.66) \cdot 10^{-6} \mathrm{kg\,m^2} \\ M_C &= (13.4 \pm 2.8) \cdot 10^{-3} \mathrm{N\,m} \\ d &= (0.069 \pm 0.009) \cdot 10^{-3} \frac{\mathrm{N\,m\,s}}{\mathrm{rad}} . \end{aligned}$$

As can be seen, the standard deviations of the inertia J and damping d are a magnitude smaller than the corresponding model parameters, indicating a consistent estimation of the parameters of the linear model. Figure 4.7 exemplarily shows measured and estimated motor velocity for the $n = 3$ positive step responses. The Coulomb friction M_C and viscous damping d turn out to be approximately one standard deviation higher than in the previous friction identification. This can be explained by the bearings having warmed up during the friction identification, but not during the step responses. For the further purposes of system analysis and controller design, the friction parameters from the pure friction identification and the inertia gained from the step responses are utilized.

4.3.3. AG friction

Similar to the ROA, the friction of AG is estimated based on the corresponding nonlinear equation of motion (4.23). To do so, the Bowden cable is detached, allowing the motor and gearbox to move freely. The motor velocities of interest are commanded using the PI velocity control derived in the appendix Section A.2. The least squares fitted friction parameters are

$$\begin{aligned} M_C &= 18.8 \cdot 10^{-3} \mathrm{N\,m} \\ d &= 0.061 \cdot 10^{-3} \frac{\mathrm{N\,m\,s}}{\mathrm{rad}} . \end{aligned}$$

and the measured and fitted data is shown in Figure 4.8.

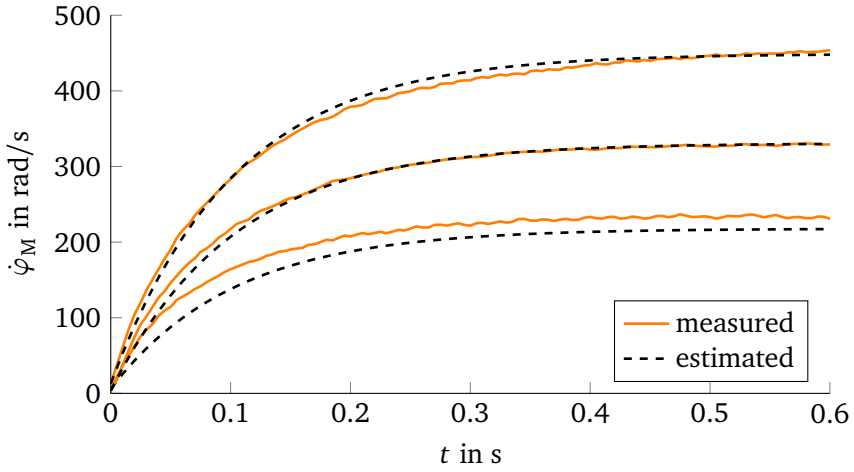

Figure 4.7.: Step responses of the ankle joint prosthesis motor angular velocity $\dot{\varphi}_M$ for multiple input current steps with a step height of 2 A, 2.5 A, and 3 A and fits from the output error minimization

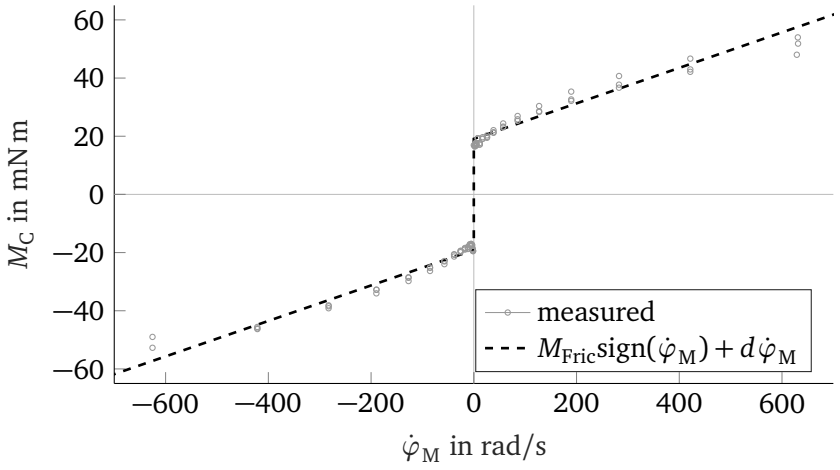

Figure 4.8.: Measured friction (grey dots) of the AG and least squares fit (solid black) consisting of coulomb and viscous friction.

4.3.4. AG inertia

The actuator inertia J comprises the inertia of the motor J_{M}, gearbox J_{Gear} and the reflected inertia of the winding disc J_{Disc} (see equation (3.5))

$$J = J_{\mathrm{M}} + J_{\mathrm{Gear}} + \frac{J_{\mathrm{Disc}}}{i_{\mathrm{G}}^2} \, .$$

J_{M} and J_{Gear} are provided in the manufacturers datasheet. The inertia of the aluminum disc can be approximated as the mass moment of inertia of a cylinder, or be taken from the CAD model. It turns out that the total inertia at the motor axis

$$J = 19.2 \cdot 10^{-6} \,\mathrm{kgm}^2 \tag{4.30}$$

is dominated by the inertia of the motor, which is $J_{\mathrm{M}} = 17 \cdot 10^{-6} \,\mathrm{kgm}^2$.

4.3.5. AG stiffness

The stiffness of the AG is composed of the stiffness of the cable, the carbon foot and the interfering human tissue at the thigh bracket. It is estimated for unimpaired subjects with the help of the orthotic bypass presented in Section 3.2.3. The bypass is expected to have a similar effect on stiffness as a prosthetic stem in an individual with TTA, and both setups are expected to affect stiffness less than the remaining mechanical components and interfering human tissue. In addition, changes in stiffness are expected as a result of the individual physique of the subject, which must be dealt with by the force control system to be designed. Including a subject in the experimental setup is important to characterize the full dynamics of the human-machine system.

The stiffness is estimated for two unimpaired subjects with the following body characteristics.

- subject A: male, 1.93 m, 86 kg, body mass index 22.8 $\mathrm{kg/m}^2$
- subject B: male, 1.83 m, 65 kg, body mass index 19.4 $\mathrm{kg/m}^2$

During the identification experiment, the subjects stand with their legs extended, hold on to a railing and the entire surface of the shoe sole maintains permanent contact with the ground. Triangular-shaped reference (5 ... 250 ... 5 N) forces are commanded to the AG Bowden cable actuator, while the ROA prosthetic foot is commanded to produce zero ankle torque. The peak force was chosen such that, first, the forces to be expected in the walking experiments are covered and, second, the subject can comfortably hold the leg straight. During the application of the force profiles, the Bowden cable deflection is measured to estimate the AG stiffness. Pretests with an early prototype in [93] showed, that there was no difference in the loading curves between straight ($\varphi_{\mathrm{Knee}} = 180°$) and bent knee ($\varphi_{\mathrm{Knee}} = 140°$).

For the experimental procedure described above, a force controller is needed. In a first iteration, this can be designed as a P-P cascade controller without exact knowledge of the model parameters, as explained in appendix A.2. With this controller, stick-slip behavior occurs in the cable position, especially for higher forces. Nonetheless, an initial identification of the stiffness is possible from the obtained measurements. The quality of the ramped force profiles increases with the performance of the force controller. For the present measurement, a PI-control with state feedback, as described in Chapter 5, was used. The controller allows the application of smooth force profiles.

Figure 4.9, top, shows the measured force and cable deflection for 13 loading and unloading cycles for subject A, whereby the actuator position x is reset to 0 in each cycle once the force is minimal (5 N). This is done to compensate for small changes in the leg posture over the course of the identification experiment. An approximately linear profile is observed during loading and a curved profile during unloading. Similar

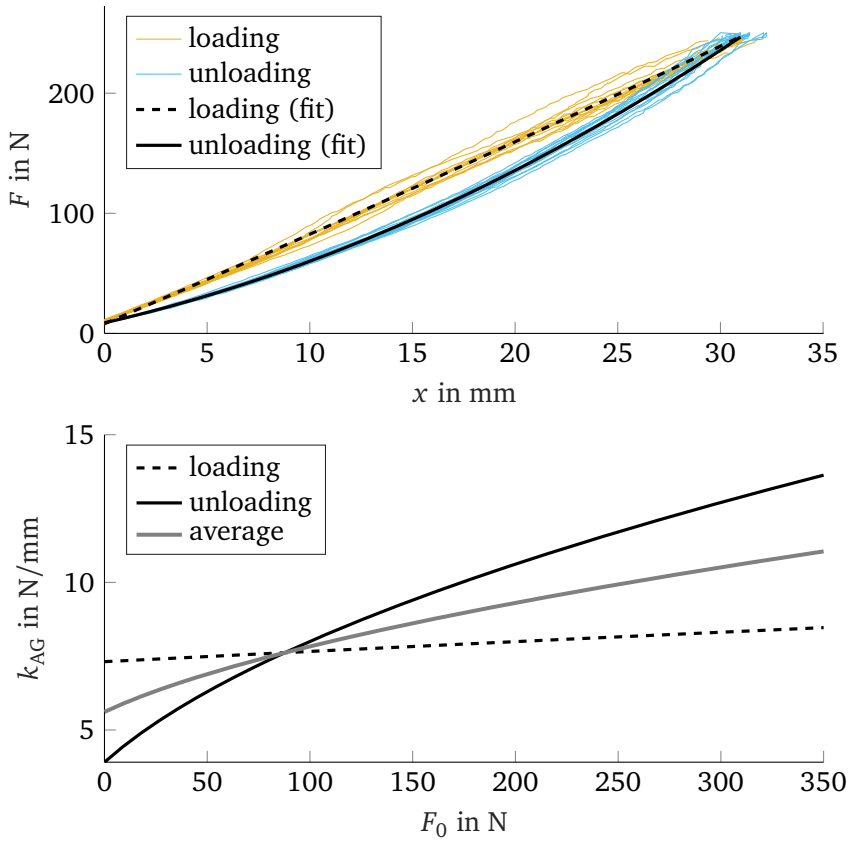

Figure 4.9.: Top plot: Force and actuator position measured during ramp-shaped loading (orange) and unloading (blue) with corresponding fitted nonlinear spring characteristic (dashed, solid). Multiple repetitions for subject A. Bottom plot: linearized spring stiffness over actuator force F_0 for loading (dashed) and unloading curve (solid black) and average (solid grey)

profiles were observed in [94] for the characterization of a soft exosuit with biarticular actuation at knee and ankle.

A quadratic spring

$$F = a_2 x^2 + a_1 x + a_0 \tag{4.31}$$

is fitted to the measurements, where F is the measured force and x is the Bowden cable deflection. The linearized output stiffness of the AG is

$$k_{\mathrm{AG}} = \left.\frac{\mathrm{d}F}{\mathrm{d}x}\right|_{x_0} = 2a_2 x_0 + a_1 \,, \tag{4.32}$$

where x_0 denotes the cable deflection at a stationary working point. Furthermore, let F_0 denote the cable force at a stationary working point. With

$$x_0 = \frac{-a_1}{2a_2} + \sqrt{\frac{a_1^2}{4a_2^2} + \frac{F_0}{a_2}} \tag{4.33}$$

the linearized stiffness k_{AG} can be expressed as a function of the cable force F_0 according to

$$k_{\mathrm{AG}} = \sqrt{a_1^2 + 4a_2 F_0} \,. \tag{4.34}$$

Figure 4.9, bottom, shows the estimated stiffness coefficient k_{AG} for subject A as a function of the cable force F_0. The averaged stiffness parameters for loading and unloading for subject A and B are:

- Subject A: $a_2 = 67\,000\,\mathrm{N/m^2}$, $a_1 = 5600\,\mathrm{N/m}$,
- Subject B: $a_2 = 45\,000\,\mathrm{N/m^2}$, $a_1 = 6000\,\mathrm{N/m}$.

The forces in walking experiments are expected to be in a range between 0 N and 400 N. For both subjects, a force of $F_0 = 100\,\mathrm{N}$, which is a medium force expected during walking, results in a linear stiffness of about $k_{\mathrm{AG}} \approx 8000\,\mathrm{N/m}$. The minimum stiffness is about 4000 N/m for forces near 0 N, while the stiffness for high forces ($F_0 = 350\,\mathrm{N}$) reaches values of up to 14 000 N/m.

4.4. Summary

Modeling and identification of the model parameters of both actuators, the ROA prosthetic foot and the AG, were carried out in this chapter. In the case of the ROA, the nonlinear kinematics are modeled and linearized. The nonlinear kinematics are used to determine the ankle torque from the installed sensors, while the linearized model can be used for the controller design in the following chapters. For the AG, special attention is given to the nonlinear output stiffness, which varies depending on the subjects physique as well as the actual cable force.

As can be seen from the block diagrams of the linearized systems, both actuators represent an SEA. With the gear parameter q, the unified system representation can be introduced as in Figure 4.10. Here, the output M corresponds to either the ROA torque or the AG force, and the disturbance φ_L corresponds to either $\Delta\alpha$ or Δx_L. The associated model parameters of both actuators as well as their sources are listed in Table 4.3.

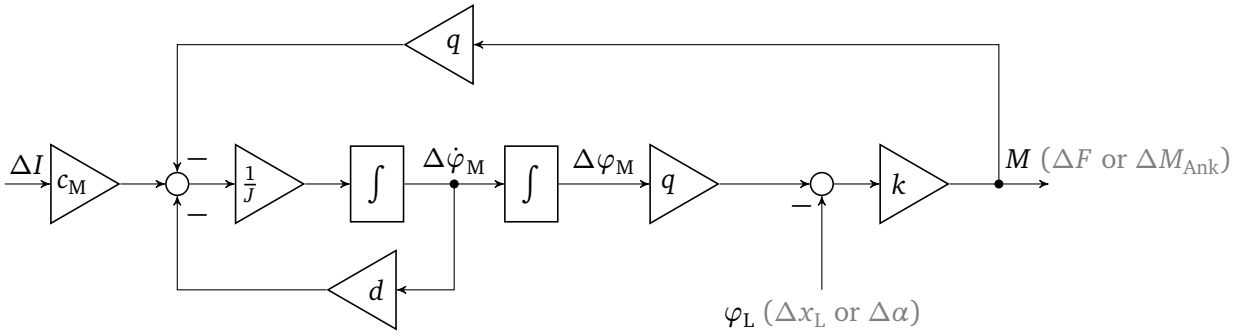

Figure 4.10.: Unified SEA block diagram

The corresponding state space model is

$$\begin{bmatrix}\Delta\dot{\varphi}_\mathrm{M}\\ \Delta\ddot{\varphi}_\mathrm{M}\end{bmatrix}=\begin{bmatrix}0 & 1\\ -\frac{q^2k}{J} & -\frac{d}{J}\end{bmatrix}\begin{bmatrix}\Delta\varphi_\mathrm{M}\\ \Delta\dot{\varphi}_\mathrm{M}\end{bmatrix}+\begin{bmatrix}0\\ \frac{c_\mathrm{M}}{J}\end{bmatrix}\Delta I+\begin{bmatrix}0\\ \frac{qk}{J}\end{bmatrix}\varphi_\mathrm{L}$$

$$M=\begin{bmatrix}qk & 0\end{bmatrix}\begin{bmatrix}\Delta\varphi_\mathrm{M}\\ \Delta\dot{\varphi}_\mathrm{M}\end{bmatrix}-k\varphi_\mathrm{L}$$

and the Laplace transfer function is

$$M(s)=\frac{qkc_\mathrm{M}}{Js^2+ds+q^2k}\Delta I(s)+\frac{-kJs^2-kds}{Js^2+ds+q^2k}\varphi_\mathrm{L}\,.$$

For the ROA, the linearized model with the parameters from Table 4.3 is

$$\begin{bmatrix}\Delta\dot{\varphi}_\mathrm{M}\\ \Delta\ddot{\varphi}_\mathrm{M}\end{bmatrix}=\begin{bmatrix}0 & 1\\ -137 & -8.78\end{bmatrix}\begin{bmatrix}\Delta\varphi_\mathrm{M}\\ \Delta\dot{\varphi}_\mathrm{M}\end{bmatrix}+\begin{bmatrix}0\\ 2130\end{bmatrix}\Delta I+\begin{bmatrix}0\\ 81000\end{bmatrix}\Delta\alpha$$

$$\Delta M_\mathrm{Ank}=\begin{bmatrix}0.517 & 0\end{bmatrix}\begin{bmatrix}\Delta\varphi_\mathrm{M}\\ \Delta\dot{\varphi}_\mathrm{M}\end{bmatrix}-305\Delta\alpha$$

and the Laplace transfer function

$$\Delta M_\mathrm{Ank}(s)=\frac{1100}{s^2+8.78s+137}\Delta I(s)+\frac{-305s^2-2680s}{s^2+8.78s+137}\Delta\alpha(s)$$

Table 4.3.: Parameters of the unified linearized SEA model for the ROA prosthetic foot and the artificial gastrocnemius (AG)

Actuator	Variable		Value	Unit	Source
ROA	Motor constant	c_M	0.0136	N m/A	Datasheet
	Inertia	J	$6.38 \cdot 10^{-6}$	kg m^2	Identification
	Viscous damping	d	$0.056 \cdot 10^{-3}$	N m s/rad	Identification
	Coulomb friction	M_C	$9.8 \cdot 10^{-3}$	N m	Identification
	Gear ratio	$q = i_\mathrm{BS} h_\mathrm{M,0}^{-1}$	0.00160	-	Kinematic model
	Spring stiffness	$k = h_\mathrm{S,0}^2 k_\mathrm{S}$	305	N m/rad	Manufacturer
AG	Motor constant	c_M	0.0706	N m/A	Datasheet
	Inertia	J	$19.2 \cdot 10^{-6}$	kg m^2	Datasheet + CAD
	Viscous damping	d	$61 \cdot 10^{-6}$	N m s/rad	Identification
	Coulomb friction	M_C	$19.1 \cdot 10^{-3}$	N m	Identification
	Gear ratio	$q = r_\mathrm{Disc} i_\mathrm{G}^{-1}$	$3/1225 \approx 0.00245$	m/rad	Datasheet + CAD
	Spring stiffness	k	8000	N/m	Identification

has two moderately damped poles

$$s = -4.39 \pm 10.9j \ .$$

For the AG, the linearized model with the parameters from Table 4.3 is

$$\begin{bmatrix} \Delta\dot{\varphi}_\mathrm{M} \\ \Delta\ddot{\varphi}_\mathrm{M} \end{bmatrix} = \begin{bmatrix} 0 & 1 \\ -2495 & -3.172 \end{bmatrix} \begin{bmatrix} \Delta\varphi_\mathrm{M} \\ \Delta\dot{\varphi}_\mathrm{M} \end{bmatrix} + \begin{bmatrix} 0 \\ 3670 \end{bmatrix} \Delta I + \begin{bmatrix} 0 \\ 1.02 \cdot 10^6 \end{bmatrix} \Delta x_\mathrm{L}$$

$$\Delta F = \begin{bmatrix} 19.6 & 0 \end{bmatrix} \begin{bmatrix} \Delta\varphi_\mathrm{M} \\ \Delta\dot{\varphi}_\mathrm{M} \end{bmatrix} - 8000 \Delta x_\mathrm{L}$$

and the Laplace transfer function

$$\Delta F(s) = \frac{71900}{s^2 + 3.17s + 2500} \Delta I(s) + \frac{-8000s^2 - 25400s}{s^2 + 3.17s + 2500} \Delta X_\mathrm{L}(s)$$

has two weakly damped poles

$$s = -1.59 \pm 49.9j \ .$$

With the models of both actuators derived, model-based controllers for the actuators can be designed in the next chapter.

5. Torque control for series elastic actuators

As derived in the preceding chapter, ROA prosthetic foot and AG both represent series elastic actuators which can be described identically using the system equations and the block diagrams presented in Section 4.4. In this chapter, the low-level torque control of both actuators is approached. The goal is that both actuators behave like ideal torque sources from the perspective of the high-level control.

For this purpose, first, the requirements for the low level torque control will be derived based on the human reference ankle behavior. For the controller design, the SEA model from Section 4.4 will be transformed to make use of the measured variables available in both actuators. A torque control scheme consisting of a model based feedforward control and feedback controller is introduced, the controller tuning is described based on simulation results and the resulting controllers are given. Finally, a suitable feedback anti-windup is derived and the potential occurrence of slack rope in the AG is addressed.

Torque control requirements

Cyclic walking control applications are often addressed with iterative control approaches, allowing to improve the tracking performance and to compensate cyclic disturbances. Limitations for these approaches are posed by the variability of human gait; in the specific case of level walking by variability of cadence and joint trajectories. This inherent variability of human gait is expected to increase when subjects are exposed to new or varying prosthetic support patterns during the walking experiments.

A feedback controller with appropriate closed loop bandwidth is a suitable approach to deal with varying reference trajectories and disturbances. The controller needs to be designed with a sufficiently high bandwidth so that the low level torque control approximately behaves like a proportional gain for relevant reference variables. To get an idea of the relevant bandwidth, the amplitude spectra of ankle torque (reference) and ankle angle (perturbation) for walking at different walking speeds are examined.

Figure 5.1 shows the single-sided amplitude spectra of the normalized ankle torque and the ankle angle for level walking with different walking speeds (averaged data from [28]).

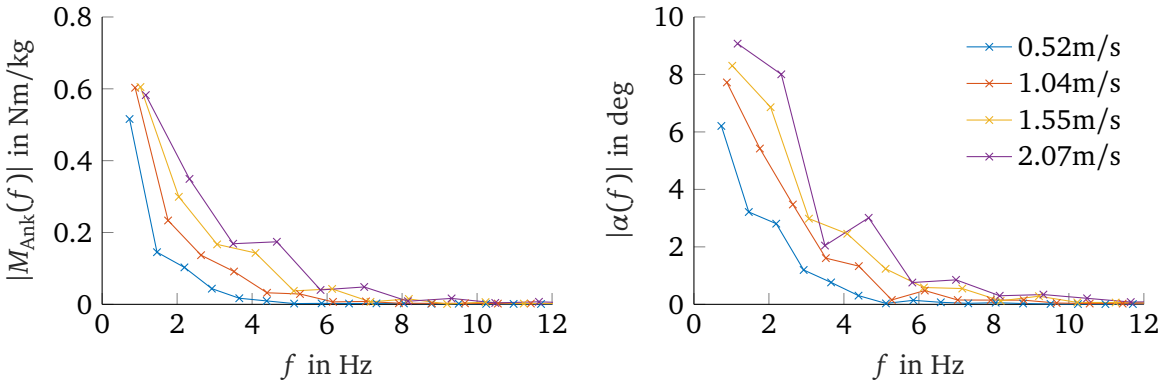

Figure 5.1.: Single-sided amplitude spectrum of ankle torque normalized to the body weight and ankle angle for level walking with different walking speeds. Joint trajectory data from [28]

At all walking speeds, especially the slower ones up to 1.5 m/s, the low frequencies are dominant and no relevant signal components above 5 Hz occur. Ankle trajectories from [28] and comparable data will be used as reference values in MLC to be designed. Furthermore, it can be assumed that disturbances, i.e. resulting joint angles during use of the prosthesis, have similar amplitude spectra to those presented here. A reasonable closed loop bandwidth for the closed loop torque control thus is in the range of

$$f_{\mathrm{b,des}} = 8 \ldots 10\,\mathrm{Hz} \quad \text{or} \quad \omega_{\mathrm{b,des}} = 50 \ldots 63\,\mathrm{rad\,s^{-1}} \,.$$

Compensation of the actuator dynamics in this frequency band is recommended. In addition, an integral component in the controller is necessary to compensate for model inaccuracies, e.g., due to the nonlinear kinematics of the ROA prosthetic foot or the nonlinear stiffness of the AG.

With regard to the measured variables, the following is valid: For both actuators, ROA and AG, the motor position φ_{M} and the output torque (ROA) respectively the output force (AG) is measured. In case of the ROA, the output torque M_{Ank} is determined from the measured ankle angle α and the motor position φ_{M} with the help of the nonlinear kinematic equations. For the AG, the output force F is directly measured with the force transducer.

Further, due to the high transmission ratio of the drive train, the measurement of the motor position φ_{M} has a much better signal-to-noise ratio than the measurement of the ankle angle α or the output force F_{AG}. Due to this, and due to the high sampling rate of 1 kHz, it can be assumed that the time derivative of the motor position $\dot{\varphi}_{\mathrm{M}}$, i.e. the angular speed $\dot{\varphi}_{\mathrm{M}}$, determined via backward differences is also available as a measured variable.

Model Transformation

The controller design will be carried out for the unified model presented in Section 4.4, of which the block diagram and model equations are reproduced here for the sake of readability. Further, the Δ indicating the linearized variables is omitted in the rest of the chapter for the sake of readability.

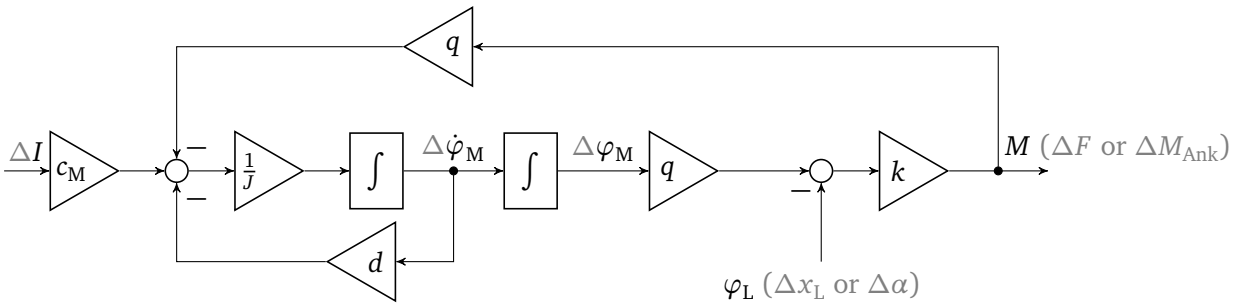

Figure 5.2.: SEA block diagram. The Δ indicating the linearized variables is omitted for the rest of this chapter.

To make use of the measured variables available in both actuators, the system equations

$$\begin{bmatrix} \dot{\varphi}_{\mathrm{M}} \\ \ddot{\varphi}_{\mathrm{M}} \end{bmatrix} = \begin{bmatrix} 0 & 1 \\ -\frac{q^2 k}{J} & -\frac{d}{J} \end{bmatrix} \begin{bmatrix} \varphi_{\mathrm{M}} \\ \dot{\varphi}_{\mathrm{M}} \end{bmatrix} + \begin{bmatrix} 0 \\ \frac{c_{\mathrm{M}}}{J} \end{bmatrix} I + \begin{bmatrix} 0 \\ \frac{qk}{J} \end{bmatrix} \varphi_{\mathrm{L}} \tag{5.1}$$

$$M = \begin{bmatrix} qk & 0 \end{bmatrix} \begin{bmatrix} \varphi_{\mathrm{M}} \\ \dot{\varphi}_{\mathrm{M}} \end{bmatrix} - k\varphi_{\mathrm{L}} \tag{5.2}$$

will be transformed such that the state vector contains the output torque M. Time derivation of M in the output equation (5.2) leads to

$$\dot{M} = qk\dot{\varphi}_{\mathrm{M}} - k\dot{\varphi}_{\mathrm{L}} \,. \tag{5.3}$$

The actuator equation of motion can be formulated as

$$\ddot{\varphi}_{\mathrm{M}} = \frac{1}{J}\left(c_{\mathrm{M}} I - d\,\dot{\varphi}_{\mathrm{M}} - qM\right) , \tag{5.4}$$

as can be seen from the state space model or the block diagram Figure 5.2. Equations (5.3) and (5.4) lead to the transformed state space representation

$$\begin{aligned}
\begin{bmatrix} \dot{M} \\ \ddot{\varphi}_{\mathrm{M}} \end{bmatrix} &= \underbrace{\begin{bmatrix} 0 & qk \\ -\frac{q}{J} & -\frac{d}{J} \end{bmatrix}}_{\boldsymbol{A}} \underbrace{\begin{bmatrix} M \\ \dot{\varphi}_{\mathrm{M}} \end{bmatrix}}_{\boldsymbol{x}} + \underbrace{\begin{bmatrix} 0 \\ \frac{c_{\mathrm{M}}}{J} \end{bmatrix}}_{\boldsymbol{b}} I + \begin{bmatrix} -k \\ 0 \end{bmatrix} \dot{\varphi}_{\mathrm{L}} , \\
M &= \underbrace{\begin{bmatrix} 1 & 0 \end{bmatrix}}_{\boldsymbol{c}^{\mathrm{T}}} \boldsymbol{x} ,
\end{aligned} \tag{5.5}$$

with the state vector $\boldsymbol{x}$, the system matrix $\boldsymbol{A}$, input vector $\boldsymbol{b}$ and output vector $\boldsymbol{c}^{\mathrm{T}}$. This state space representation allows the design of a controller that utilizes measured torque and motor velocity using state space methods.

5.1. Torque control of SEAs

For the control of both actuators, a model-based approach consisting of a model-based feedforward control and a feedback controller is used. The suggested control structure is based on [95] and shown in Figure 5.3. The model-based feedforward control consists of a controlled model of the plant and is designed to achieve good command action and disturbance rejection towards measurable disturbances. The feedback control is implemented as a PI-control with state feedback [96]. It handles modeling errors as well as unmeasured disturbances and guarantees zero tracking error at steady state. Both, feedforward and feedback control, can be designed independently from each other. The design will be described in the following sections.

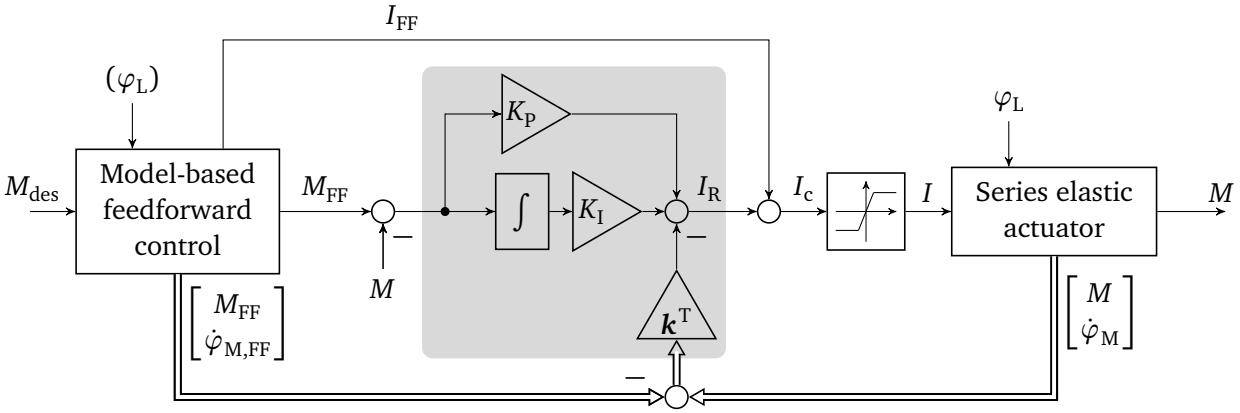

Figure 5.3.: Control structure with model-based feedforward control, PI-control with state feedback (grey area), current saturation and series elastic actuator. An integrator anti-windup is implemented, but not shown for reasons of simplicity. Parentheses at the load angle φ_L indicate, that φ_L is only fed into the feedforward control, if it is measurable.

5.1.1. Model-based feedforward control

The model-based feedforward control consists of a controlled actuator model. It can be seen as a prefilter, which generates a modified reference and a corresponding control input, that suit the closed loop dynamics of the feedforward model. The inputs of the model-based feedforward control are the desired torque M_{des} and, if available, the disturbance input φ_L. The outputs are the modified reference torque M_{FF} and the modified state vector $\boldsymbol{x}_{FF} = \left[M_{FF},\ \dot{\varphi}_{M,FF}\right]^T$ as well as the feedforward control input I_{FF}.

For the state space model (5.5) a linear state feedback controller with constant prefilter

$$I_{FF} = f\, M_{des} + \boldsymbol{k}_{FF}^T \boldsymbol{x}_{FF} \tag{5.6}$$

will lead to zero steady state error (as long as $\varphi_L = \text{const}$), good command action and disturbance rejection.

In general high torques are required and actuator saturation can occur during prosthesis operation. Therefore, instead of equation (5.6), the following control law

$$I_{FF} = \begin{cases} I_{FF,sat} & , f\, M_{des} + \boldsymbol{k}_{FF}^T \boldsymbol{x}_{FF} > I_{FF,sat} \\ -I_{FF,sat} & , f\, M_{des} + \boldsymbol{k}_{FF}^T \boldsymbol{x}_{FF} < -I_{FF,sat} \\ f\, M_{des} + \boldsymbol{k}_{FF}^T \boldsymbol{x}_{FF} & , \text{otherwise} \end{cases} \tag{5.7}$$

is used, where $I_{FF,sat}$ is the saturation current allocated to the feedforward control. It is chosen to be 75 % of the maximum current available.

State space representation (5.5) is used to design the state feedback $\boldsymbol{k}_{\mathrm{FF}}^{\mathrm{T}}$ from (5.6). During the design, the saturation is ignored. It can be designed either as a linear-quadratic regulator (LQR) with weight matrices $\boldsymbol{Q}$ and R for the states and the input, or via pole placement.

Then, using matrices from the transformed state space model (5.5), the stationary prefilter f is determined as

$$f = \frac{1}{-\boldsymbol{c}^{\mathrm{T}}\left(\boldsymbol{A} - \boldsymbol{b}\boldsymbol{k}_{\mathrm{FF}}^{\mathrm{T}}\right)^{-1}\boldsymbol{b}}\,, \tag{5.8}$$

such that the steady state error of the feedforward model is zero. The resulting controller is then implemented as stated in equation (5.7).

The implementation of the feedforward model with the transformed state space model (5.5) is not favorable, as it requires the time derivation of the measured disturbance φ_{L} as an input, which will induce noise into the feedforward control. Therefore, an alternative representation of the actuator model is chosen for the implementation of the feedforward model. Either, the untransformed model from equations (5.1) and (5.2) or the block diagram from Figure 5.2 is used. In either case, $\boldsymbol{x}_{\mathrm{FF}}$ needs to be constructed from the variables of the model. Figure 5.4 shows the implementation of the model-based feedforward control based on the block diagram of the model. The feedforward control and the actuator model are indicated by the gray boxes.

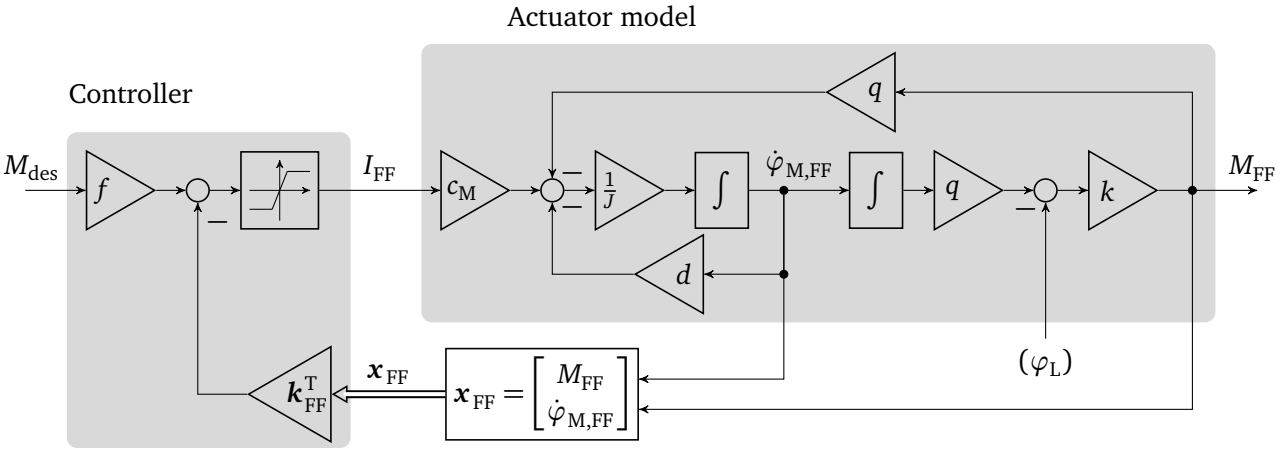

Figure 5.4.: Implementation of the model-based feedforward control with the block diagram of the actuator model. The grey boxes indicate the controller and the linear actuator model. The state vector $\boldsymbol{x}_{\mathrm{FF}}$, the feedforward current I_{FF} and the manipulated reference M_{FF} are annotated. The measured disturbance φ_{L} is fed into the actuator model, if available.

Note that the block diagram implementation easily allows to include nonlinear effects such as the coulomb friction or the nonlinear prosthesis kinematics, in which case the proposed controller does not ensure steady-state accuracy of M_{FF}. In this case, a controller with integral component or feedback linearization in the feedforward would be suitable. These approaches were not adopted and it was decided to address only the well identified actuator dynamics using the feedforward control, while unmodeled nonlinearities and model errors have to be compensated by the PI-control with state feedback.

For the ankle joint prosthesis, the disturbance φ_{L} is measurable. For the Bowden cable actuator, the disturbance x_{L} results from the knee and the ankle motion, where only the latter is measurable. Therefore, x_{L} is not feed into the feedforward control and has to be handled by the feedback controller.

5.1.2. PI-control with state feedback

Ignoring the model based feed forward control and the saturation block in Figure 5.3, the PI-control with state feedback is designed for the transformed state space model (5.5). Figure 5.5 shows the corresponding block diagram.

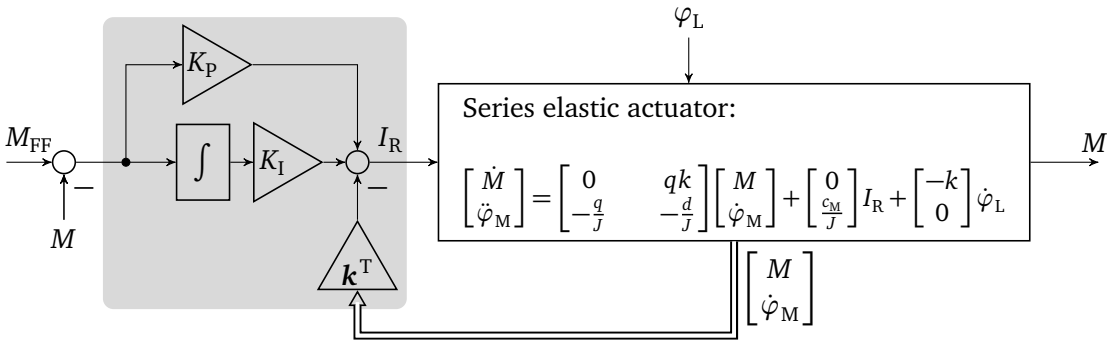

Figure 5.5.: PI-Control with state feedback and plant model for the controller design

The dynamics of PI-control with state feedback and series elastic actuator can be derived by adding the integrator state

$$\dot{x}_I = M_{FF} - M \tag{5.9}$$

and the control gains K_I, K_P and $\boldsymbol{k}^T$ to system (5.5) resulting in

$$\begin{bmatrix}\dot{M}\\ \ddot{\varphi}_M\\ \dot{x}_I\end{bmatrix} = \underbrace{\begin{bmatrix}0 & qk & 0\\ \frac{-q}{J} & \frac{-d}{J} & 0\\ -1 & 0 & 0\end{bmatrix}}_{\boldsymbol{A}_e}\underbrace{\begin{bmatrix}M\\ \dot{\varphi}_M\\ x_I\end{bmatrix}}_{\boldsymbol{x}_e} + \underbrace{\begin{bmatrix}0\\ \frac{c_M}{J}\\ 0\end{bmatrix}}_{\boldsymbol{b}_e} I_R + \underbrace{\begin{bmatrix}-k\\ 0\\ 0\end{bmatrix}}_{\boldsymbol{E}_{\dot{\varphi}_L}} \dot{\varphi}_L + \underbrace{\begin{bmatrix}0\\ 0\\ 1\end{bmatrix}}_{\boldsymbol{E}_M} M_{FF}\,, \tag{5.10}$$

$$I_R = -\underbrace{\begin{bmatrix}\boldsymbol{k}^T + [K_P\ \ 0], & -K_I\end{bmatrix}}_{\boldsymbol{k}_e^T}\boldsymbol{x}_e + K_P M_{FF}\,. \tag{5.11}$$

$$M = \underbrace{\begin{bmatrix}1 & 0 & 0\end{bmatrix}}_{\boldsymbol{c}_e^T}\boldsymbol{x}_e \tag{5.12}$$

Here, $\boldsymbol{x}_e$ denotes the extended state vector, and $\boldsymbol{A}_e$, $\boldsymbol{b}_e$ and $\boldsymbol{E}_M$ are the matrices of the extended state space model as indicated in (5.10). The extended state feedback $\boldsymbol{k}_e^T$ can again be designed using the LQR method for the system matrices $\boldsymbol{A}_e$ and $\boldsymbol{b}_e$ with weight matrices $\boldsymbol{Q}_e$ and R_e or via pole placement.

With $\boldsymbol{k}_e^T$ designed, the K_P and $\boldsymbol{k}^T$ are chosen to satisfy

$$\boldsymbol{k}_e^T = \begin{bmatrix}\boldsymbol{k}^T + [K_P\ 0], & -K_I\end{bmatrix}\,. \tag{5.13}$$

Since the equation is underdetermined, the choice of K_P is not obvious, and several options are investigated in [97]. One option suggested in [96] is to choose

$$K_P = \frac{-1}{\boldsymbol{c}^T\boldsymbol{A}^{-1}\boldsymbol{b}} \tag{5.14}$$

such that during the step response the control input I_R will immediately, i.e. at $t = 0$ take the steady state control input [97]. For the given system, the effect of the choice of K_P will be discussed in more detail in the following.

For the closed loop system (5.10) and feedback controller (5.11), the closed loop dynamics become

$$\dot{\boldsymbol{x}}_\mathrm{e} = \left(\boldsymbol{A}_\mathrm{e} - \boldsymbol{b}_\mathrm{e}\boldsymbol{k}_\mathrm{e}^\mathrm{T}\right)\boldsymbol{x}_\mathrm{e} + \boldsymbol{E}_{\dot{\varphi}_\mathrm{L}}\dot{\varphi}_\mathrm{L} + \left(\boldsymbol{E}_\mathrm{M} + \boldsymbol{b}_\mathrm{e}K_\mathrm{P}\right)M_\mathrm{FF} \tag{5.15}$$

and the closed loop torque transfer function is

$$G_\mathrm{M}(s) = \frac{M(s)}{M_\mathrm{FF}(s)} = \boldsymbol{c}_\mathrm{e}^\mathrm{T}\left(s\boldsymbol{I}_3 - \boldsymbol{A}_\mathrm{e} + \boldsymbol{b}_\mathrm{e}\boldsymbol{k}_\mathrm{e}^\mathrm{T}\right)^{-1}\left(\boldsymbol{b}_\mathrm{e}K_\mathrm{P} + \boldsymbol{E}_\mathrm{M}\right)\ , \tag{5.16}$$

where $\boldsymbol{I}_3$ is the (3×3)-identity matrix. For the given system, $G_\mathrm{M}(s)$ is a third order transfer function and its poles are determined by the extended state feedback $\boldsymbol{k}_\mathrm{e}^\mathrm{T}$. The choice of K_P and $\boldsymbol{k}^\mathrm{T}$ satisfying $\boldsymbol{k}_\mathrm{e}^\mathrm{T}$ in equation (5.13) only affects the numerator of $G_\mathrm{M}(s)$ and it can be shown that $G_\mathrm{M}(s)$ has the form

$$G_\mathrm{M}(s) = \frac{K_\mathrm{P}b_1 s + b_0}{(s-s_1)(s-s_2)(s-s_3)}, \tag{5.17}$$

where b_1 and b_0 are constants and s_i, $i \in [1,3]$ are the closed loop poles determined with $\boldsymbol{k}_\mathrm{e}^\mathrm{T}$. For $K_\mathrm{P} = 0$, the transfer function $G_\mathrm{M}(s)$ has no zeros, whereas for $K_\mathrm{P} > 0$, the transfer function $G_\mathrm{M}(s)$ has one zero in the left half s-plane, which tends to 0 as K_P increases.

Hence, the proportional gain K_P can be used to compensate a closed loop pole, and thus to increase the bandwidth without modifying the total controller gain $\boldsymbol{k}_\mathrm{e}^\mathrm{T}$. An example will be illustrated for the ROA in the next section, where the tuning of the PI-control with state feedback is described.

5.1.3. Controller tuning procedure

Feedforward control

For the tuning of model-based feedforward control the state space controller $\boldsymbol{k}^\mathrm{T}$ needs to be specified. Choosing the LQR design approach, $\boldsymbol{k}^\mathrm{T}$ is determined by specifying the weight matrices $\boldsymbol{Q}$ and R, where $\boldsymbol{Q}$ is chosen to be a diagonal matrix $\boldsymbol{Q} = \mathrm{diag}(q_{11}, q_{22})$. The element q_{11} is chosen high to lead to a desired bandwidth, whereas q_{22} is raised from zero to guarantee proper damping. The prefilter f is then designed according to (5.8).

PI-control with state feedback

To tune the feedback controller, $\boldsymbol{k}_\mathrm{e}^\mathrm{T}$ as well as K_P are to be specified. First, $\boldsymbol{k}_\mathrm{e}^\mathrm{T}$ is designed by specifying $\boldsymbol{Q}_\mathrm{e}$ and R_e. The Matrix $\boldsymbol{Q}_\mathrm{e}$ is chosen as a diagonal matrix $\boldsymbol{Q}_\mathrm{e} = \mathrm{diag}(q_{\mathrm{e},11}, q_{\mathrm{e},22}, q_{\mathrm{e},33})$, where the elements $q_{\mathrm{e},11}$ and/or $q_{\mathrm{e},33}$ are chosen high to lead to the desired bandwidth, whilst $q_{\mathrm{e},22}$ is used to adjust the damping.

With $\boldsymbol{k}_\mathrm{e}^\mathrm{T}$ specified, the proportional K_P is adjusted in the following way: starting from the K_P determined with (5.14), an adjustment factor $p_{K_\mathrm{P}} > 0$ is introduced to tune K_P as

$$K_\mathrm{P} = \frac{-p_{K_\mathrm{P}}}{\boldsymbol{c}^\mathrm{T}\boldsymbol{A}^{-1}\boldsymbol{b}}\ . \tag{5.18}$$

During the tuning, the factor p_{K_P} is gradually increased while observing the closed loop step response and Bode plot. This is done to increase the bandwidth (and equivalently decrease the settling time) while preventing overshoot, as will be seen in the following example.

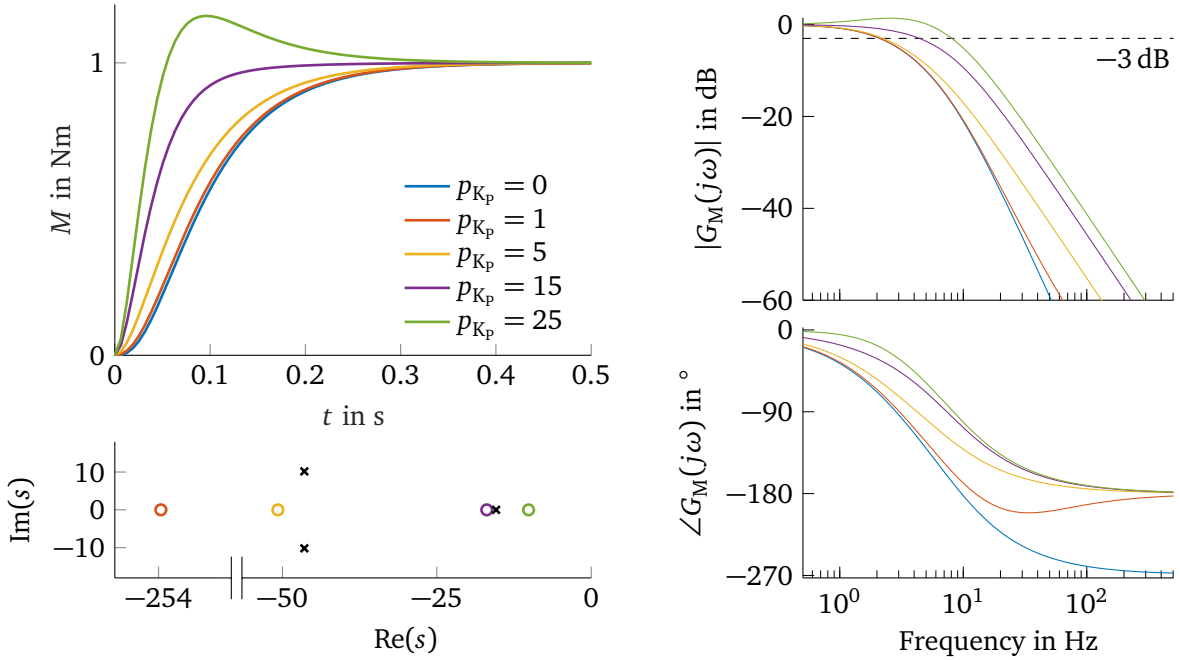

Figure 5.6.: Top left: Simulated closed loop step responses of the ROA SEA for K_P determined with varying p_{K_P}. Bottom left: corresponding pole zero maps of the closed loop transfer function (TF) (for $p_{K_P} = 0$ the TF has no zeros). Right plot: corresponding Bode plot of the closed loop TF, with the −3 dB threshold (dashed line) indicating the bandwidth

Example: Figure 5.6 demonstrates simulated closed loop step responses of the ROA prosthetic foot SEA with identical $\boldsymbol{k}_e^T$, but varying K_P. The extended controller gain $\boldsymbol{k}_e^T$ is designed with $\boldsymbol{Q}_e = \text{diag}(5, 10^{-3}, 10^3)$ and $R_e = 1$, resulting in closed loop poles at $s_1 = -15$ and $s_{2,3} = -46 \pm 10j$. Then the variation of K_P is investigated by adapting p_{K_P}. Next to the closed loop step responses, the resulting pole zero map and Bode plots of the closed loop transfer functions $G_M(s)$ are given.

For $p_{K_P} = 0$ the controller is reduced to a state feedback with integral action (e.g. [98]) and the resulting closed $G_M(s)$ has no zeros. Choosing K_P according to the recommendation in [96], i.e. $p_{K_P} = 1$ for the given system places the zero in the far left half s-plane with little impact on step response and bandwidth. A further increase of p_{K_P} moves the zero towards the dominant pole, reducing the settling time and increasing the bandwidth. When the zero is placed to the right of the dominant pole, overshoot occurs. Note that the damping of the complex-conjugate pair of poles is high, such that the resulting oscillation is not visible.

As can be seen, K_P allows to adjust the settling time and in consequence the closed loop bandwidth without modifying the total controller gain $\boldsymbol{k}_e^T$. Hence, the $\boldsymbol{k}_e^T$ and K_P can be designed one after the other, and the procedure can be iterated if necessary.

5.2. Resulting controllers

The controller of the AG Bowden cable actuator should be designed to not oscillate in order to prevent overshooting at forces close to 0 N, which would result in slack Bowden cable. However, the controller of the ROA SEA can be designed oscillating with a damping greater than $D > 0.9$ in order to achieve faster closed loop dynamics and better trajectory tracking.

5.2.1. ROA

Since the ROA SEA is fully composed of machine parts, the identified model from Chapter 4 is assumed to be accurate with little uncertainties. Due to this, and the fact that the disturbance input $\Delta\alpha$ is measured, a feedforward-control is used for the ROA SEA. The controller for the feedforward model is designed as an LQR controller with $\boldsymbol{Q} = \mathrm{diag}\left(12,\ 10^{-3}\right)$ and $R = 3/4$, and the prefilter is chosen according to (5.8), such that the bandwidth of the feedforward control is 8 Hz. The resulting controller is $\boldsymbol{k}^{\mathrm{T}} = [3.88,\ 0.0527]$ and $f = 4$ with the closed loop poles at $s_{1,2} = -60 \pm 27j$ ($D = 0.91$).

The PI-control with state feedback is designed with $\boldsymbol{Q}_{\mathrm{e}} = \mathrm{diag}\left(5,\ 10^{-3},\ 10^{3}\right)$, $R_{\mathrm{e}} = 1$ and $p_{\mathrm{K_P}} = 14$, resulting in the controller parameters $\boldsymbol{k}^{\mathrm{T}} = [1.5,\ 0.047]$, $K_{\mathrm{P}} = 1.7$, and $K_{\mathrm{I}} = 31$. The closed loop transfer function is

$$\frac{M(s)}{M_{\mathrm{FF}}(s)} = \frac{1920(s+18)}{(s+15)(s^2+93s+2260)}\,, \tag{5.19}$$

where the zero is used to compensate the dominant pole, as examined in Figure 5.6, and the remaining complex-conjugate pair of poles $s_{2,3} = -46 \pm 10j$ has a damping factor of $D = 0.9$ The closed loop bandwidth is 4 Hz. This is lower than the desired 8 Hz derived at the start of this chapter, but still sufficiently fast since in case of the ROA, the model-based feedforward control tuned at 8 Hz can react to the disturbance input $\Delta\alpha$.

5.2.2. AG

In comparison to the ROA SEA, the AG SEA has to be assumed to be less accurately modeled because, first, the output stiffness k depends on the human tissue properties of the specific user, and, second, the friction in the Bowden cable varies with the Bowden cable bending and the cable force. In addition to this, the load position is not measured. For this reason, no feedforward control is used for the AG, and instead the PI-control with state feedback is designed to achieve a closed loop bandwidth of 10 Hz.

For the design of the AG controller, the linearized stiffness is assumed to be $k_{\mathrm{AG}}(F_0) = 8000\,\mathrm{N/m}$, which corresponds to an output force of $F_0 = 100\,\mathrm{N}$ based on the identification results in Section 4.3.5.

Since the classical LQR controller design does not provide a way to force the closed-loop to be non-oscillating, the controller was designed using pole placement.

The closed loop poles were placed at $s_1 = -95$, $s_2 = -96$, and $s_3 = -97$, and $p_{\mathrm{K_P}} = 3.5$ to place the closed loop zero closely left of the closed loop poles. The resulting controller is $\boldsymbol{k}^{\mathrm{T}} = [0.23,\ 0.078]$, $K_{\mathrm{P}} = 0.12$, and $K_{\mathrm{I}} = 12$. and the closed loop transfer function is

$$\frac{F(s)}{F_{\mathrm{des}}(s)} = \frac{8730(s+101)}{(s+95)(s+96)(s+97)}\,. \tag{5.20}$$

Since stiffness k of the AG is not constant, the effect of altered k due to either changed cable force or material properties (i.e. changed user) is investigated. Figure 5.7 shows the simulated step responses of the AG with the designed controller, but varied output stiffness k in the range of 3000 to 15 000 N/m, as well as the corresponding closed loop poles and zeros. Note that the closed loop zero, indicated with the black circle, does not change with altered k.

For very low stiffness values, the system gets oscillatory and overshoots by up to 20 %, whilst for very high stiffness values, the closed loop step response changes only marginally.

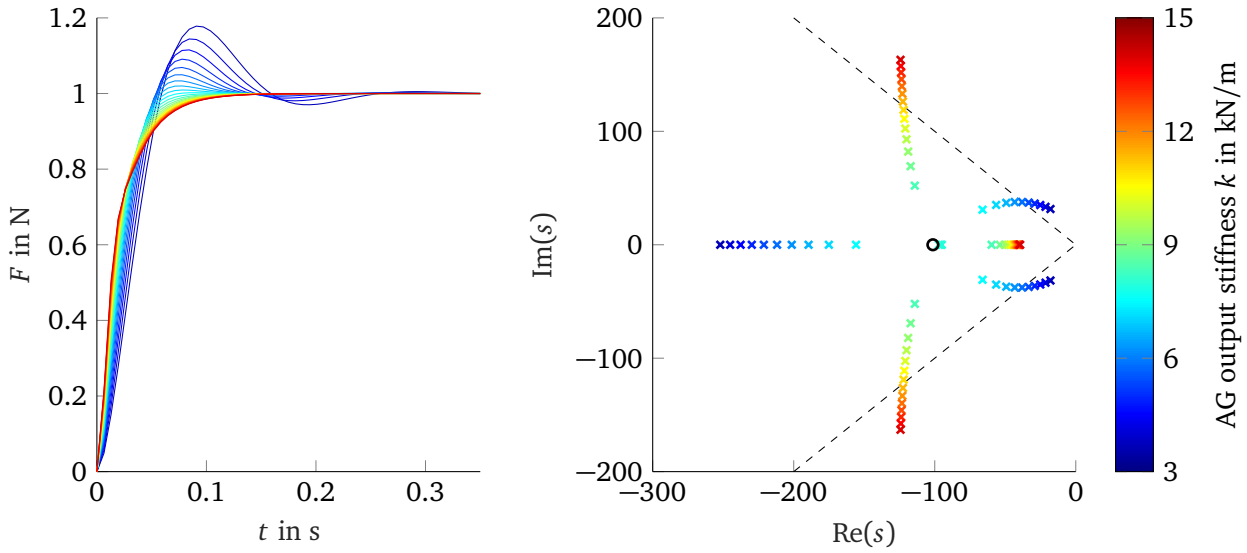

Figure 5.7.: Simulated closed loop step response of AG for range of stiffness values estimated in Chapter 4 (left) and corresponding closes loop poles (left). The dashed lines indicate a damping factor of $D = 0.7$

5.3. Controller modifications

With the controllers for the ROA and AG determined, two more aspects will be addressed in the remainder of this chapter. First, since the controllers contain integral action and the motor drive currents are limited, a suitable anti-windup is designed. Second, it has been disregarded so far that the Bowden cable can eventually become slack during prosthesis operation, for which the presented models are no longer valid. For this purpose, a heuristic approach will be implemented with the help of a fuzzy controller.

5.3.1. Anti-windup

For all controllers with integral component in this work, a classic linear feedback anti-windup (AW) algorithm for PID controllers [99, p. 248] is used as shown in Figure 5.8. Here u_I denotes the control signal of the integral component, $u - u_\mathrm{I}$ denotes the control signal of the remaining controller components, and u_r the control input realizable with the real actuator hardware, i.e. the saturated control input.

The linear feedback AW gain K_AW is designed with the method of the realizable reference, which is presented in [100] for the case of PID controllers. The realizable reference w_r is the reference signal, that, if it had been applied instead of the actual reference w, would have resulted in the realized control input u_r generated with w. When commanding w_r, the control input $u = u_\mathrm{r}$ equals the realizable control input, for which reason the saturation as well as the feedback K_AW in Figure 5.8 can be neglected, and the output y of the system would track the realizable reference w_r with the expected performance of the controller. [100]

In the following, the appropriate anti-windup gain K_AW is derived for the PI-control with state feedback without and with model-based-feedforward control. Therefore, the variables in Figure 5.8 are transformed into the Laplace domain, and in favor of readability the argument (s) is omitted.

PI-control with state feedback Let $[x_1, x_2]^\mathrm{T}$ be the state vector of the transformed SEA (5.1) and $\boldsymbol{k}^\mathrm{T} = [k_1, k_2]$ be the state feedback. For a realizable reference ($w = w_\mathrm{r}$, $u = u_\mathrm{r}$, $e = w_\mathrm{r} - y$), the control

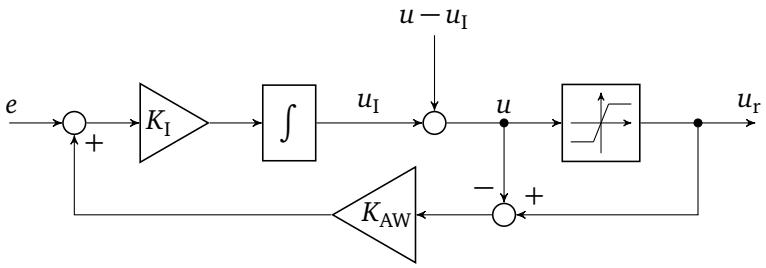

Figure 5.8.: Anti-windup: Only parts of the controller, that are relevant to the anti-windup, are shown. The remainder of the controller is indicated by $u-u_\mathrm{I}$.

input of the PI-control with state feedback presented in this work is

$$u_\mathrm{r} = \left(K_\mathrm{P} + \frac{K_\mathrm{I}}{s}\right)(w_\mathrm{r} - y) - k_1 x_1 - k_2 x_2 \tag{5.21}$$

where

$$u - u_\mathrm{I} = K_\mathrm{P} e - k_1 x_1 - k_2 x_2$$

is the control input from all components except for the integral part. In the specific case of the transformed state space model (5.1), the state vector contains the system output $[x_1,\, x_2]^\mathrm{T} = [y,\, x_2]^\mathrm{T}$, such that

$$u_\mathrm{r} = \left(K_\mathrm{P} + \frac{K_\mathrm{I}}{s}\right)(w_\mathrm{r} - y) - k_1 y - k_2 x_2 \,. \tag{5.22}$$

During a limitation of the control input (i.e. $u \neq u_\mathrm{r}$, $w \neq w_\mathrm{r}$) the control input is

$$u = \left(K_p + \frac{K_\mathrm{I}}{s}\right)(w - y) - k_1 y - k_2 x_2 + \frac{K_\mathrm{AW} K_\mathrm{I}}{s}(u_\mathrm{r} - u) \,. \tag{5.23}$$

Subtracting (5.23) from (5.22)

$$(u_\mathrm{r} - u) = \left(K_\mathrm{P} + \frac{K_\mathrm{I}}{s}\right)(w_\mathrm{r} - w) - \frac{K_\mathrm{AW} K_\mathrm{I}}{s}(u_\mathrm{r} - u)$$

and solving for the realizable reference w_r results in

$$w_\mathrm{r} = w + \underbrace{\frac{1 + \frac{K_\mathrm{AW} K_\mathrm{I}}{s}}{K_\mathrm{P} + \frac{K_\mathrm{I}}{s}}}_{G_w(s)} (u_\mathrm{r} - u) \,.$$

In order to achieve that $w_\mathrm{r} = w$ at the moment when the controller leaves the saturation $(u_\mathrm{r} - u) \to 0$, K_AW has to be designed such that $G_w(s)$ is a proportional gain [100]. Hence, the anti-windup gain is chosen as

$$K_\mathrm{AW} = \frac{1}{K_\mathrm{P}} \,. \tag{5.24}$$

PI-control with state feedback and model-based feedforward control For the sake of readability, let w continue to be the reference input of the PI-control with state feedback, i.e., the output of the model-based dynamic feedforward control. Then, in the present case the control input is

$$u = \left(K_\mathrm{P} + \frac{K_\mathrm{I}}{s}\right)(w - y) - \boldsymbol{k}^\mathrm{T}(\boldsymbol{x} - \boldsymbol{x}_\mathrm{FF}) + u_\mathrm{FF} \,, \tag{5.25}$$

where u_{FF} is the control input of the feedforward model. In the given case, the state vector of the feedforward control $\boldsymbol{x}_{\mathrm{FF}} = \left[w,\, x_{2,\mathrm{FF}}\right]^{\mathrm{T}}$ contains the reference w of the PI-control with state feedback.
Similar to the derivations without $\boldsymbol{x}_{\mathrm{FF}}$ and u_{FF}, the control input corresponding to the realizable reference is

$$u_{\mathrm{r}} = \left(K_{\mathrm{P}} + \frac{K_{\mathrm{I}}}{s}\right)(w_{\mathrm{r}} - y) - k_1\,(y - w_{\mathrm{r}}) - k_2\left(x_2 - x_{2,\mathrm{FF}}\right) + u_{\mathrm{FF}}$$

and the control input during saturation is

$$u = \left(K_{\mathrm{P}} + \frac{K_{\mathrm{I}}}{s}\right)(w - y) - k_1\,(y - w) - k_2\left(x_2 - x_{2,\mathrm{FF}}\right) + u_{\mathrm{FF}} + \frac{K_{\mathrm{AW}} K_{\mathrm{I}}}{s}\,(u_{\mathrm{r}} - u)$$

such that

$$(u_{\mathrm{r}} - u) = \left(K_{\mathrm{P}} + \frac{K_{\mathrm{I}}}{s}\right)(w_{\mathrm{r}} - w) - k_1\,(w - w_{\mathrm{r}}) - \frac{K_{\mathrm{AW}} K_{\mathrm{I}}}{s}\,(u_{\mathrm{r}} - u)\ .$$

Solving for the realizable reference results in

$$w_{\mathrm{r}} = w + \frac{1 + \frac{K_{\mathrm{AW}} K_{\mathrm{I}}}{s}}{K_{\mathrm{P}} + k_1 + \frac{K_{\mathrm{I}}}{s}}\,(u_{\mathrm{r}} - u)\ .$$

such that

$$K_{\mathrm{AW}} = \frac{1}{K_{\mathrm{P}} + k_1} \tag{5.26}$$

causes that reference and realizable reference are identical at the moment the limitation ends.

5.3.2. Fuzzy control for hybrid SEA

The fact that only pulling and no pushing forces can be applied with the Bowden cable actuator has been neglected so far. Strictly speaking, the AG is a system with hybrid dynamics. The assumption of an always tensioned inner cable is valid if the actuator is operated in the range of sufficiently large forces, the closed control loop overshoots little and and the load position changes slowly compared to the closed loop dynamics.

During the heel strike and in the swing phase, target forces close to 0 N and comparatively fast movements of the load position are to be expected. In this case, the inner cable may become slack and the motor and load may move detached from each other. In combination with the integral action of the controllers, unfavorable excitations at the load position may lead to bumps, oscillations and instability.

The possibility of actuator- or load-sided slack rope, uncertainties in orthotic attachment and tissue compliance, and the few available measurement variables complicate modeling of the process and do not provide explicit information about the location and length of the slack rope. From human intuition there is a simple strategy, which is to be applied in case of (imminent) slack rope:

- If the rope is slack or there is a risk of slack rope, the rope should be pulled, i.e. the actuator speed should be increased, while the force control should be suspended in this situation.

A suitable method for the implementation of this verbally easy to formulate mode of operation offers the implementation as a fuzzy system or fuzzy control [101]. In the present case, the force controller is extended by a fuzzy controller, which switches to current control mode when the rope forces are close to zero.

Inputs: The measured force F is used as the input variable. The range of forces is divided into low forces close to 0 N and high forces where a tensioned cable can be assumed. Ramp functions are used as the membership functions $\mu_{F,\mathrm{low}}$ for the low, and $\mu_{F,\mathrm{high}}$ for the high forces.

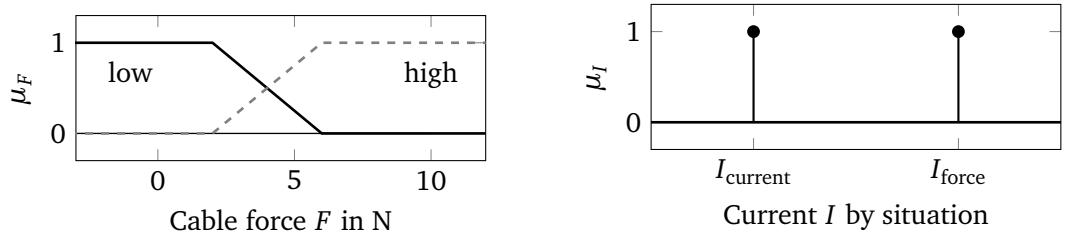

Figure 5.9.: Membership functions of the input and output variables

Outputs: The output variable is the actuator current I. Singletons are used for the membership function μ_I, with one value for the force controller current and one value for the actuator acceleration current.

The membership functions for input and output variable are shown in Figure 5.9. This results in the following rules:

1. If the force is low, then use the system input of the current control.
2. If the force is high, then use the system input of the force control.

For this simple fuzzy system the output quantity is calculated as

$$I = \frac{\mu_{F,\text{low}} I_{\text{current}} + \mu_{F,\text{high}} I_{\text{force}}}{\mu_{F,\text{low}} + \mu_{F,\text{high}}} = \mu_{F,\text{low}} I_{\text{current}} + \mu_{F,\text{high}} I_{\text{force}}$$

with $\mu_{F,\text{low}} + \mu_{F,\text{high}} = 1$ satisfied for all forces F.

Choice of actuator currents: The current to overcome actuator coulomb friction is about $I = M_\text{C}/c_\text{M} = 0.02/0.07 \approx 300\,\text{mA}$. For fast movements ($\dot{\varphi}_\text{M} \approx 300\,\text{rad/s}$), friction torques of about 40 mN m occur, corresponding to actuator currents of about 0.6 A. To reduce slack cable the current I_{current} should be selected large enough to overcome not only the actuator friction but also the friction in the untensioned Bowden cable.

Choice of force thresholds: The lower force threshold should be selected greater than $F_{\text{low}} > 2\,\text{N}$ to counteract zero point errors and measurement noise. The upper force threshold should be below the smallest nominal forces expected in operation (8 to 10 N) and above F_{low}.

Results: In pretests, currents of 1.0 to 1.5 A at thresholds of $F_{\text{low}} = 2 \ldots 3\,\text{N}$ and $F_{\text{high}} = 6 \ldots 8\,\text{N}$ have been shown to be suitable. For various force controllers (PI-control with state feedback, P-PI cascaded controller) and Bowden cable bending radii, these do prevent limit cycles or instability when applying arbitrary manual movement of the load position while commanding constant forces of 8 N to the force controller.

In addition to the proposed fuzzy controller, reference forces of the AG are restricted to forces $F_{\text{des}} \geq 8\,\text{N}$. If tracked with sufficiently small error, this ensures, that the inner cable is always tensioned. Furthermore, 8 N correspond to disturbance torques of $M = 0.64\,\text{N m}$ at the knee, which is negligibly small and not perceived as disturbing during free movement in pretests.

6. Biarticular prosthesis control for steady walking

In this chapter, the HLC and MLC that will be used to evaluate the biarticular prosthesis in the laboratory are designed. Therefore, first the requirements for controller are discussed and the resulting control structure is introduced. The design of the individual subsystems of the controller is described. Lastly, the performance of the developed hardware in combination with the controller consisting of the walking controller (HLC, MLC) as well as the previously derived LLC is evaluated during walking experiments.

Requirements

The goal is to evaluate the biarticular prosthesis during steady walking with varying distribution of power and torque between the monoarticular and the biarticular actuator. Hence, besides standing, the HLC and MLC to be designed should enable walking at a freely selectable but constant speed on the treadmill. During walking, ankle behavior similar to that of unimpaired individuals should be provided by the prosthetic ankle. Deviations from average unimpaired ankle behavior should be countered in a way that enables secure walking. The controller should allow freely adjustable distribution of ankle power and torque between the monoarticular and the biarticular actuator. In addition, the distribution to the individual actuators should be easily accessible for use in walking experiments.

6.1. Control structure

To meet these requirements, the hierarchical control structure shown in Figure 6.1 is developed: Gray blocks indicate the components of the walking controller, i.e. the HLC and MLC that enable walking with the prosthesis. The blue block contains those quantities manually provided to the controller. The white blocks indicate the user and the device as well as the previously developed LLC for the ROA and AG, which will be treated as ideal torque/force sources. The development and implementation of the walking controller is subject to the next sections.

6.1.1. Manual inputs

In general a high degree of automation facilitates the work in the laboratory experiments. Nonetheless, some parameters are not estimated, but entered manually in favor of simplicity, error-proneness and testing effort. The blue block contains the external inputs to the controller. As only standing and walking under laboratory conditions is required, the gait mode is manually changed by the subject or the experimenter using a handheld input device. Pretests showed, that this way the change of the gait mode can easily be enabled during the swing phase of the stride initiating walking, or the swing phase immediately before the end of walking. The walking velocity will only be adapted gradually in the experiments and will thus be adjusted by the experimenter through the realtime system interface. Both, gait mode and walking velocity could be estimated online with the help of methods provided in the literature, e.g. [102] for the walking speed, or [103] for the distinction of standing and walking. The proposed controller structure allows for this addition. Lastly, the distribution of power and torque among the individual actuators, i.e. ROA and AG, will either be specified manually by the experimenter, or be provided by the experimental protocol.

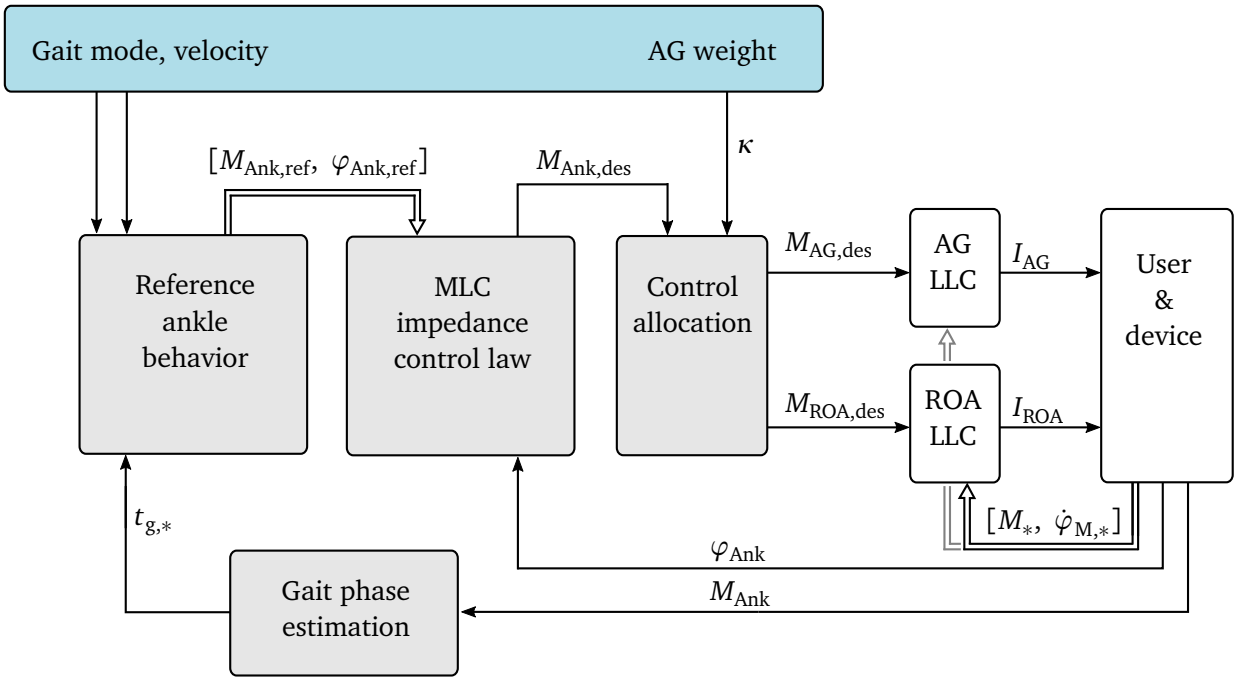

Figure 6.1.: Control structure for treadmill walking: Gray boxes indicate the high- and mid-level-controller enabling walking under laboratory conditions. The blue block contains manually set parameters, entered by a handheld device or the experimenter.

6.1.2. Walking controller subsystems

The gray blocks contain the subsystems of the HLC and MLC that enable walking on the treadmill. Since the prosthesis is evaluated at constant velocity, an event based gait phase estimation relying on the periodicity of the steady gait provides a suitable solution to determine the relative progress within the stride. Special attention is given to spatiotemporal asymmetries, which may occur in subjects with unilateral TTA, especially when using the unfamiliar powered prosthesis prototype. The gait phase is estimated separately for the stance and the swing phase to compensate for deviations of the duty factor from the reference behavior. With the estimated gait phase, ankle angle and ankle torque trajectories from unimpaired subjects are used as references in the MLC. They are further processed in an impedance type control law whose parameterization is motivated by human perturbation experiments. The resulting desired ankle torque is then allocated to the different actuators by selection of the AG weight factor κ. The design of the individual subsystems is presented in the sections that follow.

6.2. Gait phase estimation

The gait phase t_g is typically defined as a variable that is $t_g = 0$ at the start of the stride, $t_g = 1$ at the end of the stride and linearly increases in between. To estimate the gait phase in steady walking applications, usually a single repeatedly occurring event, most often the heel strike, is used in combination with the duration of previous strides (e.g. [30]) to extrapolate the gait phase t_g for the current stride. The estimation

accuracy is thus determined by the actual periodicity of the gait as well as the accuracy of the event detection. Since the gait phase is usually combined with pattern generators, additional deviations can occur due to changed timing of the individual subject compared to the reference data, e.g. a changed duty factor.

From an ankle joint perspective, level walking has two distinct phases: The first is the stance, in which the ankle torque takes large values while the ankle angle moves slowly. The second phase is the swing phase, in which the torque is approximately zero and the ankle moves quickly to provide foot clearance. These two distinct phases motivate an altered approach for the gait phase estimation: the stride is divided in the two phases, stance and swing, and the relative progression is estimated for each of the two phases individually. The stance gait phase $t_{\mathrm{g,st}}$ is $t_{\mathrm{g,st}} = 0$ at heel strike and linearly increase to $t_{\mathrm{g,st}} = 1$ at the toe-off, whilst the swing gait phase $t_{\mathrm{g,sw}}$ will increase from $t_{\mathrm{g,sw}} = 0$ to $t_{\mathrm{g,sw}} = 1$ during the swing phase, i.e. the period between toe-off and heel strike. As a consequence, MLC reference trajectories must be prepared so that they are available separately for the stance and swing phase. That way, the gait phase estimation can accommodate not only individual stride durations, but also individual duty factors, that do not match the duty factor in the MLC reference trajectories.

To determine stance and swing gait phase as described, heel strike and toe-off events have to be determined with the prosthesis.

6.2.1. Event detection

To determine the stance, foot switches in various locations of the shoe sole (i.g. [44], [104]) are found in the literature, but are limited by durability issues. Grimmer et al. [105] investigated how zero crossings of the shank angular velocity measured with IMUs correlate with heel strike and toe-off events. They found, there is an almost constant relation for the heel strike, but a velocity dependent relation for the toe-off for unimpaired subjects. For impaired subjects, especially when wearing new prosthetic hardware, shank angular velocity trajectories likely differ from those of unimpaired subjects, such that the results from [105] cannot be transferred without further investigation.

To overcome the above mentioned limitations, the event detection in the present work uses the prosthesis torque M_{Ank} to detect the stance phase. Based on the typical ankle torque trajectories (see Figure 2.3) the finite state machine in Figure 6.2 is used to determine the stance phase and to provide the trigger signals at heel strike (HS) and toe-off (TO). Stance is divided in the two states early stance and late stance, and the swing is divided into early swing and late swing. Early stance is entered when the ankle torque increases above a small threshold M_{On}. Late stance is entered when the torque rises above the threshold M_{CD} during the controlled dorsiflexion. The late stance state is necessary for strides with multiple zero crossings after the heel strike, possibly caused by a pronounced dorsiflexion torque after the heel strike. Early swing starts when the torque becomes negative at TO. Late swing is entered after a minimum swing duration T_{min} has passed. The early swing phase is necessary to prevent the prosthesis from falsely triggering the toe-off during fast ankle movements.

The thresholds M_{CD} and T_{min} are determined based on the biomechanical data from walking experiments with 21 unimpaired subjects from [28]. The torque threshold M_{CD} is selected as 25 N m, which is easily reached even for very light subjects. The minimum swing duration $T_{\mathrm{min}} = 250\,\mathrm{ms}$ is chosen to be below the smallest mean swing duration for walking with 0.5 m/s to 2.1 m/s, which is 350 ms.

The value of M_{On} depends on the noise level of the torque measurements, as well as the torque values occurring during ankle movement in the late swing. To reduce the influence of the noise, a moving average filter is applied, the influence of which on the event detection is discussed in the following paragraph.

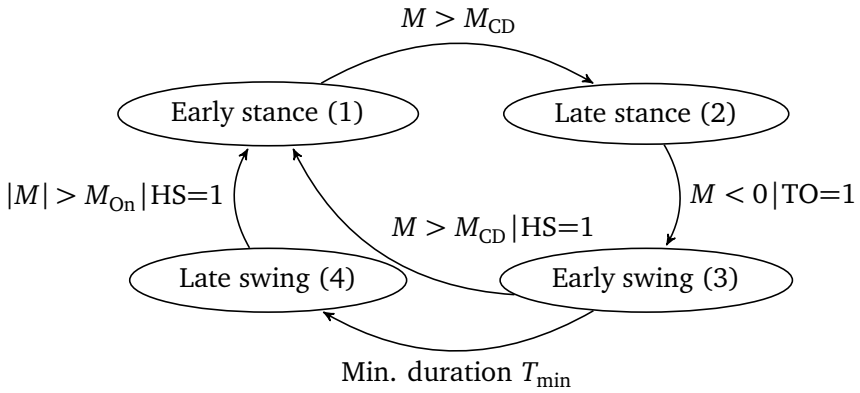

Figure 6.2.: Finite state machine for the detection of stance and swing based on the filtered ankle torque M

The influence of causal filters on the event detection Causal moving-average filtering of length N yields the following filtered torque at time t_i

$$M_i^* = \frac{1}{N}(M_i + M_{i-1} + ... + M_{i-N+1}) = \frac{1}{N}\sum_{n=0}^{N-1} M_{i-n} \,.$$

Assuming $M(t)$ to be a first order function at time t_i for the duration of the filter $t \in [t_{i+N+1}, t_i]$, i.e. $M(t) = a_0 + a_1 t$, the following holds for the filtered torque

$$\begin{aligned} M_i^* &= \frac{1}{N}\sum_{n=0}^{N-1}(a_0 + a_1 t_{i-n}) = a_0 + \frac{1}{N}\sum_{n=0}^{N-1} a_1(t_i - n\Delta T) = a_0 + \frac{a_1 N t_i}{N} + \frac{-a_1 \Delta T}{N}\sum_{n=0}^{N-1} n \\ &= a_0 + a_1 t_i + \frac{-a_1 \Delta T}{N}\frac{(N-1)N}{2} = a_0 + a_1\left(t_i - \frac{(N-1)\Delta T}{2}\right) = M\left(t_i - \frac{(N-1)\Delta T}{2}\right) , \end{aligned}$$

which corresponds to a delay of the torque M by $\frac{N-1}{2}$ samples. Filtering the prosthetic moment allows the transition conditions, especially the on-threshold M_{On} for the heel strike, to be chosen more tightly and the detected transition times to be backdated by $\frac{N-1}{2}$ samples. This is possible if N is chosen sufficiently small. When filtering over 25 ms (25 sampling points), the heel strike is detected about 12 ms too late, which corresponds to a delay of about one gait percent. In that case, during the first gait percent of the stance phase, no support adapted to the stance phase could be provided, while the remaining stance phase is not affected by the filter. It is expected that the first gait percent of the stance phase has no influence on the quality of support, since the ankle angle changes little during this period and the ankle torque is identical to the swing phase at about 0 N m.

The filter length is chosen to be $N = 10$ samples, corresponding to 10 ms of measurement. M_{On} is then determined to be $M_{On} = 4$ N m based on measurements conducted with an early prototype of the biarticular prosthesis in [93], where 440 strides with various levels of AG support were conducted. Table 6.1 sums up all parameters of the event detection.

6.2.2. Stance and swing gait phase calculation

Let $t_{TD,i}$ and $t_{TD,i-1}$ be the preceding touch down (TD) events, and $t_{TO,i}$ and $t_{TO,i-1}$ be the preceding toe-off (TO) events. Then a series of preceding events at the current time t is a sequence $(\dots t_{TD,i-1}, t_{TO,i-1}, t_{TD,i}, t_{TO,i})$ or $(\dots t_{TO,i-1}, t_{TD,i-1}, t_{TO,i}, t_{TD,i})$ as shown in Figure 6.3.

Table 6.1.: Event detection parameters

Parameter	Variable	Value
Heelstrike detection torque	M_{On}	4 N m
Controlled dorsiflexion detection torque	M_{CD}	25 N m
Minimum swing duration	T_{min}	250 ms
Moving average filter length	N	10 samples

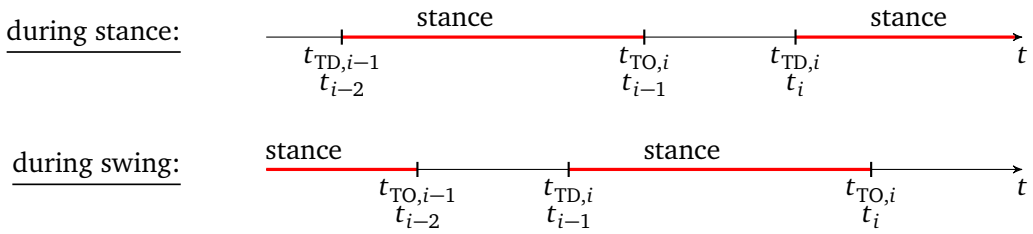

Figure 6.3.: Possible sequences of preceding stride events

Let also $(\dots t_{i-2}, t_{i-1}, t_i)$ be the series of preceding alternating TD and TO events, as indicated in Figure 6.3. Then, during a stance phase, the relative progression of the current stance $t_{\mathrm{g,st}}$ based on the duration of the previous stance $t_{\mathrm{TD},i} - t_{\mathrm{TO},i}$ is

$$t_{\mathrm{g,st}} = \frac{t - t_{\mathrm{TD},i}}{t_{\mathrm{TD},i} - t_{\mathrm{TO},i}} \qquad \left(= \frac{t - t_i}{t_{i-1} - t_{i-2}} \quad \text{during stance}\right).$$

Similar, during the swing phase, the relative progression of the current swing based on the duration of the previous swing $t_{\mathrm{TD},i} - t_{\mathrm{TO},i-1}$ is estimated as

$$t_{\mathrm{g,sw}} = \frac{t - t_{\mathrm{TO},i}}{t_{\mathrm{TD},i} - t_{\mathrm{TO},i-1}} \qquad \left(= \frac{t - t_i}{t_{i-1} - t_{i-2}} \quad \text{during swing}\right).$$

Thus, for the estimation of the stance-gait phase and for the estimation of the swing-gait phase, the identical expression follows in each case as

$$t_{\mathrm{g,st}} = \begin{cases} \frac{t-t_i}{t_{i-1}-t_{i-2}} & \text{, during stance} \\ 0 & \text{, during swing} \end{cases}$$
$$t_{\mathrm{g,sw}} = \begin{cases} 0 & \text{, during stance} \\ \frac{t-t_i}{t_{i-1}-t_{i-2}} & \text{, during swing} \end{cases}.$$

6.2.3. Adaptive averaging

For treadmill walking, an approximately constant stride rate is expected up to the level of inter-stride variability inherent in gait. By averaging the duration among multiple past steps, the gait phase estimate can become less sensitive to the inter-stride variability. Furthermore, the influence of outliers, e.g., due to misdetections or stumbling, can be reduced. In particular, the latter can be expected when testing novel, unfamiliar prostheses.

Besides moving averages, e.g. arithmetic or exponential averaging over N past steps, more robust estimators for the mean such as the median or truncated mean can be used. Schrade et al. [68] employ a

weighted moving average to determine the stride duration. For this purpose, the parameters of a normal distribution

$$\mu_\mathrm{T} = \frac{\sum_{i=1}^{N} T_i}{N}, \qquad \sigma_\mathrm{T} = \sqrt{\frac{\sum_{i=1}^{N} (T_i - \mu_\mathrm{T})^2}{N-1}} \tag{6.1}$$

are estimated from the past step durations T_i, $i \in [1,N]$ (or phase durations) and the stride duration is estimated as a weighted average according to

$$d_i = f(T_i|\mu_\mathrm{T}, \sigma_\mathrm{T}) = \frac{1}{\sigma_\mathrm{T}\sqrt{2\pi}} e^{\frac{-(T_i-\mu_\mathrm{T})^2}{2\sigma_\mathrm{T}^2}} \quad , \quad w_i = \frac{N \cdot d_i}{\sum_{i=1}^{N} d_i}$$

$$\bar{\mu}_\mathrm{T} = \frac{\sum_{i=1}^{N} (T_i \cdot w_i)}{N} \, ,$$

where $\bar{\mu}_\mathrm{T}$ is the estimated mean stride (or phase) duration. As a result, outliers are weighted small by the Gaussian distribution and their effect on phase duration estimate is suppressed to a greater extent than in the arithmetic mean.

Effect of the filter length Two measurements (2 subjects, 1 m/s, 350 strides each, $\kappa \in [0, 0.45]$), that were acquired with the control approach from [93], are used to investigate the effect of the filter length N for a simple moving average (SMA) and the Gaussian weighted moving average. For the evaluation, the mean absolute error (MAE) at the end of the stance and swing phase is calculated. The true value is assumed to be 1 or 100 %, respectively. Figure 6.4, left shows the MAE in dependence of the window length N. Since there are no irregularities in the measurements, SMA and Gaussian weighted differ only marginally. The effect of stumbling or irregular strides is emulated by delaying the HS detection in 10 % of the strides. To do this, M_On is increased to 50 N m, causing the HS of these strides to be detected approximately 250 ms to late. The resulting MAE are shown in Figure 6.4, right.

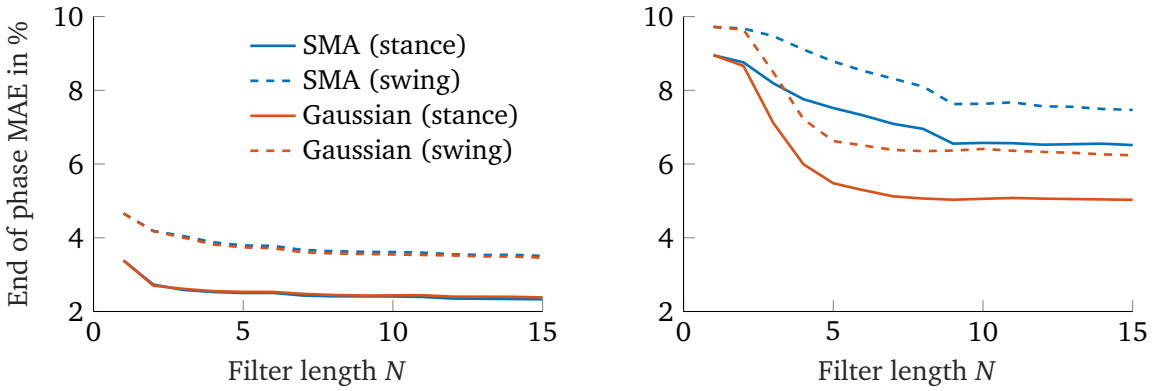

Figure 6.4.: Left plot: Mean average Error (MAE) of the gait phase estimation at the end of the stance and swing for simple moving average (SMA) and Gaussian weighted moving average. Right plot: MAE for the same approaches with faulty heel strike detection in 10 % of the strides emulating stumbling.

Unlike SMA, a Gaussian weighted moving average is capable to decrease the effect of irregular strides notably for $N > 3$. By averaging over several strides, a reduction of the MAE by 30 % (stance, data without irregular strides) can be achieved compared to $N = 1$. Above $N = 10$ there is no improvement of the MAE due to the variability inherent in the gait. Hence, for the remainder of the work,

- averaging with Gaussian weighting and $N = 6$

is used. Assuming HS and TO are estimated correctly, with the given gait phase estimation the MAE at the end of the stance phase during steady walking is 2.7 %. The average error during the whole stride is just half that value, i.e. 1.35 %. Based on a duty factor of 0.63, the error of the gait phase related to the entire step is on average less than one gait percent.

6.3. Reference torque generation

The reference torque for the actuators is generated in two stages: first, a desired torque for the ankle joint $M_{\text{Ank,des}}$ is determined based on the gait phase, the ankle angle and human reference torques $M_{\text{Ank,ref}}$ and angles $\varphi_{\text{Ank,ref}}$ with the help of a MLC impedance control law. In the second stage, the ankle reference torque $M_{\text{Ank,des}}$ is allocated to the AG and ROA actuators.

6.3.1. Reference ankle behavior

For the reference ankle behavior $M_{\text{Ank,ref}}$ and $\varphi_{\text{Ank,ref}}$, average ankle trajectories from [28] are used (21 subjects, 11 females, 10 males, 25.4 ± 2.7 yrs, 1.73 ± 0.09 m, 70.9 ± 11.7 kg). The data contains 5 walking velocities equally spaced between 0.52 and 2.59 m/s. Angle and torque trajectories are divided into stance and swing phases, with zero torque crossing used to cut the phases. To allow freely adjustable walking speeds, interpolation between the available walking speeds is performed using cubic splines. Figure 6.5 shows the resulting control surfaces with increasing range of motion and plantar flexion torque for the higher velocities.

When the sole of the ROA prosthetic foot is perpendicular to the prosthetic shank, the measured angle in Figure 4.1 is $\alpha = 131.4°$. Similar for the human reference angles from [28], the ankle angle $\varphi_{\text{Ank,ref}} = 115°$ at the instance the shank is perpendicular to the ground. Hence, an offset of 16.4°, which is fine adjusted by ±1° in consultation with the user, is utilized.

6.3.2. MLC impedance control law

Rather than switching between certain impedances as it is often found in the literature (see Chapter 2), the ankle impedance is parametrized in a continuous manner with the help of the estimated gait phase. The basic idea of the MLC introduced in this section is that if the ankle angle is similar to the human reference angle, the ankle will deliver a torque similar to the human. In case of deviation from the human reference angles, the torque should be adjusted appropriately. But how? In perturbation experiments Rouse et al. investigated how the human ankle joint is adjusted, if the ankle angle is perturbed during stance phase. They found that the deviations of the torque can be mostly described with the help of a linear stiffness, with stiffness values between 1.5 N m/(rad kg) to 6.5 N m/(rad kg). Similar results for the ankle are found in [106] where the joint behavior while stepping on unanticipated bumps was investigated. For the swing phase, [107], [108] found significantly lower stiffness values below 0.5 N m/(rad kg).

To emulate the described behavior, the MLC control law is used

$$M_{\text{Ank,des}}(t) = -k_{\text{Ank}} \left(\varphi_{\text{Ank}}(t) - \varphi_{\text{Ank,ref}}(t_{\text{g},*}) \right) + M_{\text{Ank,ref}}(t_{\text{g},*}) \tag{6.2}$$

is used, where $M_{\text{Ank,des}}$ is the ankle torque that is to be allocated to the actuators, $\varphi_{\text{Ank}}(t)$ is the measured ankle angle, and $\varphi_{\text{Ank,ref}}$ and $M_{\text{Ank,ref}}$ are the reference angle and torque trajectories from unimpaired

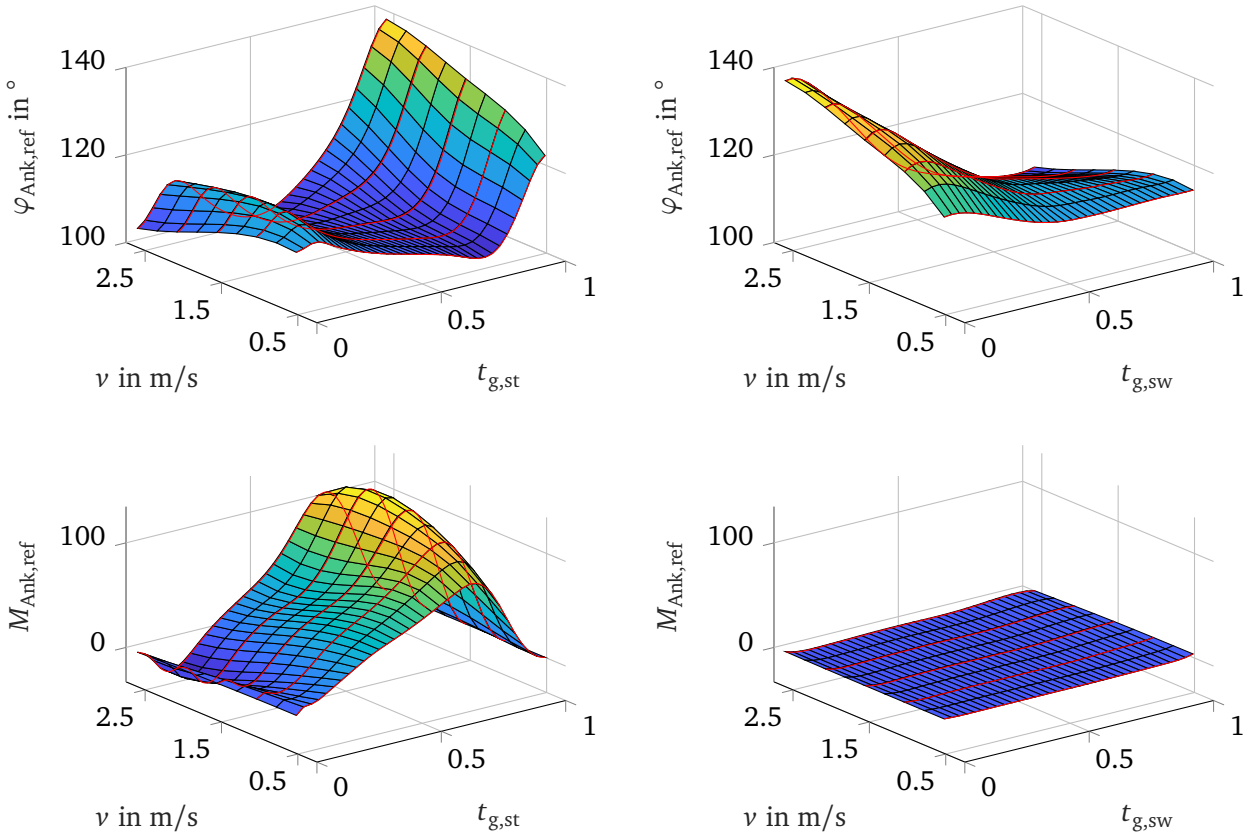

Figure 6.5.: Time normalized ankle angle and torque for the stance and swing for various walking speeds. Processed data from 21 subjects from [28]. De-normalized with $m_{\mathrm{User}} = 80\,\mathrm{kg}$. Red lines indicate the measured trajectories.

subjects. The gait phase $t_{g,*}$ can either be the stance or swing gait phase $t_{g,st}$ or $t_{g,sw}$. With the mass of the user m_{User}, the ankle stiffness is determined as

$$k_{Ank} = m_{User} \cdot k_{Ank,norm} \ ,$$

where is m_{User} is the body weight and $k_{Ank,norm}$ is the ankle stiffness normalized to the body weight. The latter is chosen to be $k_{Ank,norm} = 4\,\mathrm{N\,m/(rad\,kg)}$, which corresponds to the average value for the stance phase found in [109]. The ankle stiffness k_{Ank} serves two purposes: in the stance, it determines the ankle behavior when deviating from $\varphi_{Ank,ref}$, while in the swing, where $M_{Ank,ref} \approx 0\,\mathrm{N\,m}$, it causes the ankle angle to follow $\varphi_{Ank,ref}$.

6.3.3. Control allocation

The desired torque is allocated to the AG and the ROA actuator. Therefore, the AG weighting factor $\kappa \geq 0$ is introduced, which determines the relative portion of plantar flexion torque allocated to the AG. The desired force for the AG actuator is

$$M_{AG,des} = \kappa M_{Ank,des} H\left(M_{Ank,des}\right) \ , \tag{6.3}$$

where $H(*)$ is the Heaviside step function, which is 1 for positive arguments and zero otherwise. Since $\kappa \geq 0$, the Heaviside function ensures that $M_{AG,des} \geq 0 \forall M_{Ank,des}$. That way, only positive torques, corresponding to cable forces $F > 0$ are commanded to the AG. Since the AG actuator is designed as a force controller, the corresponding desired force is determined according to

$$F_{AG,des} = \frac{M_{AG,des}}{r_{Ank}} \ ,$$

where r_{Ank} is the ankle lever of the AG. The desired force is then further limited to forces above 8 N to prevent the cable from getting slack, as discussed in Section 5.3.2. The remainder of the desired ankle torque

$$\begin{aligned} M_{ROA,des} &= M_{Ank,des} - M_{AG,des} \\ &= (1-\kappa)\, M_{Ank,des} H\left(M_{Ank,des}\right) + M_{Ank,des} H\left(-M_{Ank,des}\right) \end{aligned}$$

is commanded to the ROA actuator. Here, the first term corresponds to the remaining plantar flexion torque, whereas the second term represents dorsiflexion parts of the desired torque.

6.4. Results

This section presents the results of the prosthesis controller, covering the reference generation, control allocation, gait phase estimation and LLC torque tracking performance. The focus is on the technical functionality, whilst the biomechanical evaluation is carried out in Chapter 7. Although the development and initial testing were performed with the bypass, measurements from the study with subjects with TTA presented in Chapter 7 are in this section to illustrate the controller results. For the exemplary demonstrations, measurement data of one test subject is used. The subject (male, 61 yrs, 74 kg, 1,75 m) walked at 1 m/s with the biarticular prosthesis for 30 min with the AG activity κ between 0 % and 45 %. For details on the experimental protocol, refer to Chapter 7.

6.4.1. Walking controller results

Figure 6.6 demonstrates the behavior of the walking controller for the AG being transparent ($\kappa = 0$) and providing 45 % of the ankle torque ($\kappa = 0.45$). Displayed is the prosthetic ankle angle as well as the contribution of the individual actuators to the prosthetic ankle torque. The gray dashed lines indicate the ankle reference torque $M_{\text{Ank,ref}}$ and angle $\varphi_{\text{Ank,ref}}$ generated with the help of the gait phase $t_{\text{g},*}$ and reference surfaces (Figure 6.5) and used in the MLC impedance control law (6.2). Black lines represent the overall desired torque (dashed) and actual torque (solid) at the ankle, while red and blue lines show the contributions allocated to the individual actuators. The actual ankle angle φ_{Ank} is the result of the overall prosthesis ankle torque M_{Ank} interacting with the user. The desired ankle torque $M_{\text{Ank,des}}$ results from the MLC impedance control law (6.2). For $\kappa = 0$, the desired ankle torque $M_{\text{Ank,des}}$ is identical with the desired torque of the ROA $M_{\text{ROA,des}}$ (red dashed).

The overall ankle torque and angle match a typical ankle behavior observed in unimpaired subjects. Both strides show pronounced controlled plantar flexion at the beginning of the stride, which is not present in the reference data but is quite common at higher speeds and individual subjects.

Transparent AG ($\kappa = 0$)

For $\kappa = 0$, the entire ankle torque is provided by the ROA, while the AG is transparent. There are only small differences between $\varphi_{\text{Ank,ref}}$ and φ_{Ank}, such that $M_{\text{Ank,des}}$ only slightly differs from $M_{\text{Ank,ref}}$. The negative reference torque $M_{\text{Ank,des}}$ during swing results from impedance MLC and, with the help of the ankle stiffness k_{Ank}, causes the ankle to perform the dorsiflexion and provide the foot clearance required during swing.

ROA torque tracking errors are small during the stance phase, and increase during the fast movement of the ankle angle and the swing phase. During the swing phase, the ankle torque M_{Ank} is approximately zero with the exception of the inertial forces. The AG is mostly passive with the exception of the quick ankle and knee movement after the push-off. The short peak in the AG torque at M_{AG} $t = 0.8$ s is observed in the opposite direction in the ROA torque M_{ROA}. As a result, the disturbances of both actuators at the ankle cancel each other, while the peak of the AG torque still impacts the unimpaired knee.

Powered AG ($\kappa = 0.45$)

In case of the powered AG, 45 % of the desired positive ankle torque is commanded to the AG, while the remaining 55 % is commanded to the ROA. The negative torque required during the initial controlled plantar flexion is fully provided by the ROA. For $\kappa = 0.45$, the ankle angle φ_{Ank} shows a stronger dorsiflexion during mid stance compared to $\kappa = 0$, which leads to increased desired ankle torque $M_{\text{Ank,des}}$ compared to $M_{\text{Ank,ref}}$. This increased dorsiflexion is also observed during the late push-off, resulting in an extend of the push-off torque towards the end of the stance.

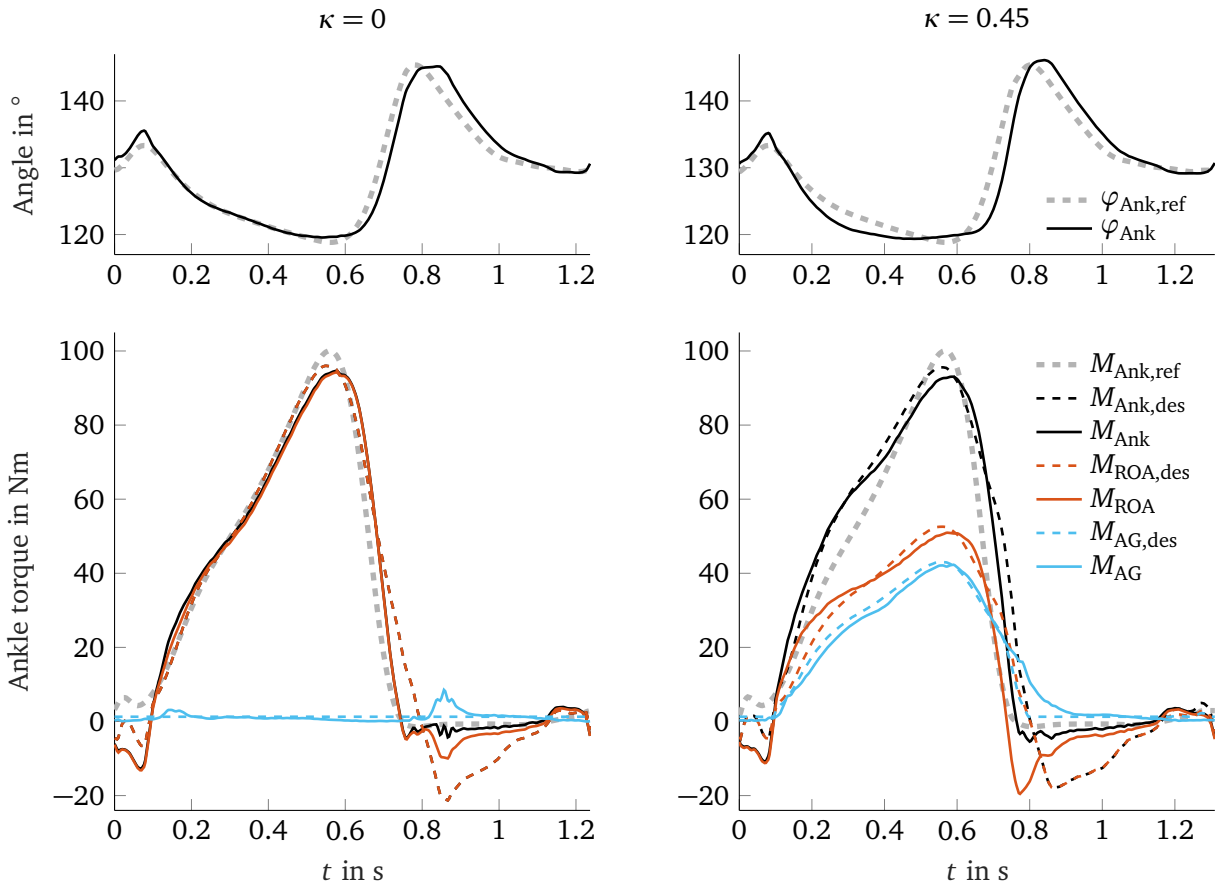

Figure 6.6.: Exemplary trajectories of one stride with passive AG (left, $\kappa = 0$) and active AG (right, $\kappa = 0.45$). Top plots show the prosthetic joint angle, while bottom plots show the overall prosthetic ankle torque as well as the contributions of the individual actuators, i.e. ROA and AG. Stride data from one subject with TTA walking at $1\,\mathrm{m/s}$.

Similar to the ROA, the AG tracks the desired torques with small errors during the stance and increased errors during the fast ankle and knee movement during and after the push off. Due to the increased AG torque during stance, the tracking error during the swing of both actuators has a different characteristic shape compared to $\kappa = 0$.

Duty factor adaption

For the shown strides, the duty factor is 0.60 for the transparent AG ($\kappa = 0$) and 0.58 for the powered AG ($\kappa = 0.45$). Both values differ from the duty factor of the reference data, which is 0.63. Without the separation into stance and swing phase, irregularities in the ankle references $M_{\mathrm{Ank,ref}}$ and $\varphi_{\mathrm{Ank,ref}}$ around the toe-off ($t \approx 0.75\,\mathrm{s}$) would occur, as was observed in [93]. Due to the separation into stance and swing phase, human ankle like references $M_{\mathrm{Ank,ref}}$ and $\varphi_{\mathrm{Ank,ref}}$ are generated. This demonstrates, that the separation of the gait phase estimation and reference generation into stance and swing phase allows to adapt to duty factors that deviate from the reference data.

Irregularly timed strides

Figure 6.7 shows an ill timed stride with a too short stance phase. The estimated stance gait phase at the end of the stance is $t_{g,st} = 94\,\%$, indicating that the stance phase is about 6 % shorter than in the preceding strides. In this case, the switching from the stance to the swing phase results in discontinuous reference angle $\varphi_{Ank,ref}$ and $M_{Ank,ref}$ in the MLC impedance control law (6.2) at $t \approx 0.73\,s$. From this, a short spike in the desired torques is observed, which due to its short duration and the limited bandwidth of the torque control loops does not result in torque trajectories significantly different from the regular strides shown in Figure 6.6.

Similar observations were made during irregular strides in early bypass-pretests, but were not perceived to be disruptive and therefore have not been dealt with any further. If these discontinuities were perceived as disturbing, they could be addressed with suitable filtering methods.

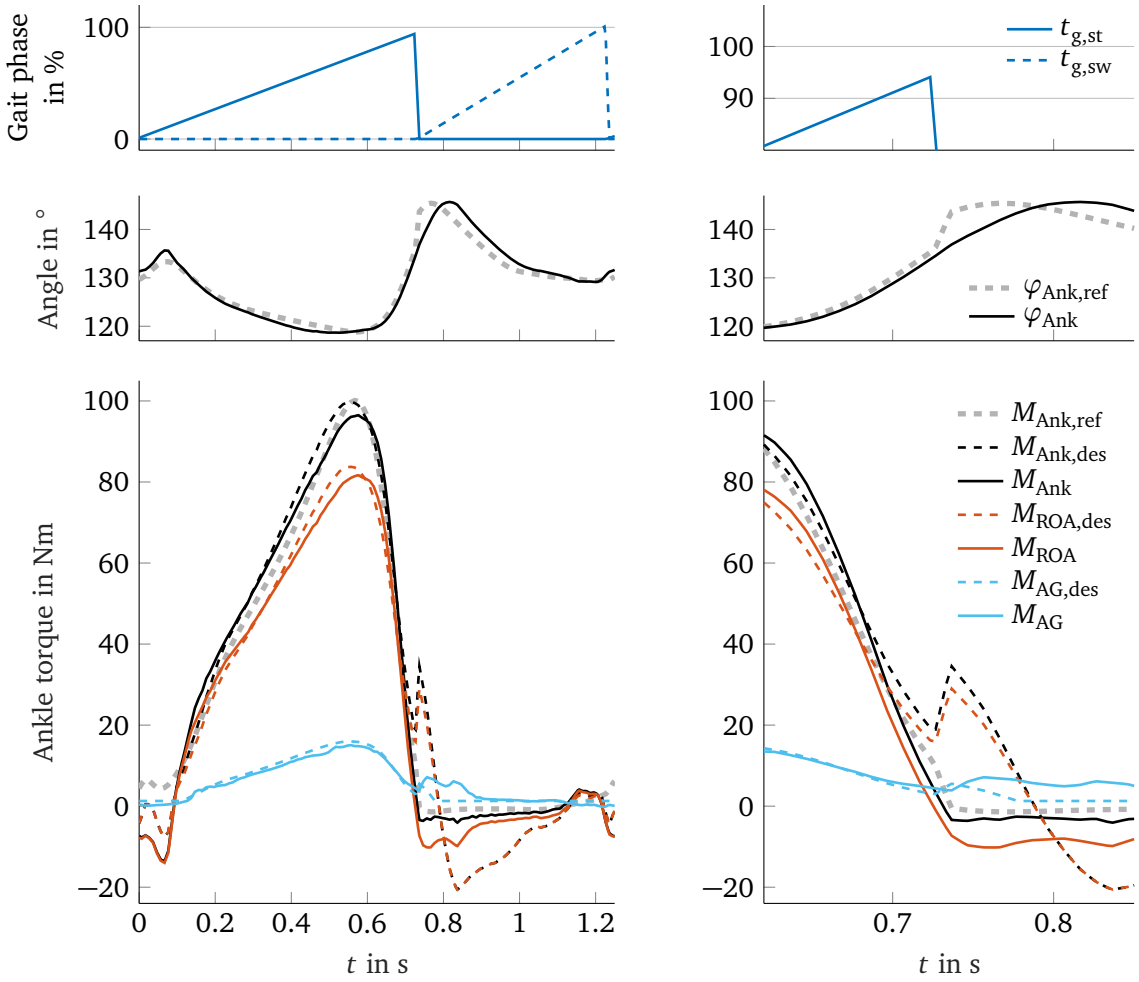

Figure 6.7.: Ill timed stride with to short stance phase (left column). Top plot shows the estimated stance and swing gait phase, central plot shows the joint angle, and bottom plots show the overall prosthetic ankle torque as well as the contributions of the individual actuators, i.e. ROA and AG. The right column shows the period of time around the toe-off, where the discontinuity in the reference trajectories occurs. Stride data from one subject with TTA walking at $1\,m/s$.

Gait phase estimation during disturbance

Figure 6.8 shows a sequence of nine strides, where the fourth stride represents an irregular stride caused by stumbling. The stumbling causes an irregular short stance phase and an oddly shaped ankle torque. The duration of the stance phase is approximately 20 % shorter than that of the preceding and following strides. The adaptive averaging method introduced in Section 6.2.3 suppresses this outlier such that the gait phase estimation of the following strides is unaffected.

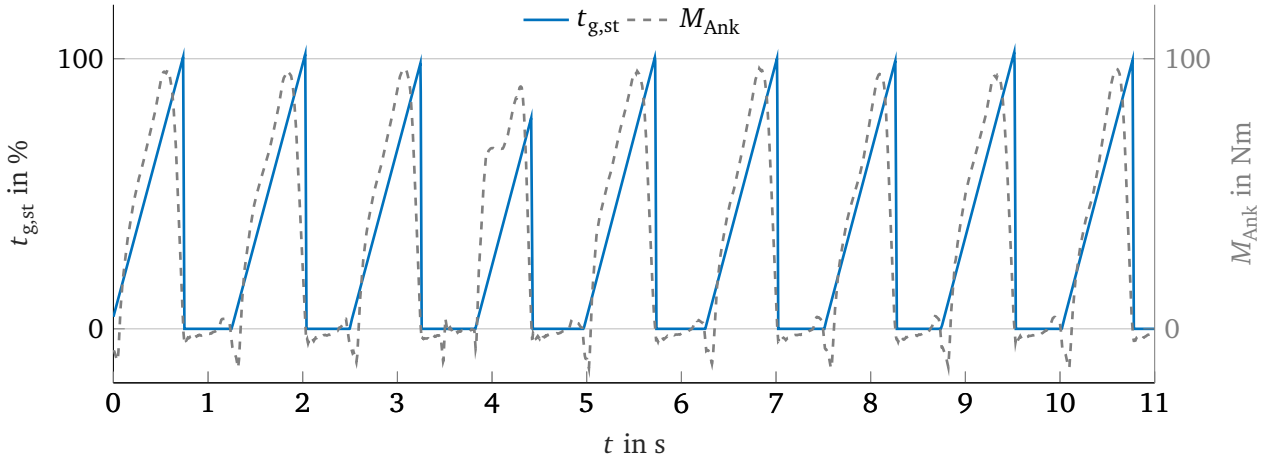

Figure 6.8.: Estimated stance gait phase (blue) for a walking sequence of nine strides with a stumbling event at the fourth stride. The overall ankle torque is indicated in gray dashed lines.

6.4.2. LLC results

Figure 6.9 shows the average torque tracking error within a stride of the ROA and AG for $\kappa = 0$ (165 strides) and $\kappa = 0.45$ (90 strides). Note, that for $\kappa = 0$ and $\kappa = 0.45$ the magnitude of the reference torques differs for both actuators: for $\kappa = 0$ the reference torques for the ROA are the highest, while for the AG the reference torque is 0 N m. In contrast, for $\kappa = 0.45$ the reference torques are of similar magnitude.

The ROA shows a low tracking error during the first 50 % of the gait cycle, which incorporate the controlled dorsi-flexion. In this period, the motor of the ROA-SEA moves little, while the series elasticity is beeing tensioned. During the push-off and the early swing phase, the torque tracking errors increase. In this phase, the motor actively pulls on the spring and then performs rapid movements, which result in increased inertial forces. For $\kappa = 0.45$, the torque tracking errors are slightly larger than for $\kappa = 0$. This is likely due to the stiffness series elasticity, which is optimized for average ankle trajectories observed for average weight subjects during level walking. Since for $\kappa = 0.45$ only 55 % of the ankle torque are provided by the ROA, this condition is similar to a very lightweight subject.

During the stance, the AG shows small tracking errors for both conditions of κ. For $\kappa = 0$, a small peak occurs in the early swing phase, while for $\kappa = 0.45$ a larger peak occurs earlier towards the end of the push-off. This increased peak is likely due to the increased AG torques for $\kappa = 0.45$. During the late swing, the tracking errors are close to zero, meaning that the knee and ankle movement is unaffected by the AG.

During early swing, where the reference torque of the AG is zero, the ankle torque tracking error of the AG is between 5 N m in passive mode ($\kappa = 0$) and 9 N m at high AG support ($\kappa = 0.45$). The corresponding disturbance torques at the knee are 2.5 N m and 4.5 N m, and the RMS errors during the swing are 2.25 N m and 3.8 N m. Both values can be considered low compared to the typical knee torque during level walking, which reaches maximum torque values of 35 N m [28] for the given walking speed and user mass.

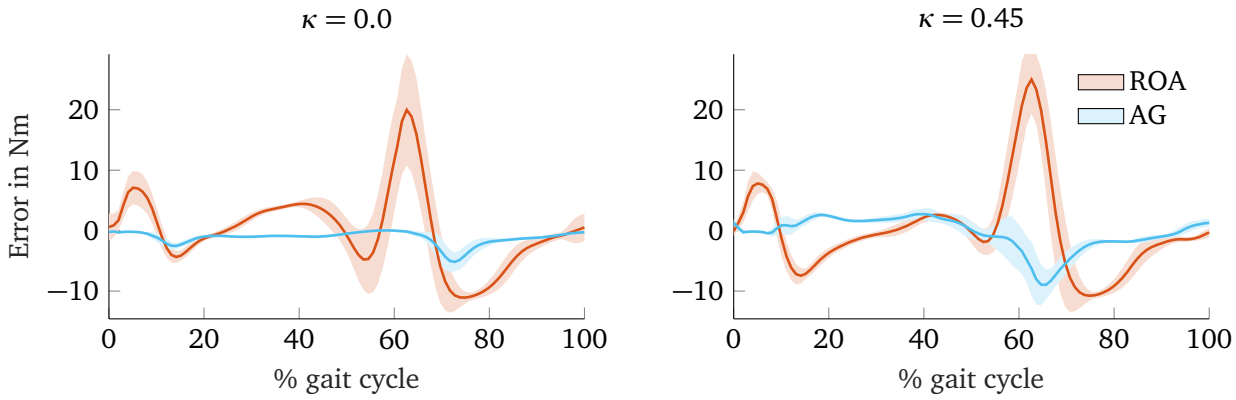

Figure 6.9.: Low level torque control tracking errors of the ROA and AG for passive AG (left) and powered AG (right). Solid lines represent the mean error, while the shaded area corresponds to one STD. Stride data from one subject with TTA from experiments in Chapter 7.

In general, the AG shows smaller tracking errors than the ROA. This is likely for three reasons. First, the portion of ankle torque allocated to the AG is smaller. Second, with 10 Hz the closed loop bandwidth of the AG torque controller is higher than for the ROA, which is 8 Hz. Lastly, the overall gear ratio of the AG is smaller, leading to a lower reflected inertia and smaller inertial forces during the fast movements.

Summary

In conclusion, a walking controller has been developed that generates human like ankle behavior with a variable distribution of plantar flexion torque between the monoarticular ROA and the biarticular AG. The controller can adapt to the user weight and the desired walking velocity. Outliers and irregular strides have no relevant effect on the walking behavior of the subsequent strides. Thus, all prerequisites for the use of the biarticular prosthesis in walking experiments on the treadmill are satisfied.

7. Biarticular prosthesis study

7.1. Introduction

The goal of the study is to investigate the effect of the biarticular prosthesis on the joint biomechanics as well as the energy expenditure during level walking. Compared to solely monoarticular ankle prostheses, the new prototype can couple ankle plantar flexion with knee flexion with the aid of the additional biarticular actuator.

It was hypothesized that shifting a certain amount of support from the monoarticular to the biarticular actuator can reduce inter-leg asymmetries compared to solely monoarticular actuation. It is further hypothesized, that this will reduce the energy expenditure of the human, as it will reduce the human knee and hip joint torque and power.

Throughout this chapter, the results are set into relation to the findings from two other studies evaluating powered prosthetic feet: The first study is the evaluation of the monoarticular BiOM powered prosthetic foot from Ferris et al. [10]. The second study is the evaluation of the biarticular prosthesis from Eilenberg et al. [44], that used the BiOM powered prosthesis with an additional powered knee orthosis. In both studies the average age is lower and the walking speed is higher than in this study.

7.2. Methods

A common approach in biomechanical experiments is the consecutive testing of several steady conditions. When energy expenditure measured by spiro-ergometric systems is involved, measurements can become time intensive. Selinger et al. [110] showed that the energy expenditure measured by spiro-ergometric systems can be approximated as a first order linear system with a time constant of 42 ± 12 s. Furthermore, the measurement is usually very noisy and requires time averaging for evaluation. Therefore, typically up to 6 min of measurement per condition are required, where the first 3 min are assumed to be transient behavior and the last 3 min are used for evaluating the condition. Approaches to reduce measurement time, e.g. by estimating steady state from the transient behavior [48] can halve measurement time at the expense of meaningfulness of results.

In the context of ankle exoskeletons, Malcom et al. [111] compared continuous sweep versus discrete step experimental protocols. They showed, that kinematic and kinetic parameters instantly respond to parameter changes in the assistive device, while changes in the energy expenditure are observed with the time lag from the spiro-ergometric system measurement dynamics.

Nonetheless, walking time in the experiment stays a critical factor, especially with subjects with gait related impairments. In this study, a continuous sweep protocol was chosen to cover the parameter space with fine resolution in the given walking time.

7.2.1. Experimental procedure

Upon arrival, the subjects were informed about the measurement systems used in the experiment and the motion capture markers were attached to them.

The location of the force plates underneath the belt of the treadmill was explained, and subjects were asked not to step over the marked centerline of the treadmill. The subjects were secured against falls with a harness attached to the ceiling. In case of uncertainty, the subjects could hold on to the railing of the treadmill. The subjects had time to familiarize themselves with the treadmill, including gait initiation and holding on to the railing.

The experimental procedure was as follows:

- **Own prosthesis walking experiment (E1):**
  The experiment consisted of 5 min of still standing followed by 10 min of walking at 1.1 m/s.

- **Powered prosthesis training:**
  The subjects were given time to familiarize with the powered prosthesis. First, the prosthesis was set to behave like a passive prosthesis with a stiffness of 4 N m/(rad kg). Then the behavior of the walking controller responding to rhythmic loading and unloading of the foot was demonstrated and explained. Subjects started walking with the powered prosthesis with $\kappa = 0$ (i.e. monoarticular actuation). The offset angle of the mid level control law was set in consultation with the test subject.

  When the subjects felt secure, the biarticular actuator was activated by continuously varying κ from 0 % to 45 % to 0 % within 2.5 min. This procedure was repeated at least twice.
  The overall training time for each subject was about 20 min, including about 10 min of walking.

- **Powered prosthesis walking experiment (E2):**
  The experiment consisted of 5 min of still standing followed by 30 min of walking at 1.0 m/s followed by 5 min of still standing.
  During the 30 min of walking, κ is modified as shown in Figure 7.1.

  For the first 8 min, κ is held at zero. This is done to counteract warm-up and initial learning effects. It is then steadily increased to the maximum value ($\kappa = 0.45$) within 9 min, held there for 2 min, and steadily reduced back to $\kappa = 0$ over 9 min. During the continuous sweep, the rate of change is $\dot{\kappa} = \frac{\pm 1\,\%}{12\,\mathrm{s}}$.

  Possible walking speeds for the powered prostheses were 1.0 m/s and 1.1 m/s. Out of these, the speed was set to 1 m/s in consultation with the first subject during warm-up. This speed was then used for all following subjects. Although effects of the different actuation would probably be more visible at higher speeds, the slower walking speed was chosen to ensure that all subjects could complete the experiment.

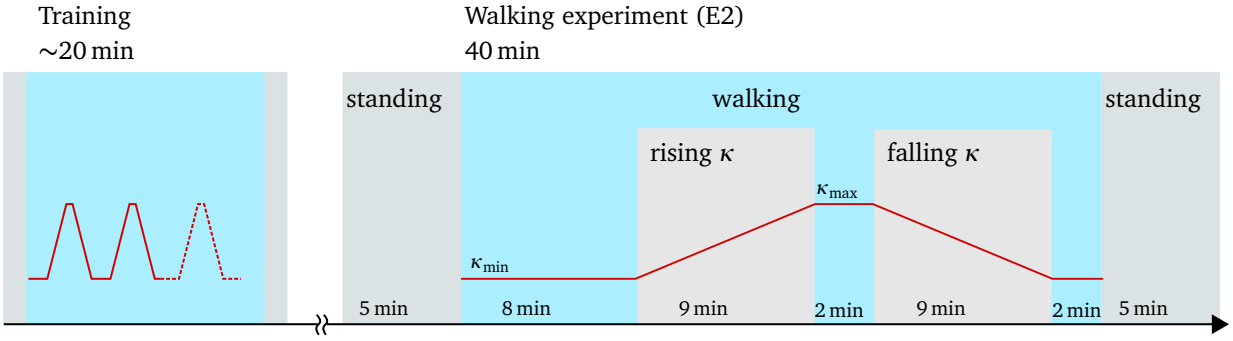

Figure 7.1.: Experimental protocol with the powered biarticular prosthesis

- **Powered prosthesis free walking (E3):**
  It was explained to the subjects that in the previous experiment the weighting of the biarticular actuator was varied, thus involvement of the knee varied. During this experiment, starting at 1.0 m/s the speed was subsequently raised in consultation with the subject with speed increments of $\Delta v = 0.5\,\mathrm{km/h}$ (0.14 m/s) and a maximum velocity of $v = 6\,\mathrm{km/h}$ (1.67 m/s). At each speed level, the subject could ask the experimenter to increase or decrease the support of the biarticular actuator. The biarticular support was changed by the experimenter in steps of $\Delta\kappa = 5\,\%$ and the preferred support of the subject was noted. If two adjacent support levels were pleasant, but not noticeably different to the subject, the spanned values of κ were noted. If explicitly asked for smaller adjustments, changes were adjusted to be $\Delta\kappa = 2.5\,\%$.

- **Feedback:**
  After the experiments, the subjects gave their feedback in a loose dialog with the experimenter, which lasted approximately 15 min.

During the walking experiments (E1 and E2), the subjects were asked to speak only about safety-related aspects. The experimenter announced when half of the experiment was over. He pointed out to the subject if there was continuous stepping over the center of the treadmill or if the subject was walking too far outside the force plates. During all experiments, the subjects wore their own sporty shoes.

7.2.2. Subjects

Three test subjects were selected with the help of a local medical supply store. The subjects were selected by an orthotist and had a high functional level (K3 or K4). Average subject characteristics are summarized in Table 7.1. A list of their passive ESR prostheses used in everyday life and to determine a reference during the experiments is given in Table 7.1.

One subject suffered paralysis of the full arm on the prosthetic side. During trials with its own prosthesis, this subject can swing the paralyzed arm freely. When wearing the powered prosthesis prototype, the paralyzed arm is tied to the abdomen - a situation with which the subject is familiar during sports activities such as jogging and cycling. With the exception of the unilateral transtibial amputation, the subjects had no other impairments affecting gait.

The study protocol was approved by the institutional review board of TU Darmstadt.

Table 7.1.: Subject characteristics (mean and standard deviation). The mass was recorded with shoes, prosthesis (own ESR resp. powered biarticular prototype), Cosmed K5, and the clothing worn during the experiment (short pants and shirt). The list of own ESR prostheses is given in random order.

Subject characteristics		Own ESR prostheses
N	3	Fillauer Allpro
age [yrs]	63 ± 8.2	Össur ProFlex Pivot
height [m]	1.82 ± 0.07	Össur Cheetah Xplore
mass ESR [kg]	79.5 ± 8	
mass powered prosthesis [kg]	81.9 ± 8	
amputation duration [yrs]	18.3 ± 11.4	
functional level	K3 or K4	

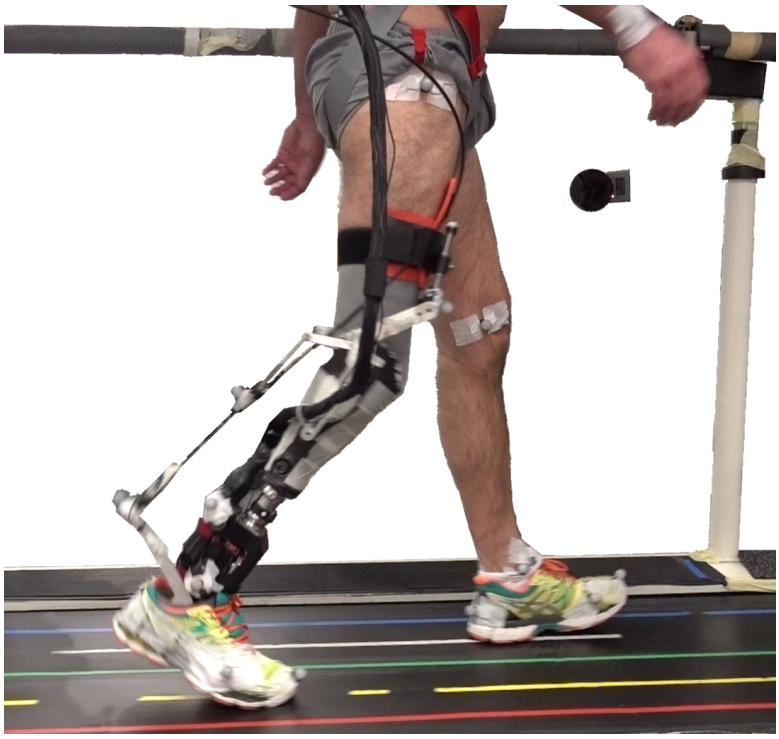

Figure 7.2.: Subject walking on instrumented treadmill with powered biarticular prosthesis. A motion capture camera, markers attached to the body, and the securing harness are shown. The Bowden cable actuator and the metabolic measurement system is not shown.

7.2.3. Data collection

The measurements were performed at the Locomotion Laboratory at TU Darmstadt. The human body motion was recorded at 300 Hz using 12 Oqus cameras (Qualisys, Sweden) and 30 19 mm super-spherical markers (Qualisys, Sweden). Markers were placed at anatomical landmarks and prosthesis parts as shown in Figure 7.3. A list of marker labels is given in the appendix Table B.1.

The walking experiment was performed on an instrumented treadmill (type ADAL-WR, HEF Tecmachine, France). Ground reaction forces were measured at 100 Hz. The vertical GRF were measured using two separate force plates directly underneath the belt of the treadmill. The anterior and lateral forces were measured using one single force plate underneath the above mentioned two. To decompose the anterior GRF during double support phase (DS), the adaptive transition function approach from [112] was used. In this approach, the anterior GRF of the trailing limb is estimated based on the duration of DS, the horizontal GRF measured before DS, and the vertical GRF measured during DS, such that GRF smoothly transitions towards zero.

The prosthesis data was logged at 100 Hz. A metabolic system (K5, COSMED S.r.l., Rome, Italy) was used to measure the gas exchange at 0.1 Hz with a mixing chamber technique.

7.2.4. Data processing

Kinematic motion data The markers were labeled and tracked in Qualisys QTM Track Manager (Qualisys, Sweden). Gaps of up to 50 ms resulting from temporarily covered reflective markers were gap-filled using polynomial gap filling in QTM Track Manager. The data was then exported and further processed in Matlab.

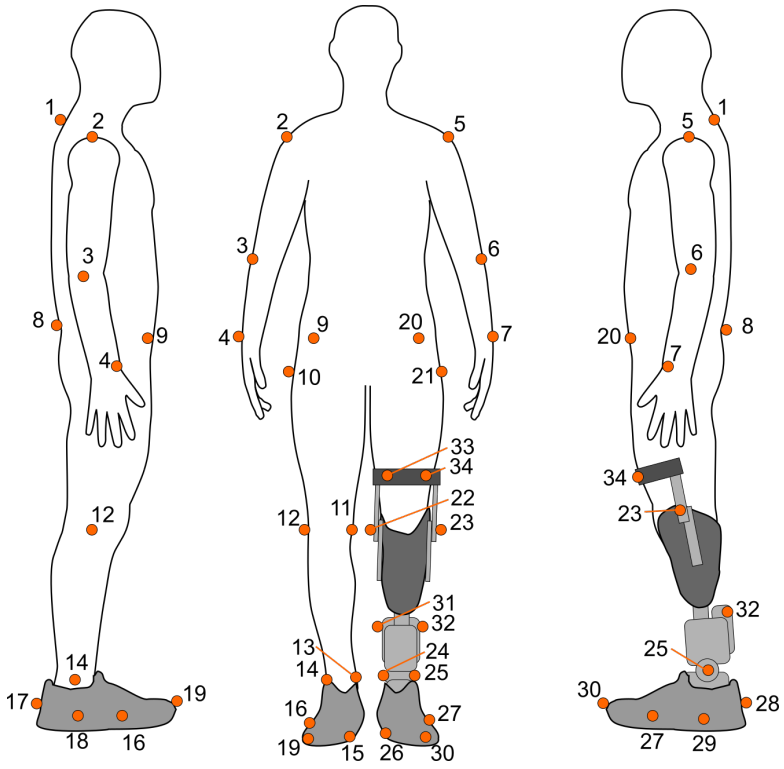

Figure 7.3.: Markers used in the prosthesis study. The marker labels are listed in Table B.1

During the experiments, for one subject, two medial markers (knee, ankle) on the prosthesis side were detached as a result of collisions with the ipso lateral leg. The medial ankle marker could be reconstructed from the corresponding lateral ankle marker and markers at the prosthesis (markers 31 and 32). The medial knee marker could be reconstructed from the corresponding lateral knee marker and the markers at the orthotic thigh bracket (markers 33 and 34).

Synchronization The GRF data and the prosthesis data were both resampled to match the sampling frequency of the motion capture data. Since the measurements were recorded on systems with individual clocks, they exhibit a time delay and drift due to the inaccuracies of the installed quartz cells. Therefore, all measurements were synchronized to the motion capture data in post processing.
To synchronize the force measurement, a pretest using exactly the same prerequisites (duration, sampling frequencies) as the in final study was performed. A stick marked with a marker was repeatedly dropped onto the force plate of the treadmill. Time delay and drift was then estimated by matching the measured forces to the vertical acceleration of the stick calculated from the motion capture system. To synchronize the prosthesis measurements to the motion capture data, the shank angular velocity measured at the prosthesis was correlated with the shank angular velocity calculated from motion capture data.
The metabolic measurements are synchronized by manually noting the system clock at the start and the end of the walking session.

Ground reaction forces The piezoelectric force transducers showed extensive drift over the duration of the experiment. Offset and drift of the horizontal and the vertical force measurements was first compensated by fitting piecewise linear polynomials to the unloaded phases at the start of the experiment, the start and the end of walking, as well as the end of the experiment.

Despite this compensation, individual vertical force sensors showed further drift over unloaded phases of the walking experiment (e.g. the swing phases of the leg). Assuming, that the vertical GRF should be approximately zero during swing phase, the vertical GRF were further corrected. This was done by subtracting a smoothed interpolation of the minimal forces observed during the swing phases.

Kinematics In the post processing, marker data and GRFs were filtered using the zero-phase digital filtering functionality provided in MATLAB . The filters are designed as second order Butterworth filters with a cut-off frequency of 10 Hz. In contrast to many other works, identical cut-off frequencies were used for movement and force data, as supposed in [113].

Foot tip, ankle and knee joint centers are determined as the midpoint between the corresponding medial and lateral joint markers [114]. Hip joint centers were determined using the GT-method [115]. Joint angles (ankle, knee, hip) are defined as the inner joint angles. For inter subject comparison, resting angles measured during standing are subtracted from the inner joint angles. The Sacrum marker was used to define the upper body segment, as throughout all subjects it was the least obscured marker out of a list of possible candidates.

Inverse dynamic analysis To estimate the sagittal plane joint torques of ankle, knee, and hip, the planar link segment model for each leg was solved. As weight and dimensions of the prosthesis are comparable to the part of the leg lost by amputation, anthropometric parameters from [20] are used for both the impaired and unimpaired leg. The center of mass accelerations are determined by numerical differentiation of the center of mass positions using second order central differences. The center of pressure (COP) is estimated from the GRF measurements. The estimated COP is then further limited to the dimensions of the foot (determined with the help of the heel and tip marker) to compensate errors when vertical GRF tend toward zero.

Periods in which the compensated, unfiltered vertical GRF exceed 20 N are classified as a stance phase. Irregular short phases resulting from artifacts, noise, or crossing of the treadmill center line are sorted out. The start of a stance phase is defined as touchdown, and the end is defined as toe-off.
The first 300 strides (corresponding to approximately 5 min of walking) and the last 30 strides of the experiment are excluded from the analysis. Strides during which the subjects hold onto the handrail or step over the treadmill centerline are excluded from further analysis. Periods where the foot crosses the centerline are determined by manually observing the vertical ground reaction forces, the stride durations, and the duty factor. Periods where the subject holds onto the treadmill handrail are determined from the wrist marker location. That way, 88 out of 1009, 95 out of 1145, and 18 out of 1257 strides are sorted out for the three subjects. Single strides are cut between two preceding touch downs, and normalized in time, i.e. interpolated to 100 sample points per stride.

Metabolic measurements To estimate the energy expenditure from the measured VO2 and VCO2, the formula derived in [116] is used, whereby the nitrogen term (nitrogen excreted in the urine) is neglected, as described in Section B.6. The net metabolic rate is calculated by subtracting the mean metabolic rate measured during the initial 5 min of still standing. To reduce the noise, a moving average filter over 6 samples, that is 60 s of measurement, is applied. From this follows that specific values of the energy expenditure in the evaluation will correspond to a range of ±2.5 % for the assigned values of κ.

The step response of a first order linear system is fitted to the start and the end of the walking experiment to estimate the metabolic time constants τ of the individual subjects (see Figure B.6 in the appendix). The subjects show faster time constants τ (27 ± 11 s) when the energetic cost increases, i.e. the walking session starts, and slower time constants (61 ± 6 s) when the energetic cost decreases, i.e. when the walking ends. The individual subject averaged time constants $\bar{\tau}$, when averaging for increasing and decreasing condition,

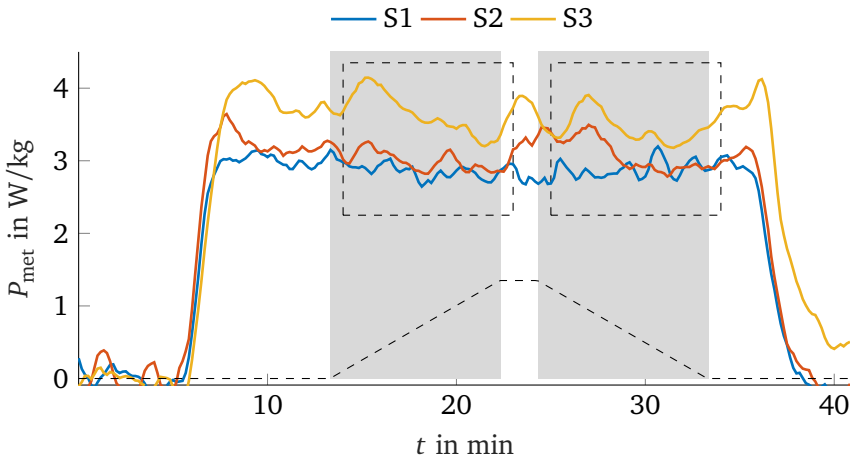

Figure 7.4.: Net metabolic rate of the subjects normalized to the body mass. The dashed line indicates the assistance profile. Gray boxes indicate the periods of rising and falling κ. The dashed boxes highlight the time periods of metabolic rate measurements associated with the periods of rising and falling κ.

were $\bar{\tau} = 39.5\,\text{s}$, $\bar{\tau} = 38.5\,\text{s}$, and $\bar{\tau} = 52.5\,\text{s}$, respectively. These time constants were used to assign the measured metabolic cost to a certain value of κ in the experiment E2, by assuming that the measured metabolic cost follows the actual metabolic cost with a delay of approximately $\bar{\tau}$.

Figure 7.4 illustrates the time windows associated with the periods of rising and falling κ.

7.2.5. Evaluation

Gait data with the subjects own prosthesis, comparison between impaired and non-impaired leg, and comparison with a control group of non-impaired subjects are used for evaluation. For the control group, data from [28] is used. The walking speed is slightly faster and the age is significantly lower than for the group of subjects in this work. Table 7.2 lists the control group characteristics. It is worth noting that for constant walking velocity, stride length and stride duration are synonymous.

Table 7.2.: Control group parameters [28]

N	age [yrs]	height [m]	mass [kg]	walking speed [m/s]
21 (11 male, 10 female)	25.4 ± 2.7	1.73 ± 0.09	70.9 ± 11.7	1.05

Time normalized joint trajectories (angle, torque, power) are averaged for values of κ in either $0 \pm 2.5\,\%$, $22.5 \pm 2.5\,\%$, or $45 \pm 2.5\,\%$, and compared to the references. Spatio temporal parameters are evaluated for $\kappa \in [0,\, 5\,\%]$, [5%, 10%] ... [40%, 45%] The spatio temporal parameters evaluated in this work are estimated as defined in Table 7.3.

Table 7.3.: List of gait parameters and belonging definitions used in this work

Gait parameter	Definition
Spatial parameters	
Stride length	Anterior-posterior distance between two consecutive footprints of the same foot, determined by the anterior-posterior distance of the associated heel marker at 0 and 100 % GC
Step length	Anterior-posterior distance between ipso-lateral heel and heel of the leg under consideration, determined during the heel strike of the leg under consideration strike
Step width	Lateral distance between ipso-lateral heel and heel of the leg under consideration, determined during the heel strike of the leg under consideration
Temporal parameters	
Stride duration	Time elapsed between two consecutive heel strikes of the same leg. The stride duration is equal for impaired and unimpaired side.
Stance duration	Time elapsed between heel strike and toe-off of the same foot, determined from the GRFs
Swing duration	Time elapsed between toe-off of and following heel strike of the same foot, determined from the GRFs
Derived parameters	
Step width variability	Standard deviation of step width
Duty factor	Quotient of stance duration and stride duration

7.3. Results

All subjects were able to complete the walking experiments. In the following sections, the results of the gait experiments with the powered prostheses E2 and E3 are presented. The interaction between human and motorized prosthesis as well as the changes in gait pattern and metabolic energy expenditure with variation of prosthesis support are presented.

7.3.1. Prosthesis ankle behavior

To verify the functioning of the prosthesis during the experiments, and to understand the individual subjects use of it, we first examine the overall behavior of the prosthetic ankle joint. Figure 7.5 shows the powered prosthetic ankle joint angle and torque trajectories averaged over all strides of the individual subjects. Shown is the resulting ankle joint behavior without separate consideration of the monoarticular and biarticular actuator. The prosthesis ankle joint behavior does not change noticeably with varying allocation κ between the mono- and biarticular actuator (not shown in Figure 7.5, but comprehensible from Figure 7.6).

Gray dashed lines represent the human reference angle $\varphi_{\text{Ank,ref}}$ and torque $M_{\text{Ank,ref}}$ utilized in the MLC control law (6.2). Solid black lines represent the actual angle and torque of the prosthesis, while the dotted line represents the desired torque $M_{\text{Ank,des}}$ resulting from the MLC control law and commanded to the LLCs. Shown in red are the ankle angle and torque resulting from the motion capture and inverse dynamics.

For all subjects, the ankle torque tracking performance shows negligible errors during the stance phase (dotted and solid black lines). During the swing phase, torque tracking errors are necessary to enable the prosthesis ankle angle to follow the reference angle trajectories in the MLC, as discussed for the walking controller results in Section 6.4.

S1 used the prosthesis in such a way that trajectories similar to the human reference trajectories (gray

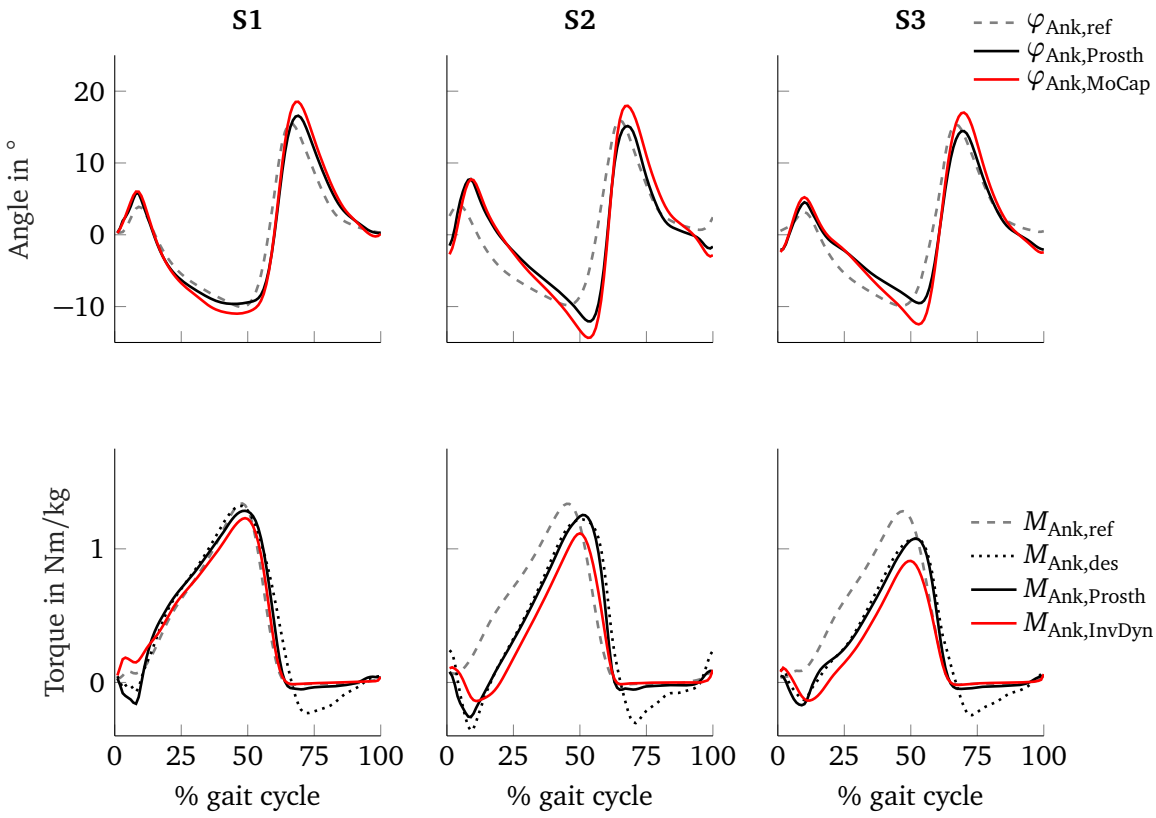

Figure 7.5.: Ankle angle and torque trajectories averaged over all strides of the subject. Prosthesis measurements and internal variables are shown in black, inverse dynamics and motion capture measurements in red.

dashed) are obtained at the ankle joint. S2 and S3 applied less load to the prosthetic ankle joint during the mid-stance phase, resulting in less dorsiflexion. This leads to reduced reference torques. For S2, the human reference trajectories (gray dashed) are slightly shifted in time, indicating that the heel strike initiating the stance phase is detected earlier than for S1 and S3.

Furthermore, the ankle trajectories measured from the motion capture system differ from the ankle angles measured with the prosthesis, especially at high ankle torque. This is due to the fact that the motion capture system measures the ankle angle resulting from the movement of the prosthetic ankle joint plus the deformation of the serial carbon spring, whereas the prostheses only measures the movement of the prosthetic ankle joint. The effect is more pronounced for S2 and S3, who are both significantly heavier than S1.

When comparing the ankle torques measured with the prostheses to those derived from the inverse dynamics, it is noticeable that there are discrepancies for S2 and S3. Those two subjects were amputated on the right side, whereas S1 was amputated on the left side. Hence, the errors are assumed to stem from GRF measurements of the left and right force plate of the treadmill.

7.3.2. Joint kinematics and kinetics

Figure 7.6 shows the grand mean ankle torque and power trajectories of the lower extremity joints. Presented are trajectories of the prosthetic ankle for no, medium and high biarticular support as well as average (for

all conditions) trajectories of the intact limb. The dashed lines show the data of the control group, where the gray shaded area represents ±1 STD. Subject individual trajectories can be found in Appendix C.

The prosthetic ankle joint movement is very close to the control group and shows slightly larger range of motion than the intact limb. The prosthetic ankle torque and consequently the power is lower than for the control group and the intact limb. The power still lies within ±1 STD of the control group, whereas the torque lies within ±2 STD of the control group.

Compared to the intact limb and the control group, the impaired side knee angle shows less flexion during early and mid stance. During the swing the range of motion (ROM) increases with increasing biarticular support. For medium κ the ROM is similar to the ROM of the control group. During early and mid stance the impaired side knee torque significantly deviates from the torque of the intact side and the control group. During late stance, the impaired side knee torque aligns to the intact side for increased κ. The increased flexion torque and flexion angle yield increased knee power absorption in late stance.

Intact side and impaired side hip ROM is larger than for the control group. Extension angle peak and flexion torque peak are shifted in time similar to the observed differences in the DF. The hip ROM does not change with varying κ, whereas the maximum flexion torque and power generation increase with increasing biarticular support. The hip torque aligns with increasing κ.

Looking at the individual joint kinematics and kinetics in Appendix C, it is worth noting, that the increases in grand mean knee power absorption and hip power generation mainly stem from S2 and are much more subtle for S1 and S3. Compared to S1 and S3, S2 responded to increasing κ with a much larger knee and hip ROM.

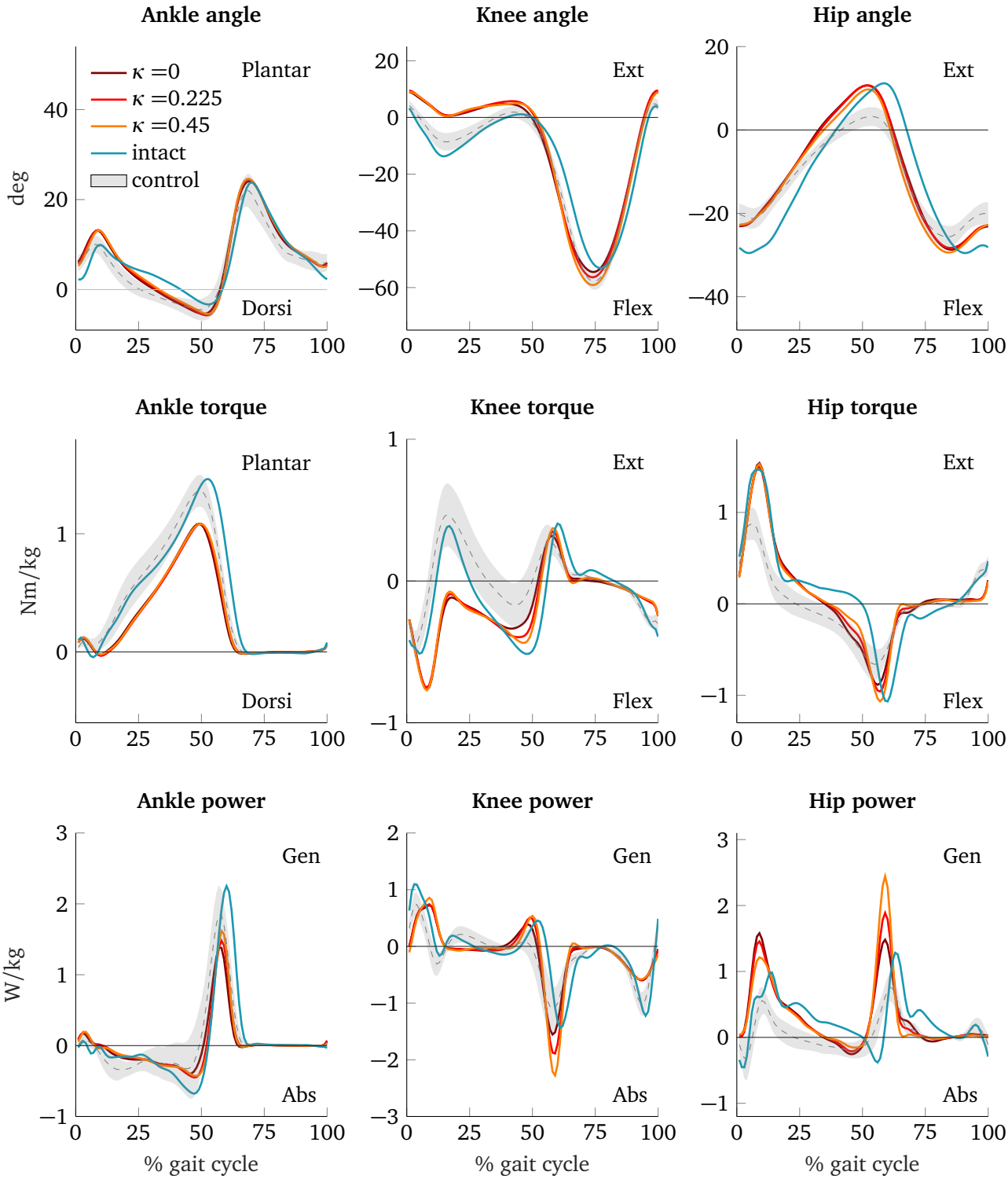

Figure 7.6.: Grand mean hip, knee and ankle joint angle, torque and power

7.3.3. Impaired side knee interaction

Figure 7.7 shows the grand mean impaired side knee behavior for no, medium and high biarticular support. With increasing κ the biological human knee flexion torque decreases while the extension torque increases. The biological knee power generation in late stance decreases with larger κ. The power absorbed by the biological human knee increases. This increase is equal to the power generated by the biarticular actuator and to a certain extent equal to the increase in the hip power generation shown in Figure 7.6.

There is no κ-dependent change in knee torque during early stance as well as swing phase, as during these phases the ankle torque is low or zero and therefore the biarticular actuator does not apply any force. In the early swing phase (at about 70 % gait cycle) two opposing bumps can be observed in the prosthesis and biological knee torque. These are due to increased force tracking errors resulting from the rapid movements of the prosthetic foot during early swing phase.

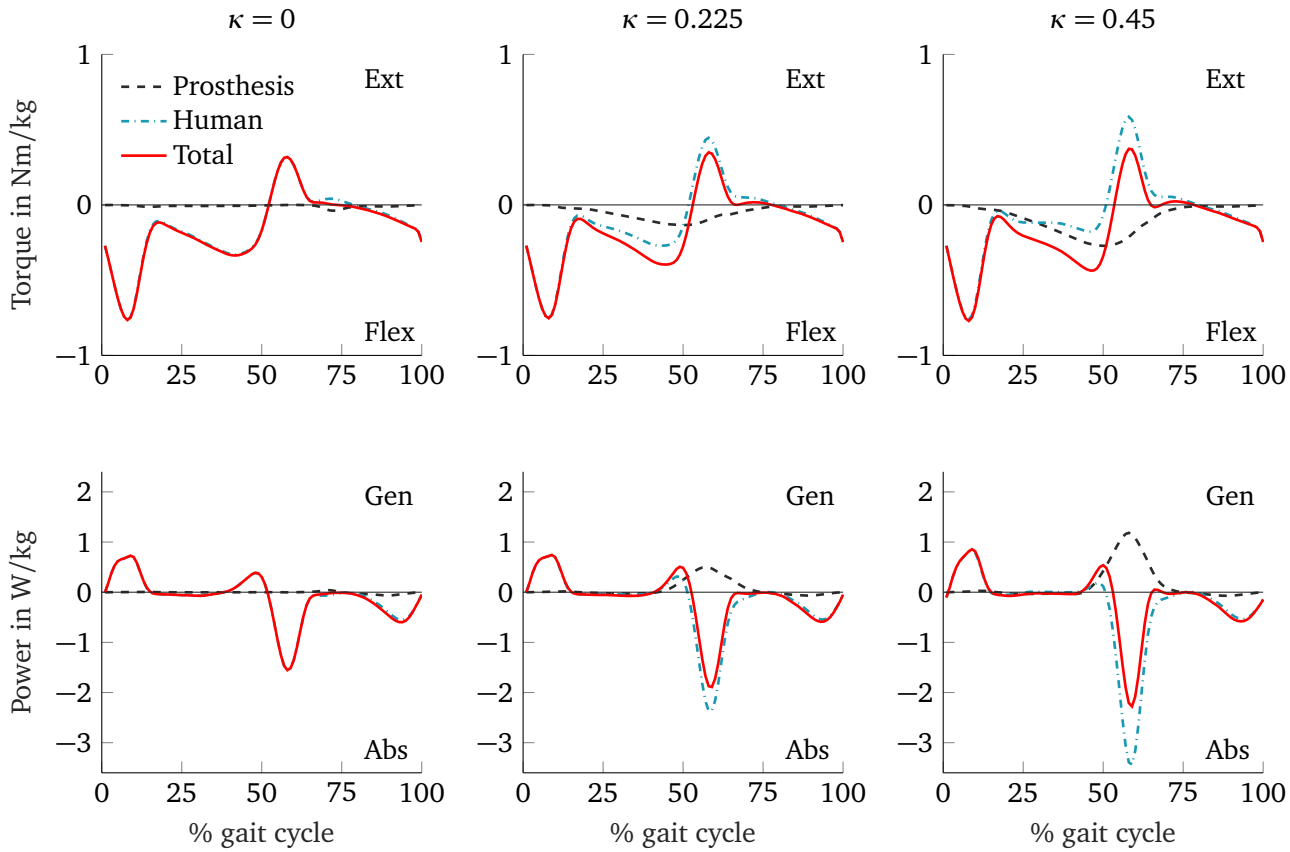

Figure 7.7.: Grand mean impaired side knee behavior: the top row shows the knee torque for no, medium and high biarticular actuator support, the bottom row shows the corresponding knee power.

7.3.4. Spatial and temporal parameters

The individual subjects did not show consistent responses to altered torque allocation κ between the mono- and biarticular actuator. Therefore, the observations are presented for each individual subject. Figure 7.8 shows the spatial and temporal gait parameters with altered allocation κ between the mono- and biarticular actuator, for both the impaired and the intact limb.

The stride length and synonymously the stride duration show no trend for S1 and S2, but clearly increase for S3 with increasing κ. With increased biarticular actuation, the stance as well as the swing duration equalize for S3.

For S1 not trend is observed for the DF. Subject S2 shows a marginal alignment of the DF for lower values of κ, whereas for S3 the DF equalizes with increasing values of κ. With increased biarticular actuation, the step length equalizes for S1 while it diverges for S2. Subject S3 shows no adaption of the step length. In the case of subject S1, who suffered paralysis of one arm on the prosthetic side, the step length behaves in the opposite way compared to the other subjects. S1 takes longer steps while standing on the prostheses, whereas S2 and S3 take longer steps while standing on the intact limb.

The step width as well as the step width variability (not shown) does not change significantly for any of the subjects.

Overall, with increased biarticular actuation S1 and S3 show equalizing trends in the parameters considered, whereas S2 shows diverging trends. This results in the observed grand mean presented in Figure 7.8.

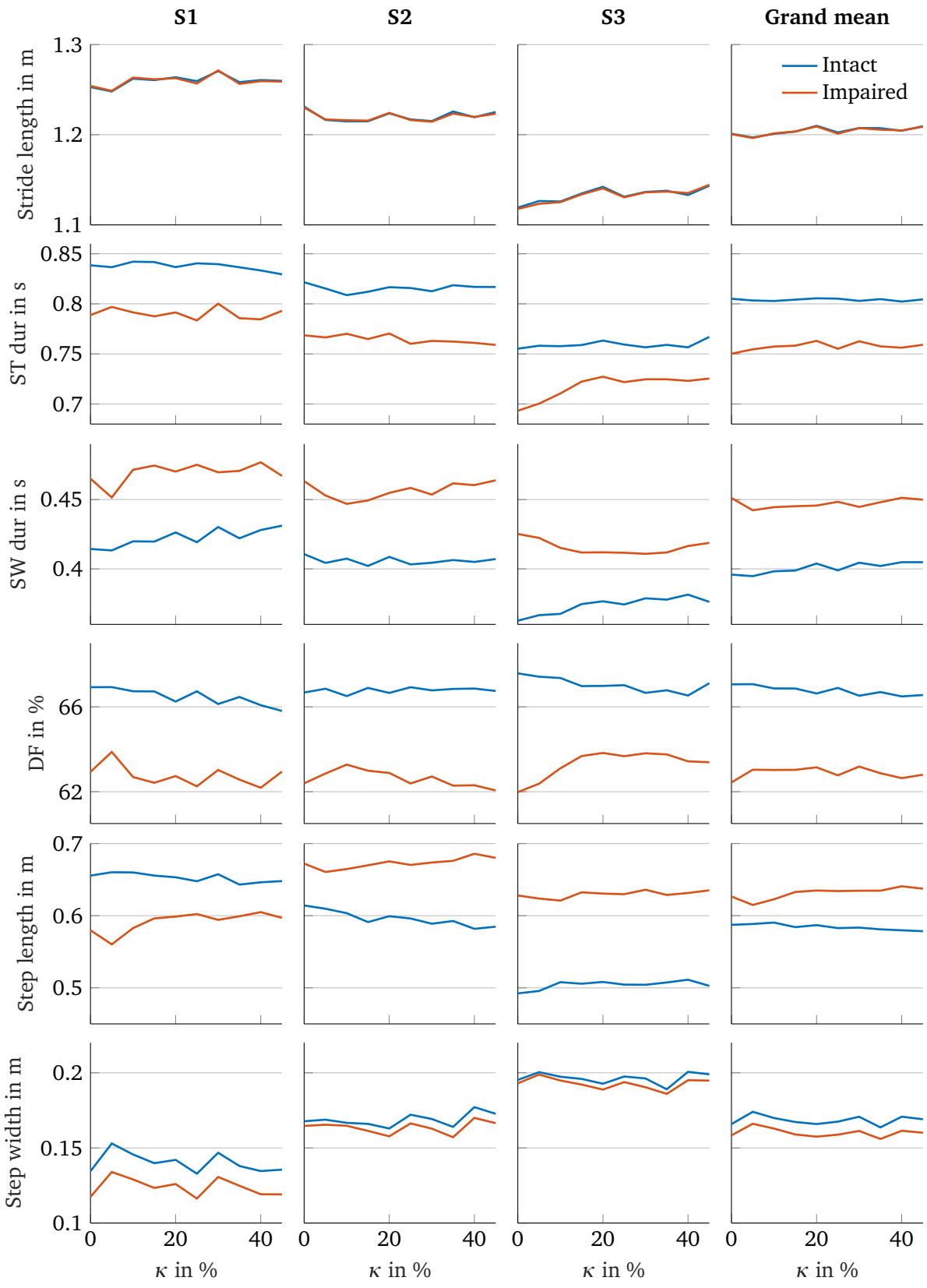

Figure 7.8.: Subject individual and grand mean spatial and temporal gait parameters for varying biarticular support κ. Acronyms: ST/stance, SW/swing, and DF/duty factor.

7.3.5. Energy expenditure

Figure 7.9 shows the net metabolic rate for the rising and falling flanks of κ as well as the average of both flanks for each individual subject. It can be seen that rising and falling edge are not congruent, especially for S2 and S3.

For S1 and S3 the net metabolic cost is the highest with solely monoarticular actuation ($\kappa = 0$). For all subjects, the averaged flanks indicate the largest reduction of the net metabolic rate for medium values of κ between 15 % and 30 %, resulting in a maximum reduction in the grand mean net metabolic rate of 8.5 % at $\kappa = 22\,\%$. In this value range for κ, the standard deviation of the net metabolic cost is the lowest at 2.5 %.

The net metabolic rates for $\kappa = 0$ of the rising and falling flank, marking the beginning and the end of the relevant time window of the measurement (see Figure 7.4), are within ±1.5 % for all subjects. This indicates a low drift of the metabolic rate measurement over the course of the experiment.

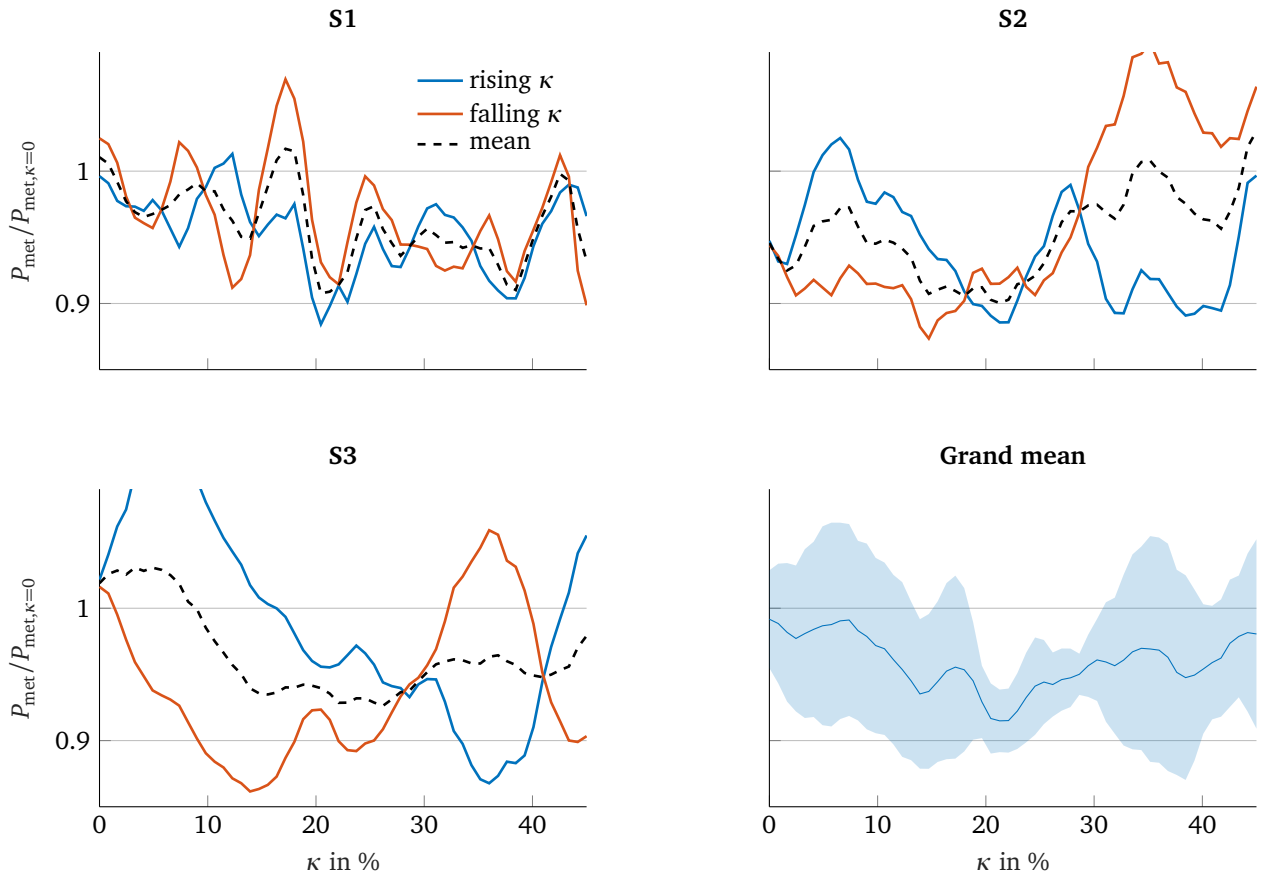

Figure 7.9.: Net metabolic rate normalized to the average net metabolic rate measured before the rising flank of κ started. Blue lines show the rate measured during rising flanks of κ, red lines show the rate measured during falling flanks. Dashed line show the average measured during rising and falling flanks. The grand mean plot shows mean and standard deviation among all rising and falling flanks.

7.3.6. Free walking at higher speeds and subjective feedback

The first subject could not tell any difference in the actuation over the course of the long experiment with slowly varying κ (E2), but did realize more abrupt changes during the free walking experiment (E3). He described that the powered prosthesis is noticeably heavier than his own prosthesis and because of that walking with the powered prosthesis is noticeably harder than with his own prosthesis. At higher speeds, the powered prosthesis feels lighter than at slow speeds, but still heavier than his own passive prosthesis. During the free walking experiment (E3) the subject could specify his preferred support level in a range with an accuracy of ±5 %

The second subject did realize changes in the actuation over the course of the experiment (E2). He felt that the support was raised to a maximum and then returned back to a minimum. He described that walking was hardest with solely monoarticular actuation and got easier with biarticular actuation. Without biarticular actuation the subject felt to work harder in the hip flexors. He further described that higher biarticular actuation catapults the leg forward and the subject feels like he wants to walk faster to catch the leg again. The subject stated that the prosthesis feels less heavy at higher speeds. The subject reported that numbness and slight emerging pain in the stump caused additional effort in the second half of the experiment. During the free walking experiment (E3) the subject could very precisely specify his preferred level of biarticular support.

The third subject reported slight emerging pain in the stump after one third of the experiment (E2) and that walking got more demanding. The subject could not tell any difference in the actuation over the course of the experiment (E2). He felt better walking on his own passive prosthesis and described that walking on the powered prosthesis felt harder. He reported that the powered prosthesis moved to much and that he felt more convenient on his own prosthesis. He felt like he had to raise the foot higher to prevent stumbling. He described that even at higher speeds of 1.4 m/s he could not feel the powered prosthesis support and felt that he could walk better on his own prosthesis. During free walking (E3) the subject could not clearly commit to a preferred level of biarticular support.

All subjects reported, that the still standing before and after the walking experiment (E2) felt unpleasant in the stump.

Figure 7.10 shows the preferred κ of the three subjects for various speeds. The bars correspond to variations of κ, for which the subjects did not notice any difference. Subject S2 could clearly distinguish slight changes in κ, for which there are no bars. In general, there is a trend towards higher values of κ for increased walking speeds.

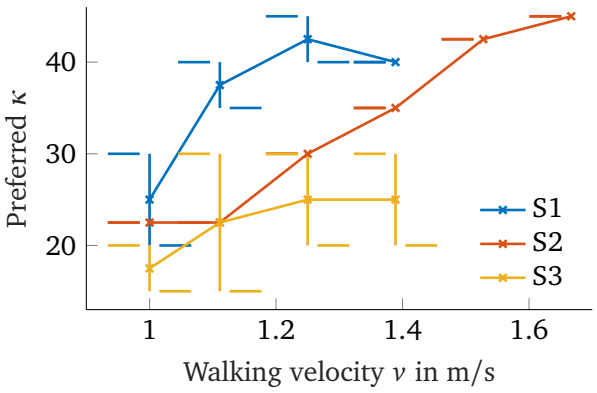

Figure 7.10.: Preferred support level κ for the biarticular actuator for various walking speeds from free walking experiment (E3). The bars indicate values of κ that the subjects found indistinguishable.

7.4. Discussion

As intended, the prosthesis provided unchanged support at the ankle and changing support at the knee by varying the biarticular support κ. For the heavier subjects S2 and S3, the ankle torque and power were too low due to the elasticity of the carbon foot, but still lay within two STD of the control group. The feedback of the heaviest subject of not being sufficiently supported by the prostheses coincides with the reduction of support due to the yielding carbon spring. Therefore, and because the prosthetic ankle-knee interaction functioned as desired, the walking experiment results can nonetheless be considered usable. Nevertheless, it is possible that as a result of the too low support the experiments potentially cannot highlight certain effects that would be visible with higher support. Furthermore, two of the subjects gave feedback that they could have performed the experiment at higher walking speed, possibly increasing observed effects or giving further insights.

Kinetics

In mid stance the impaired side knee torque is negative, hence it is missing the positive extension torque peak. This can either be characteristic to the specific gait of the subjects, or to some extend be a result from the marker application at the knee orthosis joint (instead of the skin) and the movement of the stump inside the shaft. In Eilenbergs evaluation of the artificial gastrocnemius in [44] similarly low, but still positive knee flexion torques are observed.

In the terminal stance the knee flexion torques equalize between intact and impaired sides for increasing values of κ, an effect that was not observed in the evaluation of the monoarticular BiOM powered prosthetic foot [10] and was not that distinct in study with the powered gastrocnemius Eilenberg et al. conducted in [44]. With the equalization of the knee flexion torques the hip torque also aligns.

In the terminal stance, the power generation at the knee increases slightly, whereas in pre-swing the knee power absorption increases. Simultaneously, the power generation at the hip increases. This power transfer can possibly be established by the biarticular rectus femoris muscle, indicating that through the increasing activity of the artificial gastrocnemius muscle an overall power transfer from the distal ankle to the proximal hip joint takes place.

Spatiotemporal parameters

Overall, modifications of the biarticular actuation resulted in only small and among subjects opposite changes in the spatiotemporal parameters. This variation in the results is somewhat expected, since the group of subjects is small and the individual subjects differ in age, height and weight, constitution, and individual characteristics such as the paralyzed arm of S1.

Slight alignments in the phase durations (ST and SW) and consequently also in the DF are observed. The intact limb DF decreases and the impaired limb DF increases with rising κ, resulting in a reduced DF asymmetry. Subjects shift more weight onto the impaired side, which indicates increasing confidence in loading the prosthetic leg.

Asymmetries in the step length are of similar magnitude as reported in other studies [10], whereas the asymmetries in the temporal parameters are larger than in [10]. This might be due to the short training time in this work.

Energy expenditure and subjective feedback

A reduction in the metabolic power was found for all subjects. Compared to Eilenberg et al. [44], who, when comparing solely monoarticular to mono- plus biarticular actuation, reported metabolic power reductions

in 4 out of 6 subjects, we observed metabolic power reductions for all subjects. The grand mean reduction of these 4 subjects in [44] is $(-7.3 \pm 5)\,\%$ and therefore of similar magnitude as our observations.

The subjectively preferred biarticular support at 1.0 m/s was close to where the maximum metabolic cost reduction occurred. However, Medrano et al. [117] demonstrated that the average just noticeable difference of metabolic rate with an ankle exoskeleton was $22.7 \pm 5.35\,\%$. Therefore the observed changes in metabolic rate are much lower than what the participants can reliably detect, and the goodness functions of the subjects must be different from the metabolic cost.

There are several possible explanations for the observed reduction in metabolic cost: First it was seen that the biological knee flexion torque was reduced by the biarticular actuator accompanied by a small reduction in biological knee power generation. As metabolic cost of walking can be explained by muscular force [118] this reduction in knee torque is likely to contribute to the metabolic cost reduction. As knee extension torque increases with increasing biarticular support, it is obvious that the metabolic cost reduction decreases for κ becoming too large. Second, the artificial gastrocnemius generated power at the knee, which altered the power absorption at the biological knee and power generation at the hip. It can be assumed that the power from the knee is transported to the hip with the help of the biarticular rectus femoris muscle. As during the relevant phase the knee and hip both flex, the rectus femoris operates at slow velocities providing efficient energy transport [22]. Thus, it could be assumed that appropriate biarticular support enables isometric force generation of the rectus femoris, thereby reducing the load on monoarticular hip flexors. Since metabolic energy expenditure is lower in isometric force generation than in active contraction [119], this could potentially reduce the metabolic energy expenditure. The effect could be enhanced by better engagement of elastic, energy storing elements of the muscles. Therefore it is likely that the artificial gastrocnemius contributed to thigh acceleration and swing initiation by antagonizing the rectus femoris and reducing the load in the remaining leg muscles. Evidence could be obtained by recording muscle activity with an identical experimental protocol. Higher biarticular support further reduced early stance hip power generation, but did not yield further reductions in the metabolic energy expenditure.

Limitations

A relevant amount of the observed changes in the joint torque and power occur during DS. In this phase, the instrumented treadmill only measures the combined anterior GRF of both legs. The approach used to decompose the GRF [112] is only validated for unimpaired subjects and force plates. As the overall observed kinematics are close to the control group kinematics, it can be assumed, that the chosen approach for GRF decomposition during DS is still valid.

7.5. Conclusion

This study has shown that an artificial gastrocnemius muscle can potentially equalize the kinematics and kinetics between the intact and the affected leg. In addition to the directly actuated joints, proximal joints are also affected and a reduction of the metabolic cost occurs for medium biarticular support. It is reasonable to assume that observed reductions in metabolic costs are due to the modified energy transfer between joints in addition to the reduction in biological torques.

Next to the kinematic and kinetic parameters, changes were seen in the spatiotemporal parameters. However, these were not uniform among subjects and smaller than expected.

Compared to the metabolic cost measurement, the subjects were able to determine their personal preference relatively quickly. This was approximately in line with the maximum metabolic cost reduction. It is conceivable that shortened experiments with increased knowledge gain could be possible in this way.

The walking speed at 1 m/s was lower than in comparable studies. Walking at higher speeds is likely to increase the observed effects and maybe give further insights, as biarticular gastrocnemius muscle is known to contribute thigh acceleration [120] and swing initiation [22]. Imbalances from the missing gastrocnemius function and overemphasized soleus function are therefore expected to be more distinct at higher speeds.

8. Conclusion and future work

8.1. Conclusion

This thesis describes the development of an artificial gastrocnemius (AG) to extend a monoarticular prosthetic foot, and the evaluation of this new prototype with individuals with TTA. The system comprises a powered prosthetic foot mimicking the monoarticular soleus and tibialis anterior muscles and a Bowden cable actuator mimicking the biarticular gastrocnemius muscle. The resulting prototype features all major sagittal plane muscles of the human ankle joint. It can fully reproduce the sagittal plane human ankle biomechanics of level walking with a freely selectable allocation of torque between the mono- and biarticular actuators. The main contributions of the thesis are twofold. First, the systematic design of the hardware with all necessary steps for development and implementation is described. Second, the potential of the prosthesis to influence the gait pattern and effort is evaluated in a suitably designed study with three subjects with TTA.

The new prototype is based on an existing monoarticular powered prosthetic foot. The systematically designed AG prototype consists of an offboard placed actuator with a pulley and a Bowden cable with inner steel cable. This setup allows to transfer the desired forces to the user without adding the weight of an additional actuator, and therefore minimizes effects on the biomechanics and energetics of the user caused by additional weight. The hardware has proven to be reliable even during several hours of tests and experiments with high forces above 400 N. The design methodology and implementation can be transferred to other human joints and individual components can be adopted for other hardware setups in the literature.

The designed hardware is put into operation to enable walking on the treadmill with arbitrary allocation of torque between mono- and biarticular actuator. The modeling of both actuators is presented, and both the monoarticular prosthetic foot as well as the AG represent SEAs. All necessary steps for the identification of the model parameters are presented and can be prototypically transferred to similar setups.

A hierarchical control structure for the evaluation on the treadmill is developed, consisting of a low level torque controller and a high walking controller. A PI control with state feedback is chosen for the low level torque control. It utilizes the motor velocity and output torque (or force), which are the measured variables commonly available within SEAs. Unlike straightforward control of the output torque, the approach uses all measurements available in the SEA and thus has more capabilities to shape the closed loop dynamics. In contrast to cascaded controllers, which also use all measurements available in the SEA, the design of the proposed controller can be done in one single design step. Based on human reference data, the LLC closed loop bandwidth is chosen high enough such that the controlled actuators represent ideal torque sources to the higher level controllers.

The walking controller uses prototypical trajectories of unimpaired subjects and an impedance mid-level control law, to generate desired torques for the LLC. As a result, the prosthetic ankle behaves similar to an unaffected human ankle joint when loaded similar to the human reference behavior and responds in an appropriate manner to deviations from this reference. The reference torque generation can be easily adapted independently of the prosthesis hardware, for example to the user weight or individual mounting of the prosthesis. The prototypical trajectories provide an easy access to influence the joint behavior, by adjusting the torque and angle trajectories.

With detection of the heelstrike and toe-off, the gait phase is estimated separately for stance and swing

phase. Thus, the assistance is provided with appropriate timing even at altered duty factors, which are likely to occur when using new prosthetic hardware. The quality of the gait phase estimation depends on the quality of the event detection, with the toe-off in general being detected more accurately than the heel strike due to the clear zero crossing of the torque. The latter would benefit from suitable sensors to determine the heel contact. With ideal event detection, the gait phase estimation is accurate up to the degree of gait variability, which is negligible for steady walking.

The new biarticular prosthesis is initially evaluated with three subjects with TTA. To investigate both joint biomechanics and metabolic effort, a continuous sweep protocol is designed taking into account the measurement dynamics of the investigated variables. Within the experimental protocol, the assistance is steadily shifted from the monoarticular actuator to the AG and reverse.

All subjects show a tendency to reduced metabolic effort for medium activity of the AG, although noise level and time variation are large. For more significant results, a larger subject group and several repetitions of the experiment would be necessary. In addition to the metabolic effort, the AG is able to influence spatio temporal gait parameters between the impaired and the intact side, but partially opposing effects are observed among the individual subjects. Again, meaningfulness of the results could be improved by increased clinical effort, which is not in the scope of this work.

In summary, this thesis describes the implementation of an AG with freely selectable assistance between monoarticular actuators and biarticular actuators as well as a possible study design for the systematic investigation of metabolic effort and spatio-temporal gait parameters. It is shown that the addition of the AG as found in the biological example can positively affect the investigated gait parameters such as walking velocity and gait symmetry when compared to monoarticular actuation only.

8.2. Future work

8.2.1. Biarticular prosthesis hardware and controller design

The performance of the AG closed loop force controller shows that a good trajectory tracking can be achieved with consistent identification of model parameters and model based controller design taking advantage of the measurements available. In conclusion heuristic approaches or open-loop techniques trying to generate desired force trajectories are not necessary and should be avoided. Aiming at 10 Hz closed loop bandwidth will yield sufficient results for level walking. For the ROA, the controller performance is limited by the noise of the ankle encoder. Improved sensors would allow for faster controller tuning and results similar to the AG. In consequence, high quality measuring equipment should always be preferred in the prosthesis hardware.

In the present prototype, the carbon foot blade was chosen as stiff as available, and was assumed to be rigid for the MLC control law. As it turned out, this assumption was not valid and the carbon foot blade, acting in series to the ankle prosthesis SEA, increased the effective ankle movement. This problem can be solved in two ways: Either by designing the foot part specifically for the requirements of the prosthetic SEA, or by adjusting the reference trajectories in the MLC control law by the expected carbon foot deformation.

Like a powered prosthetic foot is bulky in terms of weight and setup procedure compared to a passive carbon spring, the hardware setup in the present work consisting of knee orthoses, powered prosthesis, external wiring and Bowden cable became even more challenging. Here, two particular noteworthy aspects are the donning of the prosthesis and the routing of the Bowden cables in such a way that they allow a free arm swing and enough range of motion on the treadmill. Even for the use in the laboratory, effort should be invested in the usability and handiness, allowing for more efficient studies. Basically, with the work from Eilenberg [16], Willson [50], the present work, and the many other exoskeleton and prosthesis prototypes in the literature, there is a recipe on how to implement a powered AG in transtibial prostheses and future

laboratory prototypes should be designed to allow the systematic testing with large subject groups.

In terms of an all day powered prosthesis featuring an AG, I think neat product design wont be enough and revolutions in the field of worn actuators are required. Until that point, further understanding of mono- and biarticular actuation at the ankle should be developed to know the requirements for actuators in future mobile prostheses and to have the concepts at hand, when future actuator technology allows new prostheses concepts.

8.2.2. Biomechanical evaluation

For clinical evaluation, the subject group should be increased to obtain meaningful results and to understand the effects of biarticular actuation in transtibial prostheses The walking speed should be chosen higher than in the present thesis, because the effects of the powered ankle joint as well as the AG are likely to be better observable in this case. This is also supported by two observations: First, the majority of the subjects in this work retrospectively report that they could walk at a higher walking speed over a longer period of time even with the unfamiliar prosthesis. Second, the subjects subjectively preferred increased AG support at higher walking speeds. Hence, one goal in the future should be to increase the evaluation effort and the walking speed to systematically understand the effect of biarticular actuation in transtibial prostheses.

In addition to systematic feedforward evaluation, insights might be gained if subjects can manually tune their preferred prosthetic assistance. Experiments with an ankle exoskeleton [121] showed that users can repeatedly identify their preferred assistance with small errors in less than two minutes. Intermediate feedback from actual prosthesis users is given little weight in the studies found in the literature, but could provide guiding thoughts. Metabolically optimal support is unlikely to be found this way because the resolution of human perception is too low [117]. The continuous sweep protocol proposed in this work provides reasonable resolution with tolerable experiment time, on the condition that the parameter space has very few dimensions. The main limiting factor is the measurement dynamics of the metabolic effort. Insightful experiments would be possible if the metabolic effort can be estimated more quickly. A promising indicator for the change in metabolic effort might be the measurement of muscle activity by surface EMG, which responds to changes in effort within a few strides [122]. Possibly, this will allow employing human in the loop optimization techniques for future prosthesis tuning. If not, a lot of time has to be invested on the treadmill, anyway.

A. Modeling and identification supplements

A.1. ROA spring lever kinematic

The lever arms h_M and h_S of the motor and the spring illustrated in Figure A.1 will be derived in the following paragraphs.

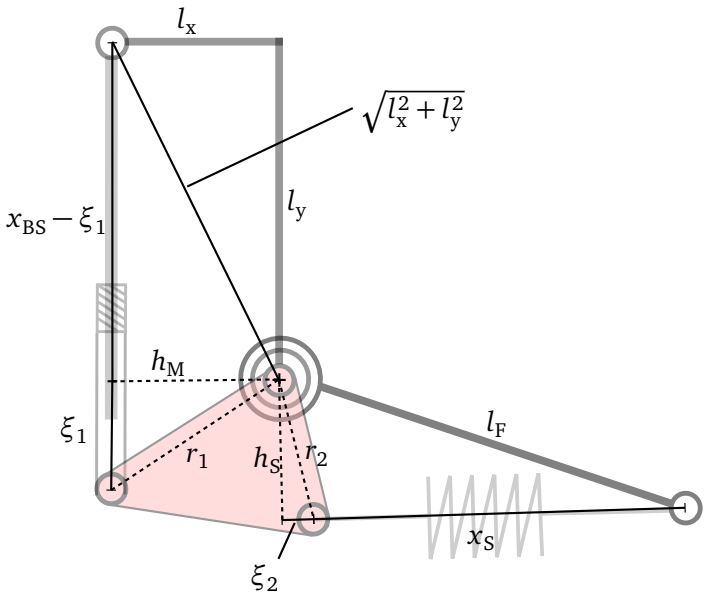

Figure A.1.: Schematic structure of the ROA prosthetic foot with kinematic parameters and variables used to derive the lever arms h_M and h_S

For the left spindle triangle, the equations

$$l_x^2 + l_y^2 = h_M^2 + (x_{BS} - \xi_1)^2 \tag{A.1}$$

$$r_1^2 = h_M^2 + \xi_1^2 \tag{A.2}$$

follow with Pythagorean theorem. Subtracting equations (A.2) and (A.1) eliminates h_M^2. Solving one equation for h_M^2 and substituting into the other eliminates h_M and allows solving for ξ_1 as

$$\xi_1 = \frac{x_{BS}^2 + r_1^2 - l_x^2 - l_y^2}{2x_{BS}} .$$

This expression for ξ_1 can be substituted in equation (A.2) to derive the expression (4.10) for h_M presented in Chapter 4.

Similarly

$$l_{\mathrm{F}}^2 = h_{\mathrm{S}}^2 + (x_{\mathrm{BS}} + \xi_2)^2$$
$$r_2^2 = h_{\mathrm{S}}^2 + \xi_2^2 \tag{A.3}$$

applies for the lower spring triangle, from which

$$\xi_2 = \frac{l_{\mathrm{F}}^2 - r_2^2 - x_{\mathrm{S}}^2}{2x_{\mathrm{S}}}$$

can be derived. Substituting ξ_2 into equation (A.3) results in

$$h_{\mathrm{S}}^2 = r_2^2 - \left(\frac{l_{\mathrm{F}}^2 - r_2^2 - x_{\mathrm{S}}^2}{2x_{\mathrm{S}}}\right)^2 ,$$

which is equal to the expression for h_{S} given in equation (4.9).

A.2. Controllers for identification process

In this section, the controllers used during the identification of the ROA and AG model parameters in Chapter 4 are described.

A.2.1. Motor velocity

The motor velocity is estimated from the motor position measured with the motor encoder via backward differences. The transfer function of the motor velocity is

$$\frac{\dot{\varphi}_{\mathrm{M}}(s)}{I(s)} = \frac{c_{\mathrm{M}}}{Js + d} .$$

A PI feedback controller is suitable to control the motor velocity and can be designed without knowledge of the model parameters. With the controller transfer function $K_{\mathrm{P}} + \frac{K_{\mathrm{I}}}{s}$, the closed loop velocity transfer function results in

$$G_{\dot{\varphi}_{\mathrm{M}}\mathrm{c,PI}}(s) = \frac{c_{\mathrm{M}}K_{\mathrm{P}}s + c_{\mathrm{M}}K_{\mathrm{I}}}{Js^2 + (d + c_{\mathrm{M}}K_{\mathrm{P}})s + c_{\mathrm{M}}K_{\mathrm{I}}}$$

and for $K_{\mathrm{I}} = 0$

$$G_{\dot{\varphi}_{\mathrm{M}}\mathrm{c,P}}(s) = \frac{K_{\mathrm{P}}c_{\mathrm{M}}}{Js + d + K_{\mathrm{P}}c_{\mathrm{M}}} .$$

To tune the controller, first the integral gain K_{I} is set to zero and K_{P} is increased until the closed loop step response is sufficiently fast. Then K_{I} is increased such that the closed loop step response overshoots as desired and the steady state error disappears. This procedure can be made plausible with the help of the root-locus method or the Hurwitz stability criterion.

For the ROA, the controller parameters

$$K_{\mathrm{P}} = 0.12 \qquad K_{\mathrm{I}} = 1$$

result in a settling time of 20 ms with no overshoot. For the AG, the controller parameters

$$K_{\mathrm{P}} = 0.1 \qquad K_{\mathrm{I}} = 5$$

yield a settling time of approximately 30 ms with 10 % overshoot.

A.2.2. Motor position

To control the motor position of the ROA, a PD feedback controller $K_\mathrm{P} + K_\mathrm{D}s$ is used. For the identification purposes, no stationary accuracy of the position control is required, for which reason no integral component is used.The derivative gain is implemented using backward differences. Together with the PD feedback controller the closed loop transfer function results in

$$G_{\varphi_\mathrm{M}\mathrm{PD}}(s) = \frac{K_\mathrm{P} + K_\mathrm{D}s}{Js^2 + (d + K_\mathrm{D})s + K_\mathrm{P}} \,.$$

From the Hurwitz criterion it is obvious that the closed loop transfer function is stable for $K_\mathrm{P} > 0$ and $K_\mathrm{D} > 0$. To tune the controller, K_P and K_D can be iteratively increased to achieve the desired closed loop behavior, where the settling time is adjusted by K_P and the damping is adjusted by K_D. The controller parameters

$$K_\mathrm{P} = 2.4 \qquad \text{and} \qquad K_\mathrm{D} = 0.025$$

yield a settling time of 80 ms with an overshoot of 25 % and negligible steady state error.

A.2.3. AG output force

To identify the stiffness of the AG user interface, it is useful to be able to control the output force of the actuator. A cascaded controller with inner velocity and outer force loop, both comprising only a proportional control, as shown in Figure A.2 is the most simple controller to to realize without any knowledge of the model parameters.

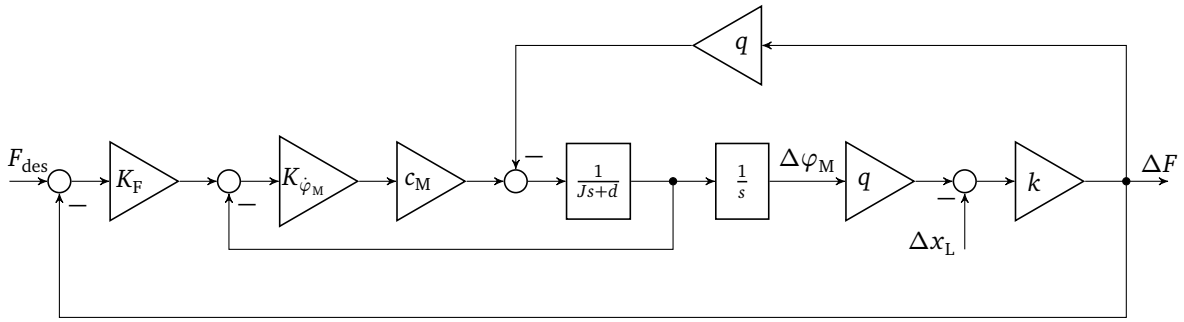

Figure A.2.: Block diagram of the AG with cascaded controller.

With the controller gains K_F and $K_{\dot{\varphi}_\mathrm{M}}$ of the outer force and inner velocity controller, the closed loop transfer function becomes

$$\frac{\Delta F(s)}{F_\mathrm{des}(s)} = \frac{K_\mathrm{F}K_{\dot{\varphi}_\mathrm{M}}qkc_\mathrm{M}}{Js^2 + (d + K_{\dot{\varphi}_\mathrm{M}}c_\mathrm{M})s + q^2k + K_\mathrm{F}K_{\dot{\varphi}_\mathrm{M}}qkc_\mathrm{M}} \,.$$

It is easy to see that the closed loop transfer function is Hurwitz stable for $K_\mathrm{F} > 0$ and $K_{\dot{\varphi}_\mathrm{M}} > 0$, and that $K_{\dot{\varphi}_\mathrm{M}}$ can adjust the damping and the product $K_\mathrm{F}K_{\dot{\varphi}_\mathrm{M}}$ can adjust the settling time and the steady state error. The controller gains can easily be tuned by hand for implementation purposes and can be based on the P-velocity control from the friction identification. For the initial identification of the AG stiffness, the following pair of controller gains was used:

$$K_{\dot{\varphi}_\mathrm{M}} = 0.1 \qquad K_\mathrm{F} = 5 \,.$$

Obviously a PD-force controller would offer the same degrees of freedom as the proposed cascaded controller, but would have been more sensitive to the noise of the force measurement.

B. Biarticular prosthesis study evaluation

B.1. Instrumented treadmill ADAL-WR

The treadmill (type ADAL-WR, HEF Tecmachine, France) has eight single axis piezoelectric force sensors L1 to L4 and R1 to R4. These are used to measure the vertical ground reaction forces in the two force plates underneath the belt. The thickness of the forceplates is measured at 30 mm. The thickness of the belt is 3 mm. A bottom force plate underneath with four multi axis piezoelectric force sensors is used to measure the horizontal ground reaction forces. This platform also carries the motor, belt, and the front and rear platforms.

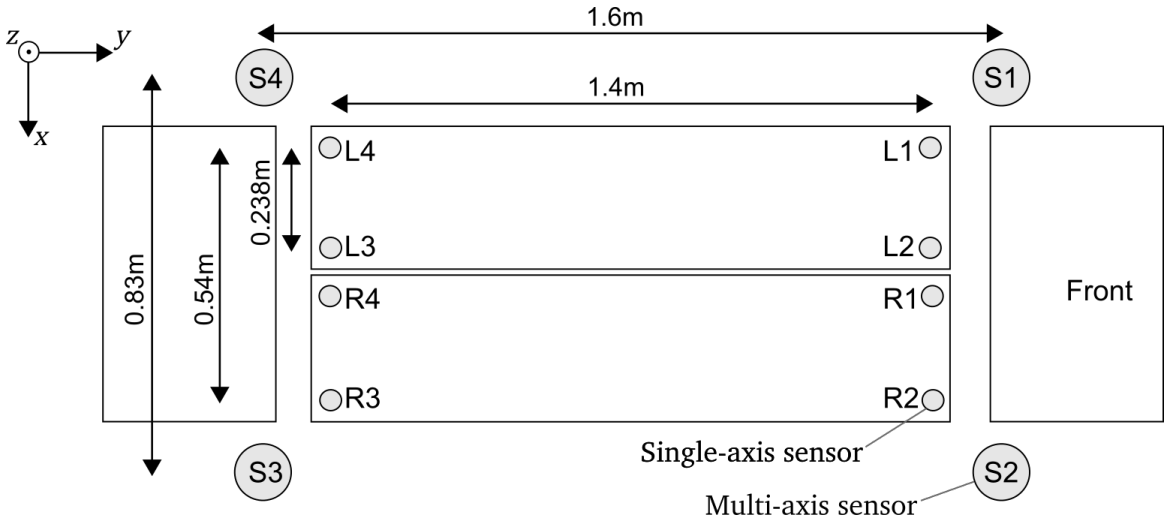

Figure B.1.: ADAL3D-WR treadmill sensor arrangement and dimensions. Illustration based on [123]

B.2. Center of pressure

Let $F_{z,\text{Front}}$ be the vertical forces measured at the front of the force plate (L1+L2 or R1+R2) and $F_{z,\text{Rear}}$ be the forces measured at the rear of the force plate (L3+L4 or R3+R4) as illustrated in Figure B.2. Torque equilibrium around the lower left corner leads to

$$y_{\text{COP}} F_z = l_y F_{z,\text{Front}} + h F_y \tag{B.1}$$

and with $F_z = F_{z,\text{Rear}} + F_{z,\text{Front}}$ the center of pressure (COP) is calculated as

$$y_{\text{COP}} = \frac{l_y F_{z,\text{Front}} + h F_y}{F_{z,\text{Rear}} + F_{z,\text{Front}}} \,. \tag{B.2}$$

As $F_{y,\text{Front}}$ and $F_{y,\text{Rear}}$ are not measured in the given setup. Therefore the force F_y is assumed to be equal to the horizontal forces measured in the bottom plate.

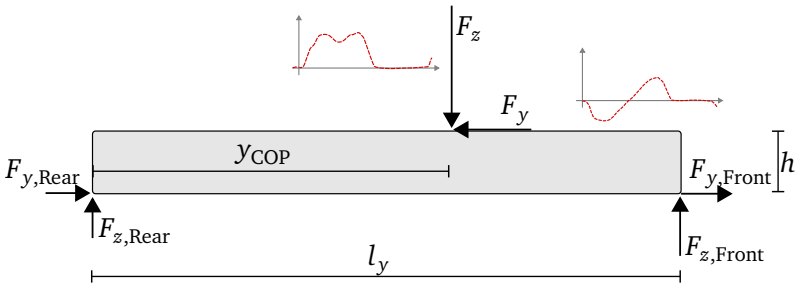

Figure B.2.: Schematic side view of the force plate with relevant forces. Typical force trajectories for level walking are indicated in red.

B.2.1. Center of pressure correction

In general, inverse dynamic results are highly sensitive to errors in COP [124]. Pretest showed, that the inverse dynamic results did not match the internal prosthesis torque measurements. As measurement of the sensor characteristics of the individual built-in sensors was not possible, a recalibration of the individual sensors could not be carried out.
Hence, a correction of the calculated COP similar to [125] was conducted. For this purpose, the treadmill is loaded at defined points with the aid of a calibration rod. With the focus on sagittal plane inverse dynamics, the calibration points were chosen to cover the total length of the force plates and to match typical stride widths. Calibration points are laid out using 3D printed templates (see Figure B.3). A 50 kg dumbbell bar with a guiding tip (6 mm diameter) was used to load the calibration points.

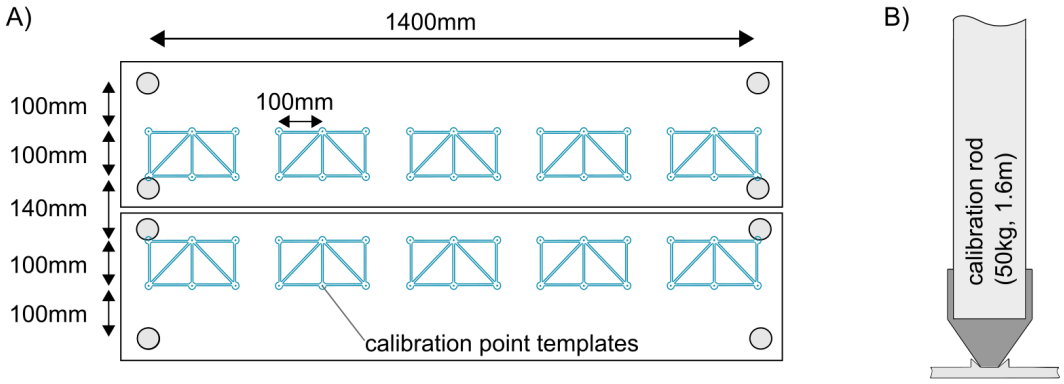

Figure B.3.: A) Calibration points on the treadmill laid out with 3D printed templates, and B) schematic illustration of the calibration rod loading a calibration point.

A 3rd order polynomial is fitted to the error

$$\Delta y_{\mathrm{COP}}(\tilde{y}_{\mathrm{COP}}) = a_0 + a_1\tilde{y}_{\mathrm{COP}} + a_2\tilde{y}^2_{\mathrm{COP}} + a_3\tilde{y}^3_{\mathrm{COP}}$$

and the corrected COP is calculated as

$$y_{\mathrm{COP,corr}} = \tilde{y}_{\mathrm{COP}} + \Delta y_{\mathrm{COP}}(\tilde{y}_{\mathrm{COP}})\,.$$

B.3. Inverse dynamics

The inverse dynamic procedure can be performed independently for each leg. In the following, y_{Ji} and z_{Ji} are the joint coordinates, y_i and z_i are the segment center of mass coordinates, F_{yi} and F_{zi} are the joint reaction forces, M_i is the joint torque, m_i is the joint mass, and I_i is the segment mass moment of inertia.

In particular, $F_{y0} = -F_{y,\mathrm{GRF}}$ and $F_{z0} = -F_{z,\mathrm{GRF}}$ are the horizontal and the vertical ground reaction forces measured from the treadmill, and $y_{J0} = y_{\mathrm{COP}}$ and $z_{J0} = z_{\mathrm{COP}}$ are the center of pressure coordinates.

Forces

The translational equations of motion of the three body segments are

$$
\begin{aligned}
m_1\ddot{y}_1 &= F_{y1} - F_{y0} \\
m_1\ddot{z}_1 &= F_{z1} - F_{z0} - m_1 g \\
m_2\ddot{y}_2 &= F_{y2} - F_{y1} \\
m_2\ddot{z}_2 &= F_{z2} - F_{z1} - m_2 g \\
m_3\ddot{y}_3 &= F_{y3} - F_{y2} \\
m_3\ddot{z}_3 &= F_{z3} - F_{z2} - m_3 g
\end{aligned}
$$

Given the segment center of mass accelerations and the ground reaction forces, the joint reaction forces

$$
\begin{aligned}
F_{y1} &= F_{y0} + m_1\ddot{y}_1 \\
F_{z1} &= F_{z0} + m_1\ddot{z}_1 + m_1 g \\
F_{y2} &= F_{y1} + m_2\ddot{y}_2 \\
F_{z2} &= F_{z1} + m_2\ddot{z}_2 + m_2 g \\
F_{y3} &= F_{y2} + m_3\ddot{y}_3 \\
F_{z3} &= F_{z2} + m_3\ddot{z}_3 + m_3 g
\end{aligned}
$$

can be calculated explicitly.

Torques

The rotational equations of motion are

$$
\begin{aligned}
J_1\ddot{\varphi}_1 &= M_1 \qquad\quad - F_{y0}(z_1 - z_{J0}) + F_{z0}(y_1 - y_{J0}) + F_{y1}(z_1 - z_{J1}) - F_{z1}(y_1 - y_{J1}) \\
J_2\ddot{\varphi}_2 &= M_2 - M_1 - F_{y1}(z_2 - z_{J1}) + F_{z1}(y_2 - y_{J1}) + F_{y2}(z_2 - z_{J2}) - F_{z2}(y_2 - y_{J2}) \\
J_3\ddot{\varphi}_3 &= M_3 - M_2 - F_{y2}(z_3 - z_{J2}) + F_{z2}(y_3 - y_{J2}) + F_{y3}(z_3 - z_{J3}) - F_{z3}(y_3 - y_{J3})
\end{aligned}
$$

and can be explicitly converted according to the joint moments

$$
\begin{aligned}
M_1 &= \qquad J_1\ddot{\varphi}_1 + F_{y0}(z_1 - z_{J0}) - F_{z0}(y_1 - y_{J0}) - F_{y1}(z_1 - z_{J1}) + F_{z1}(y_1 - y_{J1}) \\
M_2 &= M_1 + J_2\ddot{\varphi}_2 + F_{y1}(z_2 - z_{J1}) - F_{z1}(y_2 - y_{J1}) - F_{y2}(z_2 - z_{J2}) + F_{z2}(y_2 - y_{J2}) \\
M_3 &= M_2 + J_3\ddot{\varphi}_3 + F_{y2}(z_3 - z_{J2}) - F_{z2}(y_3 - y_{J2}) - F_{y3}(z_3 - z_{J3}) + F_{z3}(y_3 - y_{J3})
\end{aligned}
$$

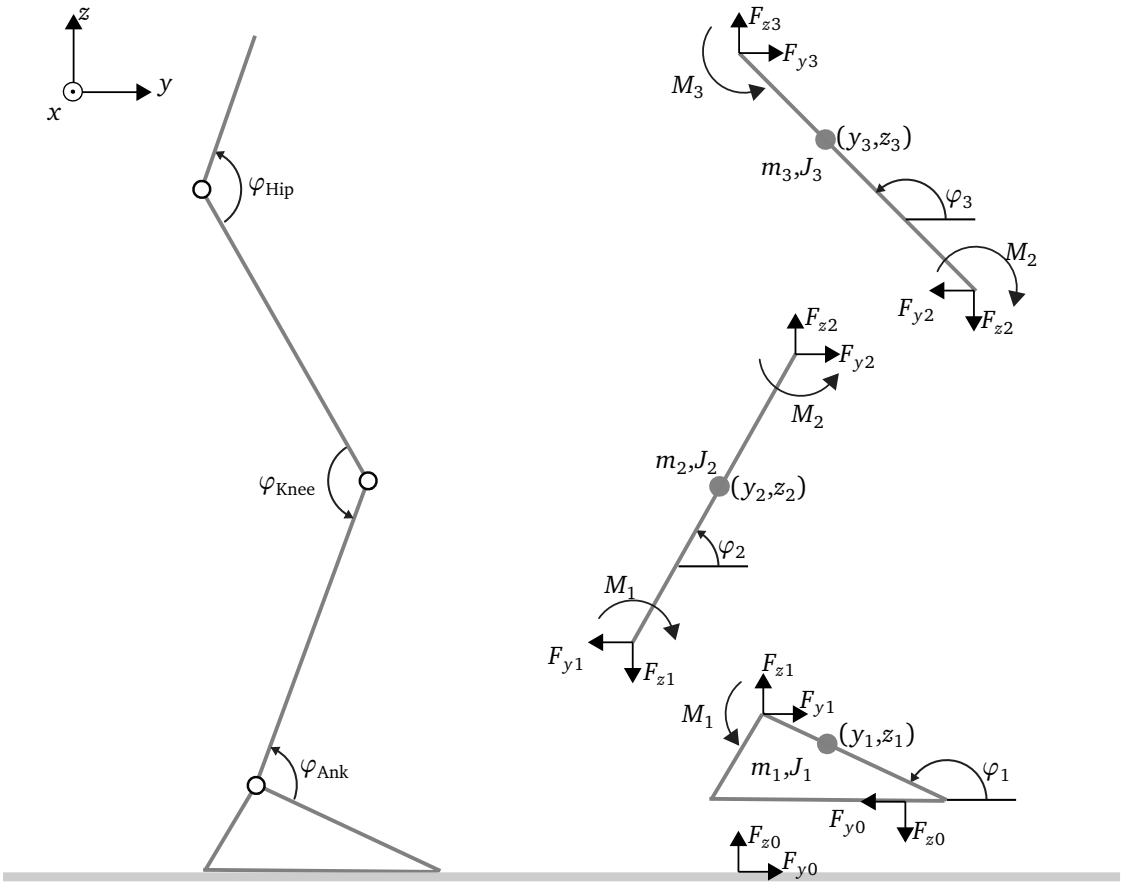

Figure B.4.: Free body diagram of the lower three segments foot, shank and thigh.

B.3.1. Joint kinematics and kinetics

Given the segments angles φ_1, φ_2, and φ_3 as shown in Figure B.4, the inner joint angles are defined as

$$\begin{aligned}\varphi_{\text{Ank}} &= \varphi_2 - \varphi_1 + 180^\circ \\ \varphi_{\text{Knee}} &= \varphi_2 - \varphi_3 + 180^\circ \\ \varphi_{\text{Hip}} &= \varphi_3 - \varphi_2 + 180^\circ\end{aligned}$$

and the joint extension torques are defined as

$$\begin{aligned}M_{\text{Ank}} &= -M_1 \\ M_{\text{Knee}} &= M_2 \\ M_{\text{Hip}} &= -M_3\ .\end{aligned}$$

The joint power

$$P_{\text{Joint}} = \dot{\varphi}_{\text{Joint}} M_{\text{Joint}}$$

is > 0, if the muscles at the joint generate power and < 0 if the muscles absorb power.

B.4. Motion capture

Figure B.5 displays the marker locations and Table B.1 lists the corresponding labels.

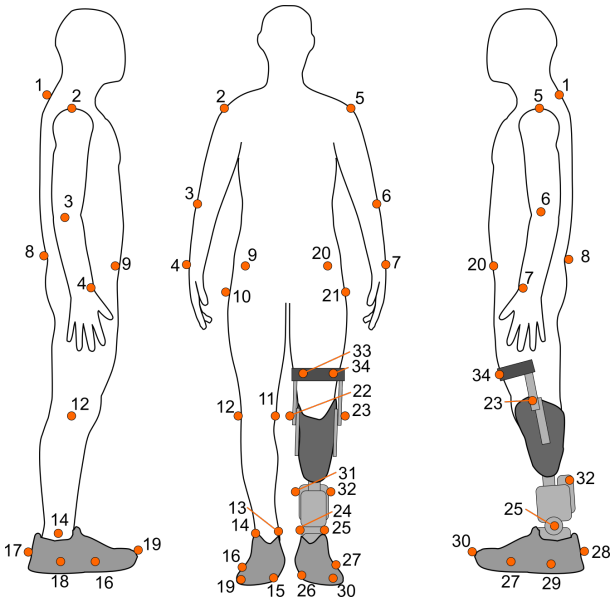

Figure B.5.: Markers used to in the prosthesis study. The marker labels are listed inTable B.1

Table B.1.: List of markers with numbers, labels and detailed location

Number (l/r)		Label (l/r)		Location
1		C7		Cervical Vertebrae 7
2	5	Sho_r/l	Sho_l	Acromion
3	6	Elb_r	Elb_l	Epicondylus lateralis humeri
4	7	Wri_r	Wri_l	Processus styloideus radii
8		Sac		Sacrum
9	20	Sia_r	Sia_l	Spina Iliaca anterior superior
10	21	Trc_r	Trc_l	Femur greater Trochanter
11	22	Kne_med_r	Kne_med_l	Condylus medialis femoris
12	23	Kne_lat_r	Kne_lat_l	Condylus lateralis femoris
13	24	Ank_med_r	Ank_med_l	Malleolus medialis or prosthesis joint medial
14	25	Ank_lat_r	Ank_lat_l	Malleolus lateralis or prosthesis joint lateral
15	26	Mt1_r	Mt1_l	Shoe matching Articulationes metatarsophalangeae I
16	27	Mt5_r	Mt5_l	Shoe matching Articulationes metatarsophalangeae V
17	28	Hee_r	Hee_l	Shoe heel
18	29	Mid_r	Mid_l	Shoe central lateral
19	30	Tip_r	Tip_l	Shoe tip
31		Pro_med		Prosthesis back medial
32		Pro_lat		Prosthesis back lateral
33		Ort_med		Orthetic thigh bracket medial
34		Ort_lat		Orthetic thigh bracket lateral

B.4.1. Joint centers

Table B.2.: Definition of lower limb joint centers

Joint center	Method
Foot distal tip	Lower end of the foot segment is defined as the center between Mt1 and Mt5 marker [114]
Ankle	The ankle joint center is defined as the midpoint between the lateral and medial ankle marker [114]
Knee	The Knee joint is defined as the midpoint between lateral and medial knee marker [114]
Hip	The hip joint center was calculatet using the GT-method [115], i.e. by shifting the ipsolateral TRC-marker by one quarter of the distance between the ipsolateral and the contralateral TRC-marker

B.5. Synchronization of multiple measurement systems

The measurements of the biomechanical experiments in this thesis are performed on different non-synchronized measurement systems. Two main of these measurement systems are the instrumented treadmill (ADAL-WR, HEF Tecmachine, Andrezieux Boutheon, France) and the Qualisys motion capture system. For longer walking experiments, the systems record data at the following measurement frequencies:

- Qualisys motion capture: 300 Hz
- ADAL instrumented treadmill: 100 Hz

The measurement frequency within each of the systems is specified by an internal quartz, which is subject to fluctuations. In this work, the measurement frequency of the motion capture system (300 Hz) is assumed to be exact and the measurement of the treadmill and all other systems is synchronized to it.

For synchronization, a rigid rod (aluminum profile bar, 20 mm×20 mm, $l = 0.5$ m) is dropped onto the force plate every minute for a measurement duration of 40 min. The rod tip is marked and recorded in the process with the motion capture sytem. By differentiation, the vertical acceleration of the rod can be determined, which is correlated with the force signal. The delay of the force measurement compared to the motion capture measurement results from the first impulse to 0.01 s. The time drift over the measurement duration of 2412 s (last impulse) is $\Delta t = -0.1066$ s. The corrected measurement frequency of the force measurement is 99.996 Hz. The result is reproducible on different measurement days (for this combination of measurement frequencies (300/100Hz)).

B.6. Energy expenditure

A metabolic system (K5, COSMED S.r.l., Rome, Italy) is used to measure the gas exchange with a mixing chamber technique. The system measures O2 and CO2 exhausted, from which the energy expenditure can be calculated.

Brockway [116] derived following formula

$$\text{Energy expenditure} = 16.58\frac{\text{kJ}}{\text{l}}\text{O}_2 + 4.51\frac{\text{kJ}}{\text{l}}\text{CO}_2 - 5.90\frac{\text{kJ}}{\text{g}}\text{N} \tag{B.3}$$

to estimate the energy expenditure of man, where O_2 and CO_2 are the oxygen uptake and the carbon dioxide production of the lungs, and N is the excreted nitrogen in the urine. For reference, typical values are 600 l oxygen per day, 525 l carbon dioxide per day, and 11 g nitrogen per day [116]. Following these numbers, nitrogen excretion only has a small influence on daily energy expenditure (about −0.5 %) and is therefore neglected.

Hence, the metabolic power in [W] is calculated according to

$$P_{\text{met}} = 16.58\frac{\text{J}}{\text{ml}}\dot{V}_{\text{O2}} + 4.51\frac{\text{J}}{\text{ml}}\dot{V}_{\text{CO2}}\,, \tag{B.4}$$

where $\dot{V}_{\text{O2}}$ and $\dot{V}_{\text{CO2}}$ are the oxygen uptake and carbon dioxide production, which are measured using the K5 at a 0.1 Hz.

B.6.1. Metabolics measurement dynamics

The authors in [110] found, that the relation between actual energetic cost and measured energetic cost based on respiratory measures can be modeled as a first-order differential equation with a time constant of 42 ± 12 s.

Figure B.6 shows the measured metabolic power as well as the first-order system fits for each of the three subjects. The individual time constants differ between the start of the experiment (increase in metabolic effort) and the end of the experiment (decrease in metabolic effort).

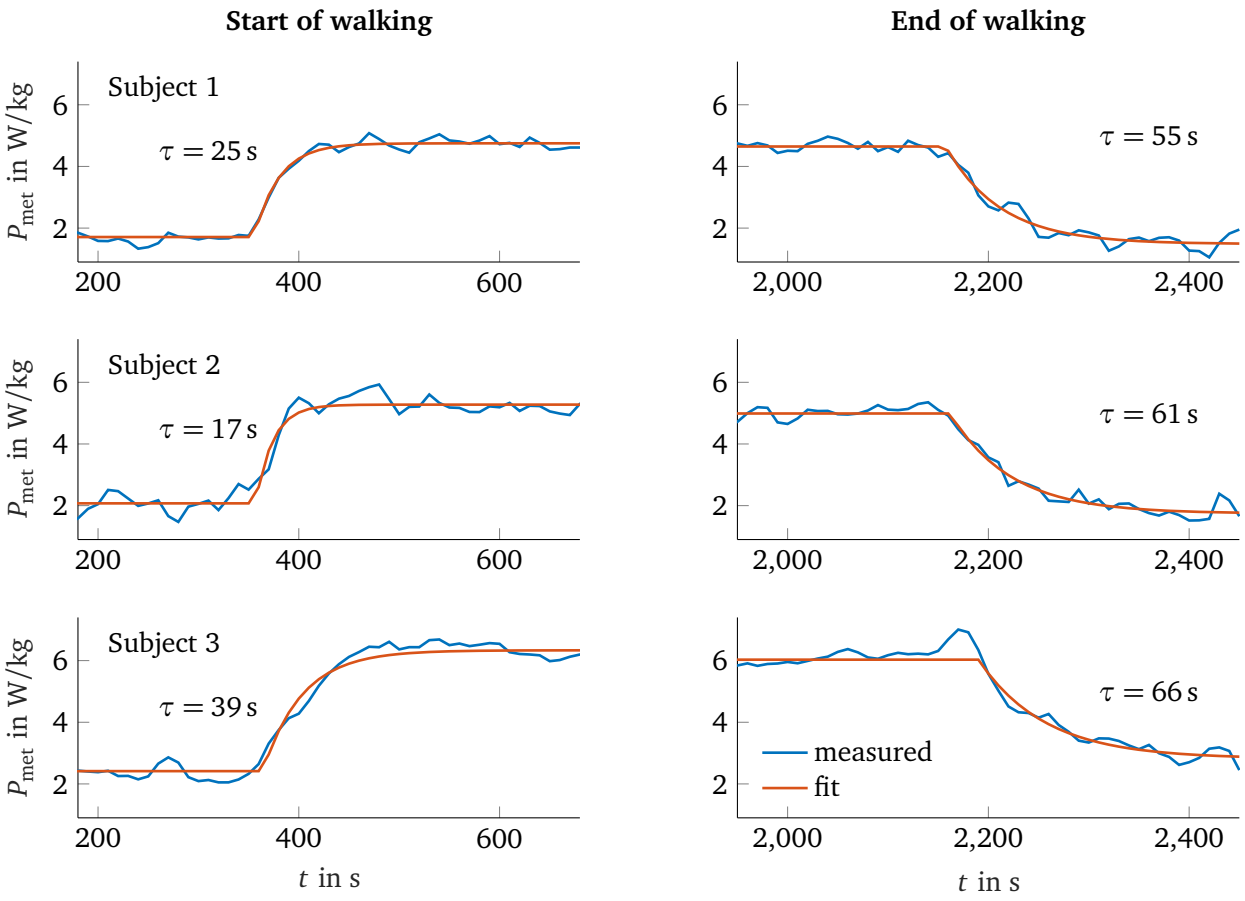

Figure B.6.: Measured metabolic power and least squares fit for start and end of the walking experiment for each of the three subjects

C. Individual joint biomechanics

The following section contains the individual measurement results of each subject from the walking experiments with the biarticular prosthesis.

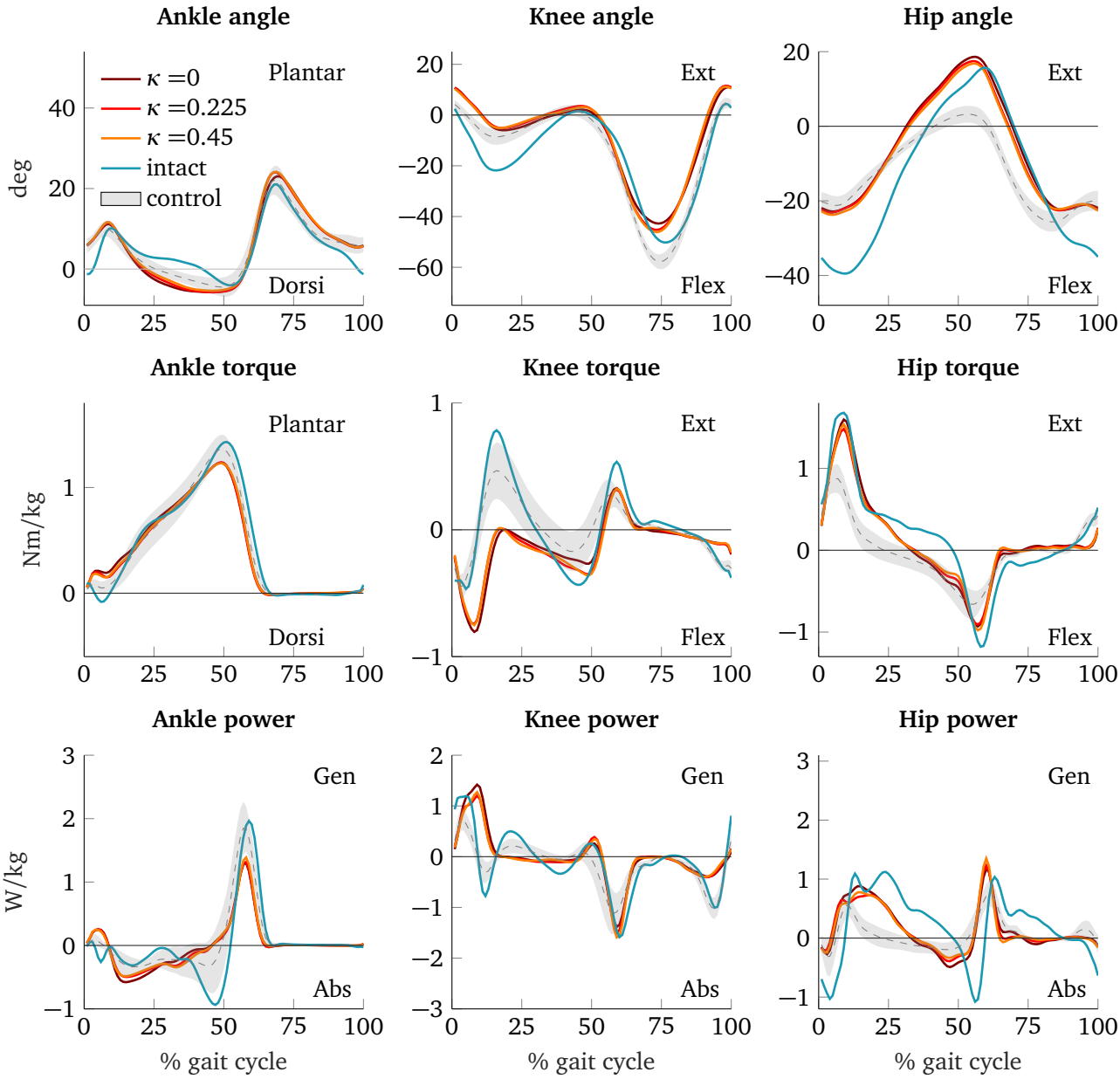

Figure C.1.: Hip, knee and ankle joint biomechanics of subject 1

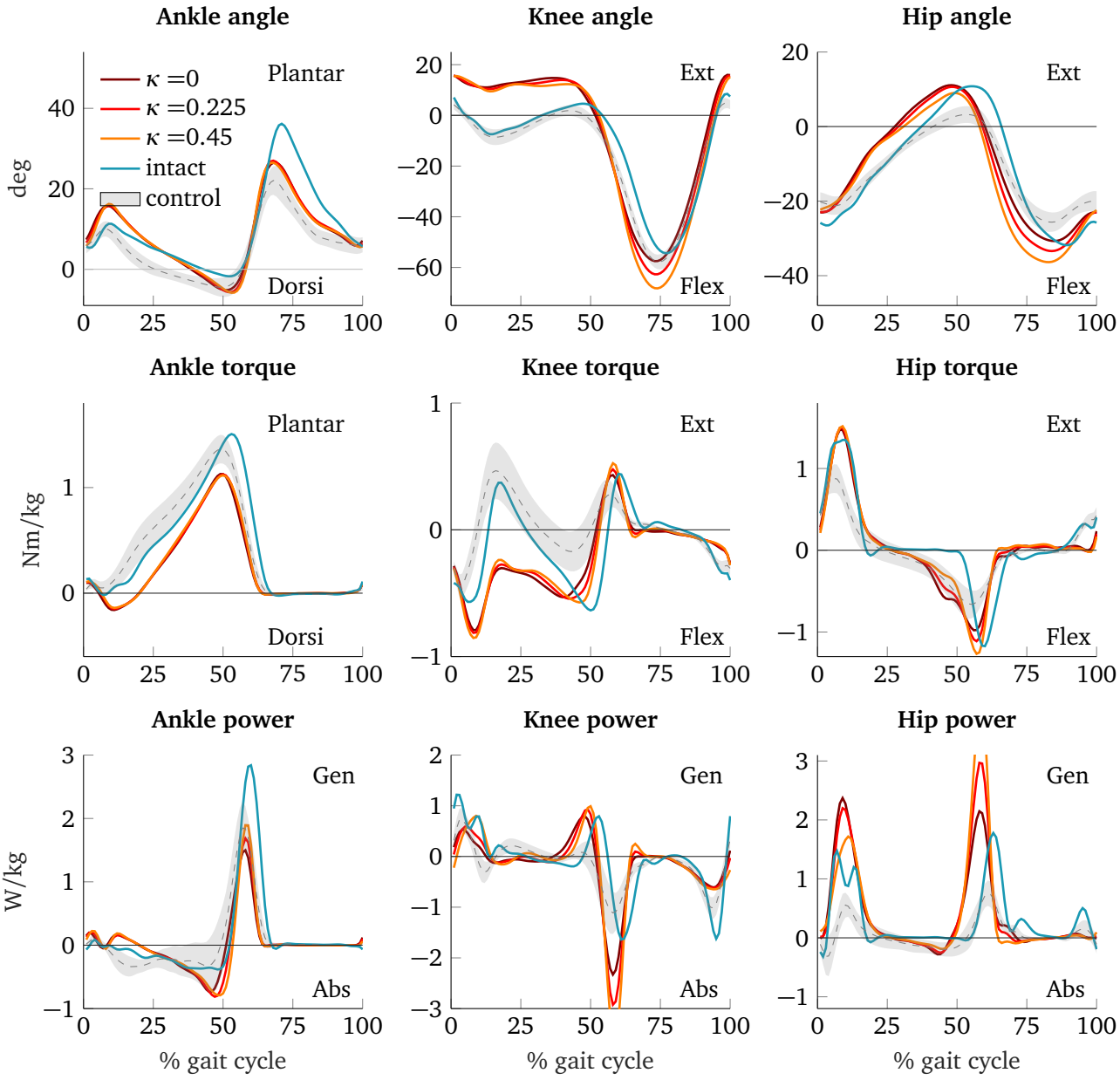

Figure C.2.: Hip, knee and ankle joint biomechanics of subject 2

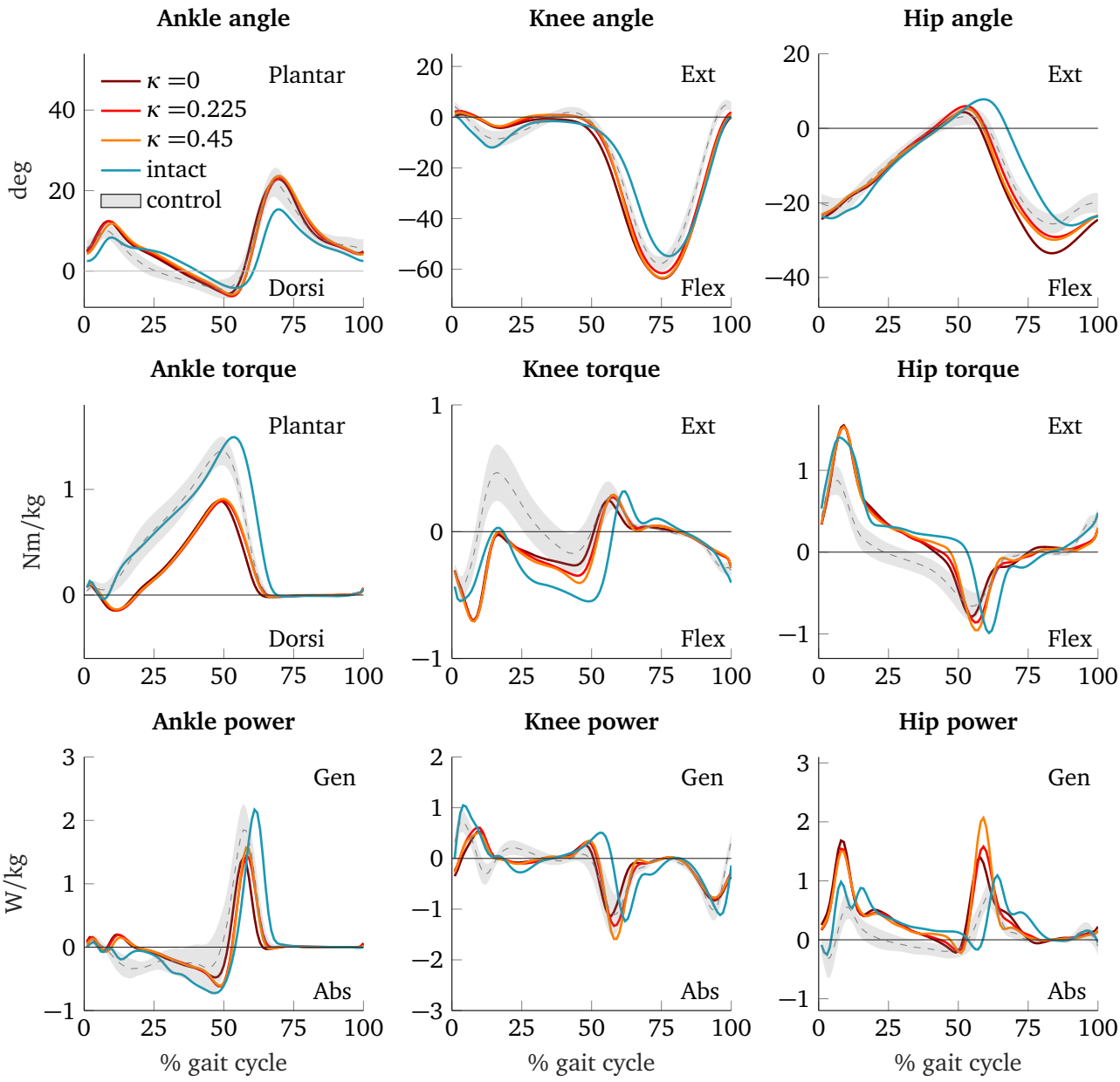

Figure C.3.: Hip, knee and ankle joint biomechanics of subject 3

Bibliography

[1] M. Spoden, "Amputationen der unteren Extremität in Deutschland – Regionale Analyse mit Krankenhausabrechnungsdaten von 2011 bis 2015," *Das Gesundheitswesen*, vol. 81, no. 05, pp. 422–430, 2019.

[2] G. Taeger and D. Nast-Kolb, "Amputationen und Prothesenversorgung der unteren Extremität," *Der Unfallchirurg*, vol. 103, no. 12, pp. 1097–1115, 2000.

[3] K. Kröger, C. Berg, F. Santosa, N. Malyar, and H. Reinecke, "Lower limb amputation in Germany: An analysis of data from the German Federal Statistical Office between 2005 and 2014," *Deutsches Ärzteblatt International*, vol. 114, no. 8, p. 130, 2017.

[4] M. Grimmer and A. Seyfarth, "Mimicking human-like leg function in prosthetic limbs," in *Neuro-Robotics*, Springer, 2014, pp. 105–155.

[5] R. L. Waters and S. Mulroy, "The energy expenditure of normal and pathologic gait," *Gait & Posture*, vol. 9, no. 3, pp. 207–231, 1999.

[6] R. Gailey, K. Allen, J. Castles, J. Kucharick, and M. Roeder, "Review of secondary physical conditions associated with lower-limb," *Journal of Rehabilitation Research & Development*, vol. 45, no. 1-4, pp. 15–30, 2008.

[7] C. B. Robbins, D. J. Vreeman, M. S. Sothmann, S. L. Wilson, and N. B. Oldridge, "A review of the long-term health outcomes associated with war-related amputation," *Military Medicine*, vol. 174, no. 6, pp. 588–592, 2009.

[8] M. F. Eilenberg, H. Geyer, and H. Herr, "Control of a powered ankle–foot prosthesis based on a neuromuscular model," *IEEE Transactions on Neural Systems and Rehabilitation Engineering*, vol. 18, no. 2, pp. 164–173, 2010.

[9] H. M. Herr and A. M. Grabowski, "Bionic ankle–foot prosthesis normalizes walking gait for persons with leg amputation," *Proceedings of the Royal Society B: Biological Sciences*, vol. 279, no. 1728, pp. 457–464, 2012.

[10] A. E. Ferris, J. M. Aldridge, C. A. Rábago, and J. M. Wilken, "Evaluation of a powered ankle-foot prosthetic system during walking," *Archives of Physical Medicine and Rehabilitation*, vol. 93, no. 11, pp. 1911–1918, 2012.

[11] M. Ackermann and A. J. Van den Bogert, "Optimality principles for model-based prediction of human gait," *Journal of Biomechanics*, vol. 43, no. 6, pp. 1055–1060, 2010.

[12] K. Junius, M. Moltedo, P. Cherelle, C. Rodriguez-Guerrero, B. Vanderborght, and D. Lefeber, "Biarticular elements as a contributor to energy efficiency: Biomechanical review and application in bio-inspired robotics," *Bioinspiration & Biomimetics*, vol. 12, no. 6, p. 061 001, 2017.

[13] K. Endo, E. Swart, and H. Herr, "An artificial gastrocnemius for a transtibial prosthesis," in *2009 Annual International Conference of the IEEE Engineering in Medicine and Biology Society*, IEEE, 2009, pp. 5034–5037.

[14] A. M. Willson, C. A. Richburg, A. J. Anderson, *et al.*, "Evaluation of a quasi-passive biarticular prosthesis to replicate gastrocnemius function in transtibial amputee gait," *Journal of Biomechanics*, vol. 129, p. 110 749, 2021.

[15] D. M. Ziemnicki, J. M. Caputo, K. A. McDonald, and K. E. Zelik, "Development and evaluation of a prosthetic ankle emulator with an artificial soleus and gastrocnemius," *Journal of Medical Devices*, vol. 15, no. 4, 2021.

[16] M. F. Eilenberg, "Development and evaluation of biarticular transtibial prostheses for level-ground amputee walking," Ph.D. dissertation, Massachusetts Institute of Technology, 2017.

[17] M. W. Whittle, *Gait analysis: an introduction*. Butterworth-Heinemann, 2014.

[18] M. L. Palmer, "Sagittal plane characterization of normal human ankle function across a range of walking gait speeds," Ph.D. dissertation, Massachusetts Institute of Technology, 2002.

[19] Y. Mrabet, wikimedia.org/wiki/File:Human_anatomy_Koerperebenen.svg, accessed 18-May-2022.

[20] D. A. Winter, *Biomechanics and motor control of human movement*. John Wiley & Sons, 2009.

[21] F. E. Zajac, R. R. Neptune, and S. A. Kautz, "Biomechanics and muscle coordination of human walking: Part i: Introduction to concepts, power transfer, dynamics and simulations," *Gait & Posture*, vol. 16, no. 3, pp. 215–232, 2002.

[22] C. Schumacher, M. Sharbafi, A. Seyfarth, and C. Rode, "Biarticular muscles in light of template models, experiments and robotics: A review," *Journal of the Royal Society Interface*, vol. 17, no. 163, p. 20 180 413, 2020.

[23] D. A. Winter and H. Yack, "EMG profiles during normal human walking: Stride-to-stride and inter-subject variability," *Electroencephalography and Clinical Neurophysiology*, vol. 67, no. 5, pp. 402–411, 1987.

[24] C. Spoor, J. Van Leeuwen, C. Meskers, A. Titulaer, and A. Huson, "Estimation of instantaneous moment arms of lower-leg muscles," *Journal of Biomechanics*, vol. 23, no. 12, pp. 1247–1259, 1990.

[25] S. G. McLean, A. Su, and A. J. van den Bogert, "Development and validation of a 3-d model to predict knee joint loading during dynamic movement," *Journal of Biomechanical Engineering*, vol. 125, no. 6, pp. 864–874, 2003.

[26] J. Van der Burg, L. Casius, *et al.*, "Factors underlying the perturbation resistance of the trunk in the first part of a lifting movement," *Biological cybernetics*, vol. 93, no. 1, pp. 54–62, 2005.

[27] I. A. Kramers-de Quervain, E. Stüssi, and A. Stacoff, "Ganganalyse beim Gehen und Laufen," *Schweizerische Zeitschrift für Sportmedizin und Sporttraumatologie*, vol. 56, no. 2, pp. 35–42, 2008.

[28] S. W. Lipfert, *Kinematic and dynamic similarities between walking and running*. Kovac Hamburg, 2010.

[29] H. Herr and A. M. Grabowski, "Bionic ankle–foot prosthesis normalizes walking gait for persons with leg amputation," *Proceedings of the Royal Society B: Biological Sciences*, vol. 279, no. 1728, pp. 457–464, 2011.

[30] M. Grimmer, M. Holgate, J. Ward, A. Boehler, and A. Seyfarth, "Feasibility study of transtibial amputee walking using a powered prosthetic foot," in *2017 International Conference on Rehabilitation Robotics (ICORR)*, IEEE, 2017, pp. 1118–1123.

[31] R. D. Bellman, M. A. Holgate, and T. G. Sugar, "Sparky 3: Design of an active robotic ankle prosthesis with two actuated degrees of freedom using regenerative kinetics," in *2008 2nd IEEE RAS & EMBS International Conference on Biomedical Robotics and Biomechatronics*, IEEE, 2008, pp. 511–516.

[32] P. Cherelle, V. Grosu, A. Matthys, B. Vanderborght, and D. Lefeber, "Design and validation of the ankle mimicking prosthetic (amp-) foot 2.0," *IEEE Transactions on Neural Systems and Rehabilitation Engineering*, vol. 22, no. 1, pp. 138–148, 2013.

[33] P. Cherelle, V. Grosu, M. Cestari, B. Vanderborght, and D. Lefeber, "The amp-foot 3, new generation propulsive prosthetic feet with explosive motion characteristics: Design and validation," *Biomedical Engineering Online*, vol. 15, no. 3, pp. 21–36, 2016.

[34] B. E. Lawson, J. Mitchell, D. Truex, A. Shultz, E. Ledoux, and M. Goldfarb, "A robotic leg prosthesis: Design, control, and implementation," *IEEE Robotics & Automation Magazine*, vol. 21, no. 4, pp. 70–81, 2014.

[35] M. Grimmer, M. Holgate, R. Holgate, *et al.*, "A powered prosthetic ankle joint for walking and running," *Biomedical Engineering Online*, vol. 15, no. 3, pp. 37–52, 2016.

[36] E. Pröbsting, B. Altenburg, M. Bellmann, K. Krug, and T. Schmalz, "How does ankle power on the prosthetic side influence loading parameters on the sound side during level walking of persons with transfemoral amputation?" *Prosthetics and Orthotics International*, pp. 10–1097, 2022.

[37] M. Grimmer and A. Seyfarth, "Stiffness adjustment of a series elastic actuator in an ankle-foot prosthesis for walking and running: The trade-off between energy and peak power optimization," in *2011 IEEE International Conference on Robotics and Automation*, IEEE, 2011, pp. 1439–1444.

[38] K. Hollander, R. Ilg, T. Sugar, and D. Herring, "An efficient robotic tendon for gait assistance.," *Journal of Biomechanical Engineering*, vol. 128, no. 5, pp. 788–791, 2006.

[39] A. S. Voloshina and S. H. Collins, "Lower limb active prosthetic systemsoverview," *Wearable Robotics*, pp. 469–486, 2020.

[40] Ottobock, https://www.ottobock.com/de-at/product/1C40, accessed 18.05.2022.

[41] Össur, https://www.ossur.com/de-de/prothetik/fusse/proprio-foot, accessed 18.05.2022.

[42] Ottobock, https://www.ottobockus.com/products/empower-ankle/, accessed 18.05.2022.

[43] K. A. Witte and S. H. Collins, "Design of lower-limb exoskeletons and emulator systems," in *Wearable Robotics*, Elsevier, 2020, pp. 251–274.

[44] M. F. Eilenberg, J.-Y. Kuan, and H. Herr, "Development and evaluation of a powered artificial gastrocnemius for transtibial amputee gait," *Journal of Robotics*, 2018.

[45] R. Müller, "Leichtbauantriebe mit hohen Kräften für Orthesengelenke," Ph.D. dissertation, Technische Universität, 2017.

[46] G. M. Bryan, P. W. Franks, S. C. Klein, R. J. Peuchen, and S. H. Collins, "A hip–knee–ankle exoskeleton emulator for studying gait assistance," *The International Journal of Robotics Research*, vol. 40, no. 4-5, pp. 722–746, 2021.

[47] K. A. Witte, J. Zhang, R. W. Jackson, and S. H. Collins, "Design of two lightweight, high-bandwidth torque-controlled ankle exoskeletons," in *2015 IEEE International Conference on Robotics and Automation*, IEEE, 2015, pp. 1223–1228.

[48] J. Zhang, P. Fiers, K. A. Witte, *et al.*, "Human-in-the-loop optimization of exoskeleton assistance during walking," *Science*, vol. 356, no. 6344, pp. 1280–1284, 2017.

[49] J. M. Caputo and S. H. Collins, "A universal ankle–foot prosthesis emulator for human locomotion experiments," *Journal of Biomechanical Engineering*, vol. 136, no. 3, 2014.

[50] A. M. Willson, C. A. Richburg, J. Czerniecki, K. M. Steele, and P. M. Aubin, "Design and development of a quasi-passive transtibial biarticular prosthesis to replicate gastrocnemius function in walking," *Journal of Medical Devices*, vol. 14, no. 2, 2020.

[51] H. Zhu, J. Doan, C. Stence, G. Lv, T. Elery, and R. Gregg, "Design and validation of a torque dense, highly backdrivable powered knee-ankle orthosis," in *2017 IEEE International Conference on Robotics and Automation*, IEEE, 2017, pp. 504–510.

[52] Ottobock, https://www.ottobock.com/de-de/product/50K13, accessed 29.09.2022.

[53] BeckerOrthopedics, https://www.beckerorthopedic.com/Product/KneeJoints/1000KneeSeries, accessed 29.09.2022.

[54] B. Quinlivan, S. Lee, P. Malcolm, *et al.*, "Assistance magnitude versus metabolic cost reductions for a tethered multiarticular soft exosuit," *Science Robotics*, vol. 2, no. 2, p. 4416, 2017.

[55] G. Lee, Y. Ding, I. G. Bujanda, N. Karavas, Y. M. Zhou, and C. J. Walsh, "Improved assistive profile tracking of soft exosuits for walking and jogging with off-board actuation," in *2017 IEEE/RSJ International Conference on Intelligent Robots and Systems*, IEEE, 2017, pp. 1699–1706.

[56] Y. Ding, I. Galiana, A. Asbeck, B. Quinlivan, S. M. M. De Rossi, and C. Walsh, "Multi-joint actuation platform for lower extremity soft exosuits," in *2014 IEEE International Conference on Robotics and Automation*, IEEE, 2014, pp. 1327–1334.

[57] CarlStahl-Technocables, https://www.carlstahl-technocables.de/seilkunde.html, accessed 17-Feb-2020.

[58] P. W. Franks, G. M. Bryan, R. M. Martin, R. Reyes, and S. H. Collins, "Comparing optimized exoskeleton assistance of the hip, knee, and ankle in single and multi-joint configurations," *bioRxiv*, 2021.

[59] A. H. Stienen, E. E. Hekman, F. C. Van Der Helm, and H. Van Der Kooij, "Self-aligning exoskeleton axes through decoupling of joint rotations and translations," *IEEE Transactions on Robotics*, vol. 25, no. 3, pp. 628–633, 2009.

[60] M. R. Tucker, J. Olivier, A. Pagel, *et al.*, "Control strategies for active lower extremity prosthetics and orthotics: A review," *Journal of Neuroengineering and Rehabilitation*, vol. 12, no. 1, pp. 1–30, 2015.

[61] R. Fluit, E. C. Prinsen, S. Wang, and H. Van Der Kooij, "A comparison of control strategies in commercial and research knee prostheses," *IEEE Transactions on Biomedical Engineering*, vol. 67, no. 1, pp. 277–290, 2019.

[62] R. Baud, A. R. Manzoori, A. Ijspeert, and M. Bouri, "Review of control strategies for lower-limb exoskeletons to assist gait," *Journal of Neuroengineering and Rehabilitation*, vol. 18, no. 1, pp. 1–34, 2021.

[63] M. A. Grün, *Regelungstechnische Aspekte bei aktiven Knieorthesen zur Mobilitätsunterstützung älterer Menschen*. epubli, 2015.

[64] F. Sup, A. Bohara, and M. Goldfarb, "Design and control of a powered transfemoral prosthesis," *The International Journal of Robotics Research*, vol. 27, no. 2, pp. 263–273, 2008.

[65] D. Quintero, D. J. Villarreal, D. J. Lambert, S. Kapp, and R. D. Gregg, "Continuous-phase control of a powered knee–ankle prosthesis: Amputee experiments across speeds and inclines," *IEEE Transactions on Robotics*, vol. 34, no. 3, pp. 686–701, 2018.

[66] M. Tschiedel, M. F. Russold, and E. Kaniusas, "Relying on more sense for enhancing lower limb prostheses control: A review," *Journal of Neuroengineering and Rehabilitation*, vol. 17, no. 1, pp. 1–13, 2020.

[67] F. Weigand, J. Zeiss, M. Grimmer, and U. Konigorski, “A novel approach for gait phase estimation for different locomotion modes using kinematic shank information,” *IFAC-PapersOnLine*, vol. 53, no. 2, pp. 8697–8703, 2020.

[68] S. O. Schrade, Y. Bader, M. R. Tucker, C. Shirota, and R. Gassert, “An adaptive and robust online method to predict gait events,” in *2016 38th Annual International Conference of the IEEE Engineering in Medicine and Biology Society (EMBC)*, IEEE, 2016, pp. 6277–6281.

[69] S. Pfeifer, A. Pagel, R. Riener, and H. Vallery, “Actuator with angle-dependent elasticity for biomimetic transfemoral prostheses,” *IEEE/ASME Transactions on Mechatronics*, vol. 20, no. 3, pp. 1384–1394, 2014.

[70] A. H. Shultz, B. E. Lawson, and M. Goldfarb, “Variable cadence walking and ground adaptive standing with a powered ankle prosthesis,” *IEEE Transactions on Neural Systems and Rehabilitation Engineering*, vol. 24, no. 4, pp. 495–505, 2015.

[71] F. Sup, H. A. Varol, J. Mitchell, T. J. Withrow, and M. Goldfarb, “Preliminary evaluations of a self-contained anthropomorphic transfemoral prosthesis,” *IEEE/ASME Transactions on Mechatronics*, vol. 14, no. 6, pp. 667–676, 2009.

[72] H. A. Varol and M. Goldfarb, “Decomposition-based control for a powered knee and ankle transfemoral prosthesis,” in *2007 IEEE 10th International Conference on Rehabilitation Robotics*, IEEE, 2007, pp. 783–789.

[73] R. Jimenez-Fabian and O. Verlinden, “Review of control algorithms for robotic ankle systems in lower-limb orthoses, prostheses, and exoskeletons,” *Medical Engineering & Physics*, vol. 34, no. 4, pp. 397–408, 2012.

[74] M. A. Holgate, T. G. Sugar, and A. W. Bohler, “A novel control algorithm for wearable robotics using phase plane invariants,” in *Robotics and Automation, 2009. ICRA'09. IEEE International Conference on*, IEEE, 2009, pp. 3845–3850.

[75] D. J. Villarreal, H. A. Poonawala, and R. D. Gregg, “A robust parameterization of human gait patterns across phase-shifting perturbations,” *IEEE Transactions on Neural Systems and Rehabilitation Engineering*, vol. 25, no. 3, pp. 265–278, 2016.

[76] N. Thatte, T. Shah, and H. Geyer, “Robust and adaptive lower limb prosthesis stance control via extended kalman filter-based gait phase estimation,” *IEEE Robotics and Automation Letters*, vol. 4, no. 4, pp. 3129–3136, 2019.

[77] M. Grün, R. Müller, and U. Konigorski, “Model based control of series elastic actuators,” in *4th IEEE RAS/EMBS International Conference on Biomedical Robotics and Biomechatronics (Biorob)*, IEEE, 2012, pp. 538–543.

[78] K. Kong, J. Bae, and M. Tomizuka, “Control of rotary series elastic actuator for ideal force-mode actuation in human–robot interaction applications,” *IEEE/ASME Transactions on Mechatronics*, vol. 14, no. 1, pp. 105–118, 2009.

[79] S. Oh and K. Kong, “High-precision robust force control of a series elastic actuator,” *IEEE/ASME Transactions on mechatronics*, vol. 22, no. 1, pp. 71–80, 2016.

[80] H. Vallery, R. Ekkelenkamp, H. Van Der Kooij, and M. Buss, “Passive and accurate torque control of series elastic actuators,” in *2007 IEEE/RSJ International Conference on Intelligent Robots and Systems*, IEEE, 2007, pp. 3534–3538.

[81] G. A. Pratt and M. M. Williamson, “Series elastic actuators,” in *Proceedings 1995 IEEE/RSJ International Conference on Intelligent Robots and Systems. Human Robot Interaction and Cooperative Robots*, IEEE, vol. 1, 1995, pp. 399–406.

[82] F. A. Panizzolo, I. Galiana, A. T. Asbeck, *et al.*, “A biologically-inspired multi-joint soft exosuit that can reduce the energy cost of loaded walking,” *Journal of Neuroengineering and Rehabilitation*, vol. 13, no. 1, pp. 1–14, 2016.

[83] J. Ward, K. Schroeder, D. Vehon, R. Holgate, A. Boehler, and M. Grimmer, “A rugged microprocessor controlled ankle-foot prosthesis for running,” in *39th Annual Meeting of the American Society of Biomechanics (ASB). Columbus*, 2015.

[84] R. C. Browning, J. R. Modica, R. Kram, and A. Goswami, “The effects of adding mass to the legs on the energetics and biomechanics of walking,” *Medicine & Science in Sports & Exercise*, vol. 39, no. 3, pp. 515–525, 2007.

[85] M. Nietert, “Untersuchungen zur Kinematik des menschlichen Kniegelenkes im Hinblick auf ihre Approximation in der Prothetik,” Ph.D. dissertation, 1975.

[86] M. Holler, “Force control of series elastic bowden cable actuators for orthotic and prosthetic applications,” M.S. thesis, TU Darmstadt, 2021.

[87] J. Braun, “Formulae handbook,” *ed: Maxon Motors*, 2012.

[88] maxon-motor, *Maxon DC motor and maxon EC motor - key information*, https://www.maxongroup.com/medias/sys_master/root/8815460712478/DC-EC-Key-Information-14-EN-42-50.pdf, accessed 18-May-2022.

[89] C. Xiang, X. Wang, Y. Ma, and B. Xu, “Practical modeling and comprehensive system identification of a BLDC motor,” *Mathematical Problems in Engineering*, vol. 2015, 2015.

[90] SpringActive, *ROA internal documentation*.

[91] F. Fritz, *Modellierung von Wälzlagern als generische Maschinenelemente einer Mehrkörpersimulation*. KIT Scientific Publishing, 2011, vol. 14.

[92] H. Baly, “Reibung Fettgeschmierter Wälzlager,” Ph.D. dissertation, Universität Hannover, 2005.

[93] J. Zeiss, F. Weigand, M. Grimmer, and U. Konigorski, “Control of a transtibial prosthesis with monoarticular and biarticular actuators,” *IFAC-PapersOnLine*, vol. 53, no. 2, pp. 8689–8696, 2020.

[94] A. T. Asbeck, S. M. De Rossi, K. G. Holt, and C. J. Walsh, “A biologically inspired soft exosuit for walking assistance,” *The International Journal of Robotics Research*, vol. 34, no. 6, pp. 744–762, 2015.

[95] G. Roppenecker, “Zustandsregelung linearer Systeme - Eine Neubetrachtung (state feedback control of linear systems - a renewed approach),” *at - Automatisierungstechnik*, vol. 57, no. 10, pp. 491–498, 2009.

[96] O. Föllinger, F. Dörrscheidt, and M. Klittich, “Regelungstechnik – Einführung in die Methoden und ihre Anwendung,” *Hüthig Buch Verlag Heidelberg, 8. überarb. Aufl.*, 1994.

[97] G. Grabmair and R. Gahleitner, “PI-Zustandsregler - eine methodische Neubetrachtung,” *at - Automatisierungstechnik*, vol. 67, no. 9, pp. 727–738, 2019.

[98] J. Lunze, *Regelungstechnik 2*. Springer, 2014.

[99] J. Adamy, *Nichtlineare Systeme und Regelungen*. Springer, 2018.

[100] Y. Peng, D. Vrancic, and R. Hanus, “Anti-windup, bumpless, and conditioned transfer techniques for pid controllers,” *IEEE Control Systems Magazine*, vol. 16, no. 4, pp. 48–57, 1996.

[101] J. Adamy, *Fuzzy Logik, Neuronale Netze und Evolutionäre Algorithmen*, 4. überarbeitete Auflage. Shaker Verlag, 2015.

[102] B. Dauriac, X. Bonnet, H. Pillet, and F. Lavaste, "Estimation of the walking speed of individuals with transfemoral amputation from a single prosthetic shank-mounted IMU," *Proceedings of the Institution of Mechanical Engineers, Part H: Journal of Engineering in Medicine*, vol. 233, no. 9, pp. 931–937, 2019.

[103] D. Quintero, D. J. Lambert, D. J. Villarreal, and R. D. Gregg, "Real-time continuous gait phase and speed estimation from a single sensor," in *2017 IEEE Conference on Control Technology and Applications*, IEEE, 2017, pp. 847–852.

[104] F. Weigand, A. Höhl, J. Zeiss, U. Konigorski, and M. Grimmer, "Continuous locomotion mode recognition and gait phase estimation based on a shank-mounted imu with artificial neural networks," in *2022 IEEE/RSJ International Conference on Intelligent Robots and Systems*, IEEE, 2022, pp. 12 744–12 751.

[105] M. Grimmer, K. Schmidt, J. E. Duarte, L. Neuner, G. Koginov, and R. Riener, "Stance and swing detection based on the angular velocity of lower limb segments during walking," *Frontiers in Neurorobotics*, vol. 13, p. 57, 2019.

[106] F. A. Panizzolo, S. Lee, T. Miyatake, *et al.*, "Lower limb biomechanical analysis during an unanticipated step on a bump reveals specific adaptations of walking on uneven terrains," *Journal of Experimental Biology*, vol. 220, no. 22, pp. 4169–4176, 2017.

[107] H. Lee and N. Hogan, "Time-varying ankle mechanical impedance during human locomotion," *IEEE Transactions on Neural Systems and Rehabilitation Engineering*, vol. 23, no. 5, pp. 755–764, 2015.

[108] H. Lee, E. J. Rouse, and H. I. Krebs, "Summary of human ankle mechanical impedance during walking," *IEEE Journal of Translational Engineering in Health and Medicine*, vol. 4, pp. 1–7, 2016.

[109] E. J. Rouse, L. J. Hargrove, E. J. Perreault, and T. A. Kuiken, "Estimation of human ankle impedance during the stance phase of walking," *IEEE Transactions on Neural Systems and Rehabilitation Engineering*, vol. 22, no. 4, pp. 870–878, 2014.

[110] J. C. Selinger and J. M. Donelan, "Estimating instantaneous energetic cost during non-steady-state gait," *Journal of Applied Physiology*, vol. 117, no. 11, pp. 1406–1415, 2014.

[111] P. Malcolm, D. M. Rossi, C. Siviy, *et al.*, "Continuous sweep versus discrete step protocols for studying effects of wearable robot assistance magnitude," *Journal of Neuroengineering and Rehabilitation*, vol. 14, no. 1, pp. 1–13, 2017.

[112] D. Villeger, A. Costes, B. Watier, and P. Moretto, "An algorithm to decompose ground reaction forces and moments from a single force platform in walking gait," *Medical Engineering & Physics*, vol. 36, no. 11, pp. 1530–1535, 2014.

[113] E. Kristianslund, T. Krosshaug, and A. J. Van den Bogert, "Effect of low pass filtering on joint moments from inverse dynamics: Implications for injury prevention," *Journal of Biomechanics*, vol. 45, no. 4, pp. 666–671, 2012.

[114] R. Dumas, L. Cheze, and J.-P. Verriest, "Adjustments to McConville et al. and Young et al. body segment inertial parameters," *Journal of Biomechanics*, vol. 40, no. 3, pp. 543–553, 2007.

[115] J. T. Weinhandl and K. M. OConnor, "Assessment of a greater trochanter-based method of locating the hip joint center," *Journal of Biomechanics*, vol. 43, no. 13, pp. 2633–2636, 2010.

[116] J. Brockway, "Derivation of formulae used to calculate energy expenditure in man.," *Human Nutrition. Clinical Nutrition*, vol. 41, no. 6, pp. 463–471, 1987.

[117] R. L. Medrano, G. C. Thomas, and E. J. Rouse, “Can humans perceive the metabolic benefit provided by augmentative exoskeletons?” *Journal of Neuroengineering and Rehabilitation*, vol. 19, no. 1, pp. 1–13, 2022.

[118] T. M. Griffin, T. J. Roberts, and R. Kram, “Metabolic cost of generating muscular force in human walking: Insights from load-carrying and speed experiments,” *Journal of Applied Physiology*, vol. 95, no. 1, pp. 172–183, 2003.

[119] G. S. Sawicki, C. L. Lewis, and D. P. Ferris, “It pays to have a spring in your step,” *Exercise and Sport Sciences Reviews*, vol. 37, no. 3, p. 130, 2009.

[120] F. E. Zajac, “Understanding muscle coordination of the human leg with dynamical simulations,” *Journal of Biomechanics*, vol. 35, no. 8, pp. 1011–1018, 2002.

[121] K. A. Ingraham, C. D. Remy, and E. J. Rouse, “The role of user preference in the customized control of robotic exoskeletons,” *Science Robotics*, vol. 7, no. 64, eabj3487, 2022.

[122] M. Grimmer, J. Zeiss, F. Weigand, and G. Zhao, “Exploring surface electromyography (EMG) as a feedback variable for the human-in-the-loop optimization of lower limb wearable robotics,” *Frontiers in Neurorobotics*, vol. 16, p. 948 093, 2022.

[123] J. Wojtusch and O. von Stryk, “Humod-a versatile and open database for the investigation, modeling and simulation of human motion dynamics on actuation level,” in *Humanoid Robots (Humanoids), 2015 IEEE-RAS 15th International Conference on*, IEEE, 2015, pp. 74–79.

[124] S. H. Collins, P. G. Adamczyk, D. P. Ferris, and A. D. Kuo, “A simple method for calibrating force plates and force treadmills using an instrumented pole,” *Gait & Posture*, vol. 29, no. 1, pp. 59–64, 2009.

[125] G. J. Verkerke, A. Hof, W. Zijlstra, W. Ament, and G. Rakhorst, “Determining the centre of pressure during walking and running using an instrumented treadmill,” *Journal of Biomechanics*, vol. 38, no. 9, pp. 1881–1885, 2005.

[126] F. Weigand, J. Zeiss, U. Konigorski, and M. Grimmer, “Cross-validation results for a gait phase estimation with artificial neural networks,” *Proceedings on Automation in Medical Engineering*, vol. 1, no. 1, pp. 026–026, 2020.

[127] F. Weigand, J. Zeiss, M. Grimmer, and U. Konigorski, “Combined estimation of gait phase and stair slope utilizing time history data,” in *Proceedings on Automation in Medical Engineering*, 2021.

[128] M. Grimmer, J. Zeiss, F. Weigand, *et al.*, “Lower limb joint biomechanics-based identification of gait transitions in between level walking and stair ambulation,” *Plos One*, vol. 15, no. 9, e0239148, 2020.

[129] R. Aftung, A. Busch, S. Weimer, and M. Knaust, “Entwurf einer Aktoreinheit für eine biartikuläre Prothese,” TU Darmstadt, Projektseminar, 2018.

[130] J. Butz and M. Holler, “Aufbau eines Bowdenzugaktor-Prüfstandes,” TU Darmstadt, Projektseminar, 2020.

[131] A. Trifan, “Segmentwinkelbasierte Gangphasenschätzung für ebenes Gehen,” BA thesis, TU Darmstadt, 2018.

[132] C. Hölzer, “Muskelkraftbestimmung mittels Inverser Dynamik und Optimaler Steuerung dynamischer Muslkelmodelle,” BA thesis, TU Darmstadt, 2018.

[133] M. Amann, “Robuste Polbereichsplatzierung für den Kraftaktor einer biartikulären Prothese,” BA thesis, TU Darmstadt, 2019.

[134] L. Nevermann, “Das Kalmanfilter zur Lageschätzung des Unterschenkels beim ebenen Gehen,” BA thesis, TU Darmstadt, 2019.

[135] E. Bräuer, “Sollgrössengenerierung für aktive Prothesenfüsse mittels Muskelreflexmodellen,” BA thesis, TU Darmstadt, 2020.

[136] L. M. Tapia Hernandes, “Regelung seriellelastischer Antriebe zur Darstellung virtueller Impedanzen,” BA thesis, TU Darmstadt, 2020.

[137] S. Tanner, “Virtual impedance based reference generation for powered prosthetic feet,” BA thesis, TU Darmstadt, 2021.

[138] F. Weigand, “Bestimmung menschlicher Muskelkräfte bei ebenem Gehen mittels Optimalsteuerung,” M.S. thesis, TU Darmstadt, 2018.

[139] J. Butz, “Optimierung seriell-elastischer Antriebe in überaktuierten Beinprothesen,” M.S. thesis, TU Darmstadt, 2021.

Own publications

[67] F. Weigand, J. Zeiss, M. Grimmer, and U. Konigorski, “A novel approach for gait phase estimation for different locomotion modes using kinematic shank information,” *IFAC-PapersOnLine*, vol. 53, no. 2, pp. 8697–8703, 2020.

[93] J. Zeiss, F. Weigand, M. Grimmer, and U. Konigorski, “Control of a transtibial prosthesis with monoarticular and biarticular actuators,” *IFAC-PapersOnLine*, vol. 53, no. 2, pp. 8689–8696, 2020.

[104] F. Weigand, A. Höhl, J. Zeiss, U. Konigorski, and M. Grimmer, “Continuous locomotion mode recognition and gait phase estimation based on a shank-mounted imu with artificial neural networks,” in *2022 IEEE/RSJ International Conference on Intelligent Robots and Systems*, IEEE, 2022, pp. 12 744–12 751.

[122] M. Grimmer, J. Zeiss, F. Weigand, and G. Zhao, “Exploring surface electromyography (EMG) as a feedback variable for the human-in-the-loop optimization of lower limb wearable robotics,” *Frontiers in Neurorobotics*, vol. 16, p. 948 093, 2022.

[126] F. Weigand, J. Zeiss, U. Konigorski, and M. Grimmer, “Cross-validation results for a gait phase estimation with artificial neural networks,” *Proceedings on Automation in Medical Engineering*, vol. 1, no. 1, pp. 026–026, 2020.

[127] F. Weigand, J. Zeiss, M. Grimmer, and U. Konigorski, “Combined estimation of gait phase and stair slope utilizing time history data,” in *Proceedings on Automation in Medical Engineering*, 2021.

[128] M. Grimmer, J. Zeiss, F. Weigand, *et al.*, “Lower limb joint biomechanics-based identification of gait transitions in between level walking and stair ambulation,” *Plos One*, vol. 15, no. 9, e0239148, 2020.

Student works related to thesis

[86] M. Holler, “Force control of series elastic bowden cable actuators for orthotic and prosthetic applications,” M.S. thesis, TU Darmstadt, 2021.

[129] R. Aftung, A. Busch, S. Weimer, and M. Knaust, “Entwurf einer Aktoreinheit für eine biartikuläre Prothese,” TU Darmstadt, Projektseminar, 2018.

[130] J. Butz and M. Holler, “Aufbau eines Bowdenzugaktor-Prüfstandes,” TU Darmstadt, Projektseminar, 2020.

[131] A. Trifan, “Segmentwinkelbasierte Gangphasenschätzung für ebenes Gehen,” BA thesis, TU Darmstadt, 2018.

[132] C. Hölzer, “Muskelkraftbestimmung mittels Inverser Dynamik und Optimaler Steuerung dynamischer Muslkelmodelle,” BA thesis, TU Darmstadt, 2018.

[133] M. Amann, “Robuste Polbereichsplatzierung für den Kraftaktor einer biartikulären Prothese,” BA thesis, TU Darmstadt, 2019.

[134] L. Nevermann, “Das Kalmanfilter zur Lageschätzung des Unterschenkels beim ebenen Gehen,” BA thesis, TU Darmstadt, 2019.

[135] E. Bräuer, “Sollgrössengenerierung für aktive Prothesenfüsse mittels Muskelreflexmodellen,” BA thesis, TU Darmstadt, 2020.

[136] L. M. Tapia Hernandes, “Regelung seriellelastischer Antriebe zur Darstellung virtueller Impedanzen,” BA thesis, TU Darmstadt, 2020.

[137] S. Tanner, “Virtual impedance based reference generation for powered prosthetic feet,” BA thesis, TU Darmstadt, 2021.

[138] F. Weigand, “Bestimmung menschlicher Muskelkräfte bei ebenem Gehen mittels Optimalsteuerung,” M.S. thesis, TU Darmstadt, 2018.

[139] J. Butz, “Optimierung seriell-elastischer Antriebe in überaktuierten Beinprothesen,” M.S. thesis, TU Darmstadt, 2021.